

THESIS FOR THE DEGREE OF DOCTOR OF PHILOSOPHY

Microsystem technology for microwave applications at frequencies above 100 GHz

SOFIA RAHIMINEJAD



Department of Microtechnology and Nanoscience
CHALMERS UNIVERSITY OF TECHNOLOGY

Göteborg, Sweden 2016

Microsystem technology for microwave applications at frequencies above 100 GHz
SOFIA RAHIMINEJAD
ISBN 978-91-7597-513-9

© SOFIA RAHIMINEJAD, 2016

Doktorsavhandlingar vid Chalmers tekniska högskola
Ny serie Nr 4194
ISSN 0346-718X

Electronics Materials and Systems Laboratory
Department of Microtechnology and Nanoscience (MC2)
CHALMERS UNIVERSITY OF TECHNOLOGY
SE-412 96 Göteborg,
Sweden
Tel. +46-(0)31 772 1000

ISSN 1652-0769
Technical Report MC2-352

Cover: From top to bottom, left to right: The Si gap adapter, the 280 GHz ridge gap resonator, the H-bend rectangular waveguide-to-microstrip transition, the 100 GHz Ridge Gap Waveguide Antenna, the 100 GHz Groove Gap resonator, the 100 GHz Ridge Gap Waveguides, and the SU8 gap adapter.

Printed by Reproservice
Göteborg, Sweden 2016

"Nothing in this world that's worth having comes easy"

Bob Kelso

Abstract

The rapid development of wireless technology today shows an increasing need for electromagnetic components operating at even higher frequencies. Higher frequencies offer wider bandwidth, higher spatial resolution and are needed for technologies such as automotive car radars, wireless media communication and body scanners.

The biggest issues with developing high frequency components are the small dimensions needed. With the small dimensions, issues with connectivity and resolution of the structures have become difficult to handle at frequencies above 100 GHz. The most common fabrication method used is micro-milling in brass, however this is limited in its resolution and micro-milling is not a mass production method, thus making it expensive.

This thesis aims to realize electromagnetic components at high frequencies, more specific above 100 GHz, with the help of microsystem technology. The thesis covers a background and history of the field, a discussion of the technologies used and presents the fabricated devices all made with microsystem technology.

A 280 GHz ridge gap resonator was fabricated in Si, and measured. The calculated attenuation from the ridge gap resonator was $0.033 - 0.043 \text{ dB/mm}$, which is higher than a rectangular waveguide, but lower than a microstrip line for the same frequency range.

The 280 GHz resonator design was used to evaluate the polymer SU8 and carbon nanotubes as a base material for fast and low-cost prototyping of high-frequency electromagnetic components. The SU8 showed promising performance with an extracted attenuation of $0.041 - 0.063 \text{ dB/mm}$, and a less costly process. The carbon nanotube ridge gap resonator showed a higher attenuation of $0.051 - 0.079 \text{ dB/mm}$ and was determined to be the lossiest of these realisations.

An issue that was noticed when performing measurements above 100 GHz was how sensitive the connection between the measurement flanges and the device under test was. A gap of a few micrometers could create huge leakage, and measuring at these frequencies turned out to be difficult. A gap adapter was designed, with the purpose of reducing these leakages. The gap adapter evolved from a brass prototype to a gold covered SU8 device. The measurement study showed that the gap adapter had the same performance with and without screws, and gaps up to $50 \mu\text{m}$, thus reducing leakage.

Groove and ridge gap waveguide technology was further explored at 100 GHz. Both a ridge and groove gap waveguide were fabricated using SOI wafers. The groove gap 90° bend waveguide showed a return loss of 15 dB, and an insertion loss around 0.4 dB. The groove gap waveguide was designed to match the rectangular measurement flange, however the ridge gap waveguide needed a microstrip-to-ridge transition to be measured. This setup was sensitive to misalignment, so only measurements on the ridge gap resonator could be obtained. The calculated attenuation was $0.036 \text{ dB}/\lambda$.

Another transition that was fabricated and explored was an H-bend rectangular waveguide-to-microstrip transition operating at 140-220 GHz. A transition structure and a similar hollow waveguide consisting of four etch depths were fabricated in Si. Measurements were performed on the hollow waveguide, and the insertion loss was around 1.5 dB and the return loss was around 10 dB.

A ridge gap antenna prototype based on the previous fundamental structures, was fabricated in Si for 100 GHz. The ridge gap antenna has a 15.5% bandwidth and a gain of 10.3 dBi matching perfectly the simulated design.

The presented work in this thesis shows how microsystem technology can realize mass producible microwave components operating above 100 GHz.

Keywords: MEMS, RF, Waveguide, High frequency, GHz, Gap waveguides, Transitions

List of Publications

This thesis is based on the work contained in the following papers:

Paper I

S. Rahiminejad, A. U. Zaman, E. Pucci, H. Raza, V. Vassilev, S. Haasl, P. Lundgren, P.-S. Kildal, and P. Enoksson, "Micromachined ridge gap waveguide and resonator for millimeter-wave applications," *Sensors and Actuators A: Physical*, vol. 186, pp. 264–269, 2012.

Paper II

S. Rahiminejad, E. Pucci, S. Haasl, and P. Enoksson, "Micromachined Contactless Pin-Flange Adapter for Robust High-Frequency Measurements," *Journal of Micromachining and Microengineering*, vol. 24, no. 8, p. 084004, 2014.

Paper III

S. Rahiminejad, H. Raza, A. U. Zaman, S. Haasl, P. Enoksson, and P.-S. Kildal, "Micromachined Gap Waveguides for 100 GHz Applications," In *Proceedings of the 7th European Conference on Antennas and Propagation, EuCAP 2013*, Gothenburg, Sweden, 8-12 April 2013.

Paper IV

S. Rahiminejad, A. Algaba Brazález, H. Raza., E. Pucci, S. Haasl, P.-S. Kildal and P. Enoksson, "100 GHz SOI Gap Waveguides" *The 17th International Conference on Solid-State Sensors, Actuators and Microsystems*, Barcelona, Spain, 16-20 June, 2013.

Paper V

S. Rahiminejad, A. U. Zaman, E. Pucci, S. Haasl, and P. Enoksson, "SU8 Ridge Gap Resonator," *International Journal of Microwave and Wireless Technologies*. vol. 6, no. 05, pp. 459–465, 2014.

Paper VI

A. M. Saleem, S. Rahiminejad, V. Desmaris, and P. Enoksson, "Carbon nanotubes as base material for fabrication of gap waveguide components," *Sensors Actuators, A: Physical*, vol. 224, pp. 163–168, 2015.

Paper VII

S. Rahiminejad, E. Pucci, V. Vassilev, P.-S. Kildal, S. Haasl, and P. Enoksson, "Polymer Gap Adapter for Contactless, Robust, and Fast Measurements at 220–325 GHz," *Journal of Microelectromechanical Systems*, vol. 25, no. 1, pp. 160–169, 2016.

Paper VIII

S. Rahiminejad, P. Cegielski, M. Abbasi, and P. Enoksson, "A Four Level Silicon Microstructure Fabrication By DRIE," *Journal of Micromachining and Microengineering*, vol. 26, no. 8, p. 084003, 2016.

Paper IX

S. Rahiminejad, A. U. Zaman, S. Haasl, P.-S. Kildal, and P. Enoksson, "Demonstration of a micromachined planar distribution network in gap waveguide technology for a linear slot array antenna at 100 GHz," *Journal of Micromachining and Microengineering*, vol. 26, no. 7, p. 074001, 2016.

Other related publications by the Author not included in this thesis:

- S. Rahiminejad, A. U. Zaman, E. Pucci, H. Raza, V. Vassilev, S. Haasl, P. Lundgren, P.-S. Kildal and P. Enoksson, “Micromachined ridge gap waveguide for sub millimeter and millimeter wave applications”, *MME 2011, 22nd Micromechanics and Micro Systems Europe Workshop*, June 19-22, 2011, Toensberg, Norway.
- S. Rahiminejad, A. U. Zaman, E. Pucci, H. Raza, V. Vassilev, S. Haasl, P. Lundgren, P.-S. Kildal and P. Enoksson, “Design of Micromachined Ridge Gap Waveguides for Millimeter-Wave Applications”, *Proc. Euroensors XXV*, September 4-7, 2011, Athens, Greece
- S. Rahiminejad, A. U. Zaman, E. Pucci, H. Raza, V. Vassilev, S. Haasl, P. Lundgren, P.-S. Kildal and P. Enoksson, "Micromachined Ridge Gap Waveguide and Resonator for 220-325 GHz", *The 9th Micronano Systems Workshop*, May 9-10, 2012, Linköping, Sweden
- S. Rahiminejad, E. Pucci, S. Haasl, P.-S. Kildal and P. Enoksson, “Contactless Pin-Flange Adapter for High-Frequency Measurements”, *MME 2012, 23de Micromechanics and Micro Systems Europe Workshop*, Illmenau, Germany, September 9 - 12, 2012.
- A. Algaba Brazález, E. Pucci, S. Rahiminejad, M. Ferndahl, P.-S. Kildal, “Evaluation of losses of the ridge gap waveguide at 100 GHz”, *IEEE International Symposium on Antennas and Propagation, AP-S 2013*, Orlando, USA, July 7-12, 2013
- S. Rahiminejad, E. Pucci, A. U. Zaman, S. Haasl, P. Enoksson, “SU8 Ridge Gap Resonator”, *MEMSWAVE, 2013*, Potsdam, Germany, July 1-3, 2013.
- A. M. Saleem, S. Rahiminejad, V. Desmaris, P. Enoksson , “A Carbon nanotube ridge gap resonator”, *MEMSWAVE, 2013*, Potsdam, Germany, July 1-3, 2013.
- S. Rahiminejad, E. Pucci, S. Haasl, and P. Enoksson, “Micromachined Double-Sided SOI Pin-Flange Adapter for 100 GHz”, *MME 2013, 24th Micromechanics and Micro Systems Europe Workshop*, Espoo, Finland, September 1 - 4, 2013.
- S. Rahiminejad, E. Pucci, A. U. Zaman, V. Desmaris, S. Haasl, P. Enoksson, P.-S. Kildal, "Micromachined gap waveguide devices for above 100 GHz," *Swedish Microwave Days* March 11-12, 2014.

- S. Rahiminejad, E. Pucci, A. U. Zaman, V. Desmaris, S. Haasl, P. Enoksson, P.-S. Kildal, "Micromachined gap waveguide devices for above 100 GHz," *The 10th Micronano Systems Workshop*, May 15-16, 2014, Uppsala, Sweden.
- S. Rahiminejad, E. Pucci, S. Haasl, and P. Enoksson, "Micromachined double-sided SOI pin-flange adapter for 100 GHz," *MME 2014, 25th Micromechanics and Micro Systems Europe Workshop*, Istanbul, Turkey, August 31 - September 3, 2014.
- A. M. Saleem, S. Rahiminejad, V. Desmaris, P. Enoksson, "A Carbon nanotube ridge gap resonator", *MEMSWAVE, 2014*, La Rochelle, France, June 30 – July 2, 2014.
- S. Rahiminejad, E. Pucci, S. Haasl, and P. Enoksson, "Evolution of Pin-Flange Adapters for High Frequency Measurements," In Proceedings of the *9th European Conference on Antennas and Propagation*, EuCAP 2015, Lisbon, Portugal, 12-17 April 2015.
- S. Rahiminejad, E. Pucci, S. Haasl, and P. Enoksson, "Evolution of Pin-Flange Adapters for High Frequency Measurements" *The 18th International Conference on Solid-State Sensors, Actuators and Microsystems*, Anchorage, United States of America, June 21-25, 2015.
- S. Rahiminejad, P. Cegielski, M. Abbasi, and P. Enoksson, "A Four Level Silicon Microstructure Fabrication By DRIE," *MME 2015, 26th Micromechanics and Micro Systems Europe Workshop*, Toledo, Spain, September 20-23, 2015.
- S. Rahiminejad, A. U. Zaman, S. Haasl, P.-S. Kildal and P. Enoksson, "Micro-machined Linear Slot Array Antenna for 100 GHz with 10 dB Gain Using GAP Waveguide Technology," *10th European Conference on Antennas and Propagation*, EuCAP 2016, Davos, Switzerland, 10-15 April 2016.
- S. Rahiminejad, E. Pucci, S. Haasl, P.-S. Kildal and P. Enoksson, "AMC pin waveguide flange for screw redundant millimeter and sub-millimeter measurements," *87th ARFTG Conference Measurements for Emerging Communications Technologies*, 27th May, 2016.
- S. Rahiminejad, E. Köhler and P. Enoksson, "Direct 3D printed shadow mask on Silicon," *MME 2016, 27th Micromechanics and Micro Systems Europe Workshop*, Cork, Ireland, August 28-30, 2016.

Contents

Abstract	ii
Acknowledgements	xii
1 Introduction	1
1.1 RF-MEMS	2
1.1.1 Switches	2
1.1.2 Varactors	4
1.1.3 Resonators & Filters	4
1.1.4 Packaging	4
1.2 Transmission Lines and Waveguide Technologies	5
1.2.1 Rectangular Waveguides	5
1.2.2 Microstrip lines	6
1.2.3 Substrate integrated waveguide (SIW)	6
1.2.4 Photonic crystals	7
1.2.5 Gap Waveguides	8
1.3 Microstrip-to-Rectangular Waveguide Transitions	8
1.4 Planar Antenna Technology	10
1.4.1 Microstrip antennas	10
1.4.2 SIW antennas	11
1.4.3 Waveguide slot array antenna	11
1.4.4 Gap waveguide antennas	12
1.5 Thesis Objective	13
2 Microfabrication	15
2.1 Lithography	15
2.2 Deep Reactive Ion Etching	17
2.2.1 Basic principle	17
2.2.2 STS ICP	18
2.2.3 Centura II	21

2.2.4	Comparison of the STS ICP machine and the Centura II	22
2.3	Sputtering	22
2.4	Electroplating	23
2.5	Utilizing SOI Wafers	24
2.6	SU8	24
2.7	Carbon Nanotubes	26
3	Gap Waveguide Theory	29
3.1	Hard and Soft Surfaces	29
3.2	Bed of Nails	31
3.3	Ridge Gap Waveguides	35
3.4	Groove Gap Waveguides	35
3.5	Resonators, Q-factors and Losses	36
4	Devices	39
4.1	280 GHz Ridge Gap Waveguide and Resonator	39
4.1.1	Si ridge gap resonator and waveguide	39
4.1.2	SU8 ridge gap resonator	45
4.1.3	Carbon nanotube ridge gap resonator	48
4.1.4	Discussion	50
4.2	Gap Adapters	52
4.2.1	280 GHz gold plated brass prototype	54
4.2.2	280 GHz micromachined Si gap adapter	58
4.2.3	280 GHz micromachined SU8 gap adapter	60
4.2.4	Discussion	65
4.3	100 GHz Gap Waveguides	66
4.3.1	100 GHz Groove Gap Waveguides	68
4.3.2	100 GHz Ridge Gap Waveguides	72
4.3.3	Discussion	75
4.4	H-bend Rectangular Waveguide-to-Microstrip Transition	77
4.4.1	Discussion	81
4.5	100 GHz Ridge Gap Waveguide Antenna	81
4.5.1	Discussion	85
5	Conclusion	87
6	Outlook	91
	Bibliography	92

Acknowledgements

I would like to express my deepest gratitude to Professor Peter Enoksson, it has been a pleasure to have him as my supervisor during the past few years. I have learnt a great deal from him. I cherish the responsibility, trust and enthusiastic encouragements that he has given me.

Also, I would like to acknowledge my former co-supervisor Professor Per-Simon Kildal for sharing and involving me in his vision for gap waveguides. For his support and time, helping me explore this new field, and for always making me feel welcome in the antenna group. He is truly missed.

My co-supervisor Dr Sjoerd Haasl has my great appreciation. Even though he is located in another city, he always takes time to help me and to guide me, whether it is cleanroom related or paper related he goes beyond my expectations.

Thanks to my friends and colleagues within the group for fruitful discussions and pleasant company and also to my friends at MC2. Thanks to the Antenna group over at S2 for all their support, guidance and contribution to my work and for including me in their group.

I would also like to extend my thanks to the technicians of the Nanofabrication Laboratory for their help whether it was big or small. A great thanks to Carl-Magnus Kihlman and Mats Myremark for providing all the great milled structures used in this work.

Thanks to the Microwave Electronics Laboratory and Jörgen Stenarson, for their support and help with their measurement equipment, which without them, I could not verify our work.

There are some people that deserves my special thanks: my parents for their support and encouragement, my sister for making me laugh and keeping me on my toes, Tobias for inspiring me to excel, and The Girls for reminding me what is important in life.

Göteborg, December 2016
Sofia Rahiminejad

Acronyms

AMC	Artificial Magnetic Conductive
CNC	Computer Numerically Controlled
CNT	Carbon Nanotubes
CVD	Chemical Vapor Deposition
DARPA	Defense Advanced Research Projects Agency
DC	Direct Current
DRIE	Deep Reactive Ion Etching
EDM	Electrical Discharge Machining
FBAR	thin Film Bulk Acoustic Resonators
ICP	Inductive Coupled Plasma
LTCC	Low Temperature Co-fired Ceramic
MMIC	Monolithic Microwave Integrated Circuit
PCB	Printed Circuit Board
PEB	Post Exposure Bake
PEC	Perfect Electric Conductive
PMC	Perfect Magnetic Conductive
PNA	Performance Network Analyzer
RF	Radio frequency
SEM	Scanning Electron Microscope
SIW	Substrate Integrated Waveguide
SOI	Silicon On Insulator
TE	Transverse Electric
TEM	Transverse electromagnetic
TM	Transverse Magnetic
UHF	Ultra High Frequencies

Introduction

As today's wireless technology is evolving, the need for increasingly high frequencies is imperative. Higher frequencies offer wider bandwidth and higher spatial resolution. Also, since microwaves travel by line of sight and can therefore go through the ionosphere, these frequencies are very suitable for satellite communications [1].

High-frequency technology has made advances in areas such as automotive radar at 24 GHz and 77 GHz (right now competing frequency bands), which are used to recognize the traffic scenario around the vehicle, and can be used in advanced driver assistance systems (ADAS) [2]. Since higher frequencies provide wider bandwidths, wireless communication can transmit at higher and higher data rates, thus high data media can be available wirelessly. Some examples of the current and future video qualities and the data rate needed: uncompressed HD video, 1.5 Gbit/s , 4K video, 6 Gbit/s , 3D video, 12 Gbit/s , and Super Hi-Vision, 24 Gbit/s [3]. The high spatial resolution possible with higher frequencies can be used to obtain an image even at night, during fog or smoke [4]. High frequency technology has today developed full-body mm-wave scanners at $27 - 33\text{ GHz}$, now used at airports to detect concealed weapons on people, and is a safer method than X-ray scanning [5]. The technology has evolved, and scanners working at E-band ($70\text{-}80\text{ GHz}$) have also been presented [6]. Full-body mm-wave scanners have also been developed at ultra high frequencies (UHF) for the fashion and apparel industry, where a full 3D image of the customers body can be used to see how garments will fit [7]. Also, the field of medical diagnostics has progressed with the help of microwave technology. Mammography, which is commonly used to detect breast cancer is a debatable method: it is uncomfortable, and it fails to detect breast cancer in 15% [8] of the cases [9]. Microwave imaging can offer higher contrast (at frequencies up to 10 GHz) during scanning and would be more a comfortable approach [9, 10]. Millimeter waves are more suitable for high spatial resolution applications due to their high sensitivity to detect pathological changes [11]. For example F. Töpfer et al present a micro-machined near-field probe at 100 GHz for high-resolution skin measurements [12].

As microwave technology is evolving and reaching millimeter and sub-millimeter wavelengths, so does the dimension of the components used in these systems. Planar technologies as microstrip lines and coplanar waveguide are being used at $300\text{ MHz} - 100\text{ GHz}$ and the low-loss rectangular waveguides are being used more and more for frequencies ranging between $30\text{ GHz} - 3\text{ THz}$. However, standard fabrication technology is limited by the dimensions at these frequencies to produce both passive and active components. Micromachining or MEMS (Micro-Electrical-Mechanical-Systems) technology can offer a solution how to fabricate small compact components and push microwave technology to higher frequencies.

1.1 RF-MEMS

The RF MEMS research field can be divided into four areas [13]: 1) RF-MEMS switches, varactors and inductors, 2) Micromachined transmission lines, high-Q resonators, filters and antennas, 3) FBAR (thin Film Bulk Acoustic Resonators) and filters, and 4) RF micromechanical resonators and filters. In this section, we will discuss the first and second research areas of RF-MEMS.

1.1.1 Switches

MEMS-based sensors have been developed since the 1970s [13]. The most common RF MEMS device, the switch, was introduced in the 1980s but did not have any application until Dr Larry Larson designed the first MEMS switch with a specific microwave application in 1991, financed by DARPA [13]. This switch was placed on a rotor and rotated to the desired circuit connection [14]. The field started to take off after his publication [14] and new applications such as phase shifters [15], filters [16] and tunable antennas [17] started surfacing.

A MEMS switch can create a short circuit or an open circuit by lateral or vertical movement and can be connected either in series or as a shunt. The switch, unlike the transistor has distinct on and off positions without any leakage. The switch can be actuated with several methods: electrostatic actuation [18–20], where the beam is drawn by electrostatic force to close the circuit, magnetostatic [21] where the beam is moved by magnetic force, thermally [22] where a thermal film is placed on the beam and deforms the beam when heated with a current, and piezoelectrically [23] where a piezoelectric film is placed on the beam, expanding or contracting by an applied voltage, Fig. 1.1.

The most common structures for the vertical switches are the fixed-fixed beam and the cantilever (Fig. 1.2), which can operate by metal-to-metal contact or as a capacitive switch. These structures are often surface micromachined and are the most common switch configuration of the past decades [24]. According to Ai Qun Liu, the lateral

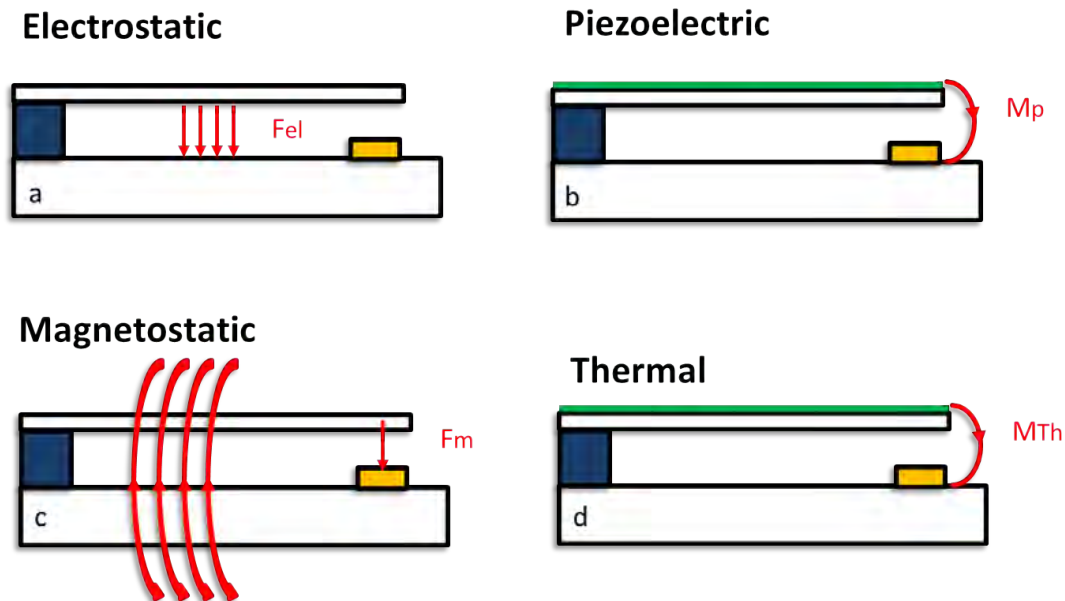


Figure 1.1: Different actuation methods for switches. a) electrostatic, b) piezoelectric actuation with a piezoelectric film (green) on the cantilever, c) magnetostatic and d) thermal with a thermal bimorph cantilever.

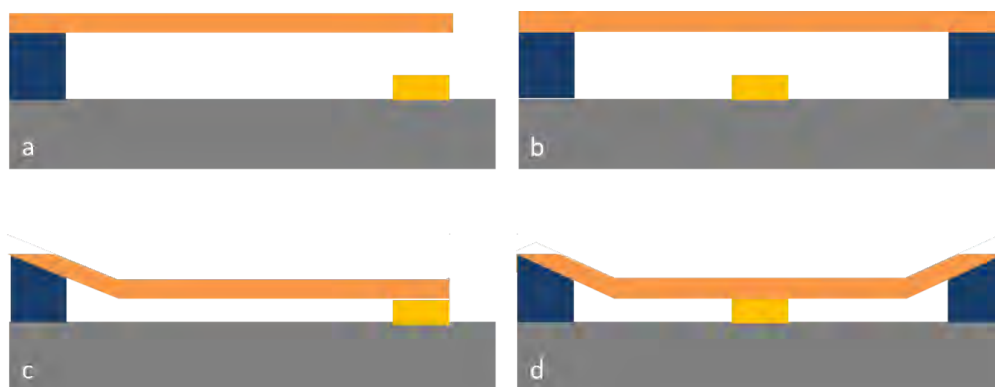


Figure 1.2: Vertical switch configurations. a) cantilever beam in up state, b) fixed-fixed beam in up state, c) cantilever in down state, d) fixed-fixed beam in down state.

switch, though not as common as the vertical switch, has shown potential in their dynamics performance and the simple fabrication process they can offer [24]. Lateral switches are bulk micromachined and therefore have fewer lithography steps, there can be as few as only one lithography step.

1.1.2 Varactors

One of the benefits of RF MEMS is the ability to tune one's system to e.g. different frequency ranges, without multiple sets of components. Tunable systems can be used in e.g. phase shifters and tunable antennas.

One of the tunable components that exist is the Varactor (variable capacitors). Varactors can be used to tune the center frequency, and the channel bandwidth, among other circuit characteristics. Most vertical MEMS varactors have the same mechanical structure as a vertical MEMS switch (Fig. 1.2), however now the variance in distance between the beam and the contact vary the capacitance of the system. Varactors can also be found in lateral configuration, like the switch e.g. a comb-drive structure [25]. Another configuration was shown in [26] implementing vertically aligned carbon nanotubes and carbon nanofibers. By being reconfigurable, they can reduce both cost and space, however no MEMS varactor exists for commercial applications yet. The commercially available varactors today are reverse-biased semiconductor diodes. Varactors can be used together with other components to make new devices. In [27] a varicap (also known as a varactor) is used together with a high-Q spiral conductor to create an LC-tank tunable resonator.

1.1.3 Resonators & Filters

MEMS resonators are mechanical resonators actuated by an electrical signal and can achieve much higher Q-values than a passive electronic resonator [28]. MEMS resonators are used in e.g. filters, reference oscillators and mixers. The mechanical structure is actuated most commonly electrostatically or piezoelectrically, which induces a mechanical resonance which vibrates in one or several modes. Then, the mechanical resonance is converted to an electrical signal again with a transducer that senses the mechanical movement. MEMS resonators come in many structures with movements both in vertical and lateral directions. The most common structures are the clamped-clamped beam [29], the free-free beam [30], the comb-drive [31] and the ring resonator [32]. Waveguide filters can also be tuned with MEMS-switches. In [33], a MEMS switch is placed inside a cavity resonator to disturb the current distribution inside the cavity to tune the resonance frequency.

1.1.4 Packaging

To be able to use MEMS devices in commercial applications they need to be protected from e.g. moisture, gases and impact. There are different ways of packaging a MEMS device but also at different levels. The chip can be packaged already at wafer level and is then protected during dicing but it can also be packaged after the chip has been diced. One way of packaging RF MEMS devices is through flip-chip technology [34].

1.2 Transmission Lines and Waveguide Technologies

A key component in microwave systems are transmission lines and waveguides, and their ability to transmit microwave power [1]. There are many different technologies, such as the hollow waveguide which has low loss but is expensive to manufacture, and it often has a bulky structure. Transmission lines that can be fabricated with printed circuit board technology such as striplines, microstrip lines, coplanar waveguides, and recently, substrate integrated waveguides (SIW) are compact and can be fabricated at a low cost. At higher frequencies waveguides that utilize metamaterials are of interest, like photonic crystals and gap waveguides. In this section, the above mentioned technologies suitable for high frequencies, will be discussed. Striplines, microstrip lines, and coplanar waveguides are similar technologies, therefore only the microstrip line will be discussed.

1.2.1 Rectangular Waveguides

The most common waveguide for high-frequency applications, is the hollow waveguide, Fig. 1.3. The idea of a hollow waveguide was first discussed by Heaviside, and rejected by himself in 1893 [35]. Lord Rayleigh approached the topic again in 1897 and proved mathematically that guiding waves through tubes was possible [36]. The hollow waveguide did not become of interest until World War II, and two men (G.C. Southworth and W. L. Barrow) independently presented papers with experimental results at the same meeting in 1936 [1]. The hollow waveguide consist of solid connected electrically conductive walls, either with a circular shape or a rectangular shape. These waveguides have the lowest loss because they are completely shielded and only have conduction losses in the sidewalls. Hollow waveguides require full electrical contact between the walls. At high frequencies, the size of the waveguides makes them difficult to assemble, and the sensitivity to misalignment and gaps is high. Hollow waveguides are also bulky in comparison to other waveguides and transmission lines.



Figure 1.3: Image of a rectangular waveguide.

1.2.2 Microstrip lines

Microstrip lines are fabricated with printed circuit board technology (PCB). It is similar to the earlier stripline and the later coplanar waveguide. The benefit with all these technologies is that the components can be placed on top of the circuit board. It was first presented by D. D. Grieg, and H. F. Engelmann in 1952 [37]. A microstrip line consists of a metal strip on top of a dielectric board with a metal ground plane, as shown in Fig. 1.4. The wave travels between the two metal surfaces. Here there are dielectric losses and because the wave is not enclosed as within a rectangular waveguide, the wave can be interfered from the outside. A microstrip line can also have surface waves leaking out into the substrate.

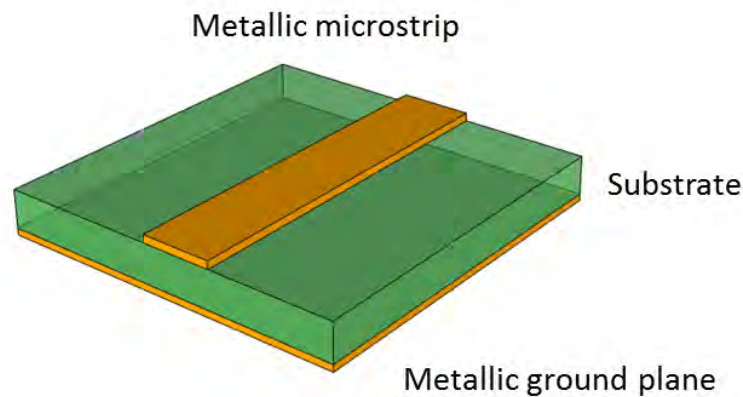


Figure 1.4: A sketch of a microstrip line

1.2.3 Substrate integrated waveguide (SIW)

In 1998, Hirokawa et Al. presented a so called post-wall waveguide used to feed a parallel-plate slot array, [38]. The post-wall waveguide can be made with PCB technology, and consist of via holes, so called posts used to contain the wave. In 2003 Wu et Al. [39] presented a similar type of microwave waveguide under another name, the substrate integrated waveguide (SIW), Fig. 1.5. The design is similar to that of a rectangular waveguide. A dielectric slab is sandwiched between two metal plates and instead

of solid conductive walls, there are conductive vias or posts connecting the top metal plate with the metal bottom plate. The height of the SIW is lower than that for a hollow rectangular waveguide. This design still needs full contact between the bottom plate and the top plate through the vias. The SIW are filled with a dielectric and therefore there are dielectric losses. However, the loss is less than for a microstrip line, due to the sidewalls.

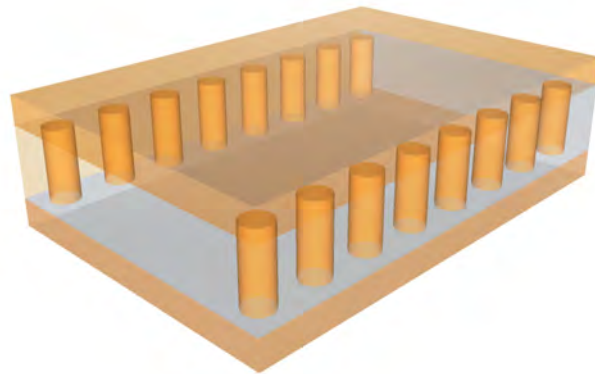


Figure 1.5: The SIW displayed, showing the conducting via holes and the conducting plates.

1.2.4 Photonic crystals

When going up in frequencies, into the optical spectrum, optical fibers are the dominating way to guide the wave. Another way to guide light is to use a photonic crystal (Fig. 1.6). This technique is based on alternating materials with different dielectric constants. Other forms of photonic crystals were already discussed in 1887 but it wasn't until 1987 that two papers [40,41] changed the field. E. Yablonovitch intended to control the spontaneous emission by atoms, by using a photonic crystal [40] and S. John used photonic crystals to control light [41]. The research on photonic crystals increased exponentially after their initial work but there was still the issue of fabricating photonic crystals. Microfabrication processes have been very useful for this application by using lithography and etching techniques to create these photonic structures.

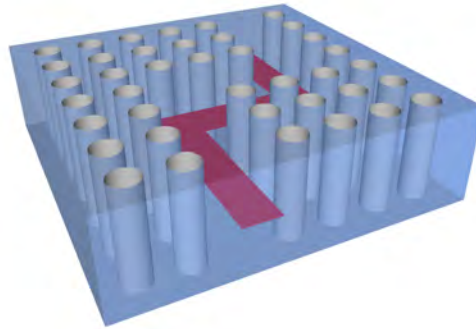


Figure 1.6: The photonic waveguide showing the holes with gaps and the light (red) traveling between.

1.2.5 Gap Waveguides

One issue with rectangular hollow waveguides when going up in frequency is that even the smallest gap will create large leakages. Gap waveguide technology does not have this issue due to that it is based on having two parallel plates and utilizes metamaterials to create a stop band to confine the wave. Gap waveguides were first presented in 2009 and exist in three varieties, ridge, groove and microstrip gap waveguides [42, 43]. In 2010, the first realized gap waveguide for 10 – 20 GHz was presented [44]. Since then a variety of different gap waveguide devices has been presented, such as packaging of microstrip circuits [45], microstrip filters [46], groove gap based filters [47], and an MMIC amplifier [48].

1.3 Microstrip-to-Rectangular Waveguide Transitions

Although rectangular waveguides with their low loss, are often used for high-frequency applications, microstrip lines and other planar transmission lines are easier to integrate with microwave circuitry. Therefore, it can be useful to have a microstrip-to-rectangular waveguide transition.

There have been many different microstrip-to-rectangular waveguide transitions. One of the earlier versions had a ridge-to-microstrip junction [49]. The ridge would end with a stair-like structure that acted as an impedance transformer to the microstrip line, Fig. 1.7. The most common transition is to insert part of the microstrip line into the rectangular waveguide, either facing the direction of propagation or transverse (Fig. 1.8) [50–52]. These transitions often have a back-short behind the microstrip line to maximize the transmitted power. A back-short is a cavity, less than a quarter of wavelength long, behind the microstrip probe to reflect electromagnetic energy back towards

microstrip probe. The probe design can also affect the power, with e.g. coplanar waveguides instead [53, 54], or with a Yagi-like antenna [55].



Figure 1.7: Schematic cross-section view of a ridge-to-microstrip junction

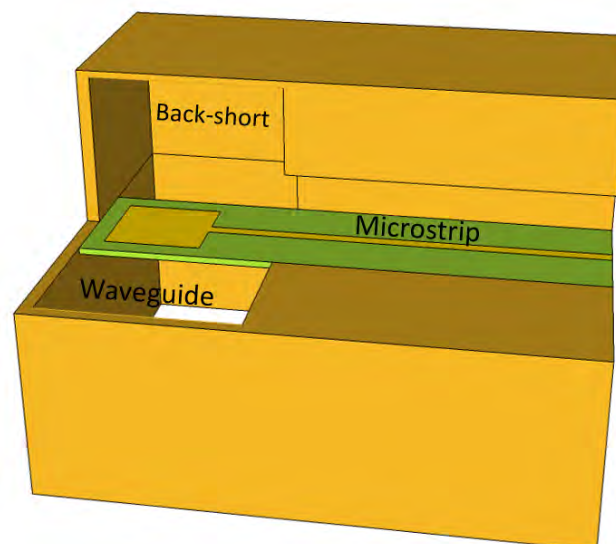


Figure 1.8: Schematic view of a microstrip-to-waveguide transition, with the top cut in half .

The previous presented transitions use milled rectangular waveguides, which is easy to integrate with at lower frequencies, and more difficult at higher frequencies due to the small tolerances for misalignments. Therefore, at higher frequencies, micromachined waveguides and sometimes also integrated micromachined microstrip lines are explored. An example of a micromachined transition is the finite ground coplanar line-to-silicon micromachined waveguide transition in [56], operating at 90 – 110 GHz. The waveguide was a diamond waveguide, easily fabricated with wet Si etching. Another ex-

ample is the coplanar waveguide-to-rectangular waveguide transition, presented in [57], where both the rectangular waveguide and the coplanar waveguide are micromachined.

1.4 Planar Antenna Technology

Planar antennas are of interest for high-frequency applications when the antenna needs to have high gain but still fit in a small confined planar space. Planar antennas are often based on waveguide and transmission line technology, for both the feed and sometimes even the radiating surface. In this section, the most common planar antenna technologies based on the transmission line and waveguide technologies: microstrip line, SIW, rectangular waveguide, and gap waveguide technology (section 1.2) are discussed.

1.4.1 Microstrip antennas

Microstrip antennas are fabricated with PCB technology, they can therefore be produced at a relatively low cost, Fig. 1.9. The radiating patch can be excited by a microstrip feed, a coaxial probe or coupled via an aperture between the patch and the microstrip line [58]. As microstrip antennas are based on microstrip line technology (see section 1.2.2) and have therefore the same benefits and problems. They are light weight, they can be integrated with active electronics, and the feed lines can be fabricated in the same process. And just as microstrip lines, they also suffer from dielectric losses, ohmic losses and surface waves. They also have a narrow bandwidth and difficult to have polarization purity (that is a high ratio of the desired polarization component to the undesired component) [59].

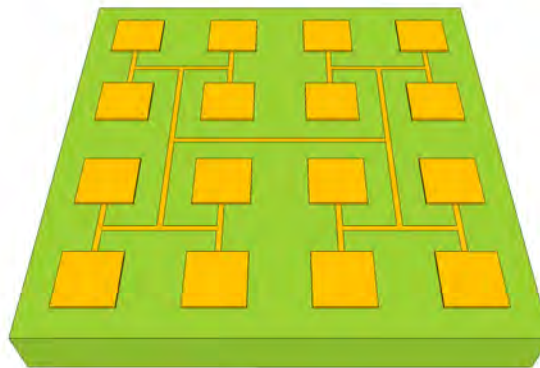


Figure 1.9: A microstrip array antenna.

1.4.2 SIW antennas

SIW antennas are fabricated with PCB technology, which makes them compact and easy to fabricate. The metallic via holes confine the wave with a larger metallic surface compared to the microstrip line antenna, and therefore, they have less ohmic losses than a microstrip line antenna [60]. The SIW antenna does not suffer from surface waves like the microstrip antenna, which reduces crosstalk in an antenna array. Since the SIW have attributes in common with both the microstrip line and the rectangular waveguide, the SIW antenna has a wide design freedom. The SIW antenna can be designed like a microstrip line antenna with patches, but also like a slot waveguide antenna (Fig. 1.10) [61]. Other examples include leaky wave antennas [62, 63], and even Vivaldi antennas [64].

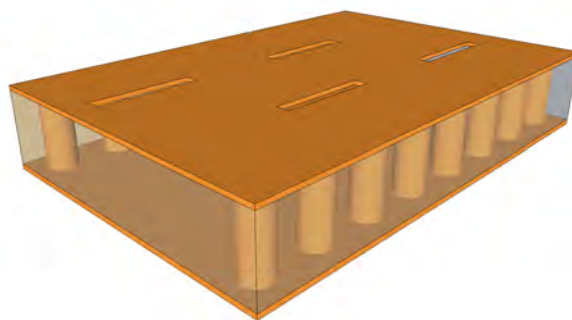


Figure 1.10: An SIW slot antenna.

1.4.3 Waveguide slot array antenna

When shielding electronic equipments, metal boxes are used. These boxes cannot have any openings, or they will leak out the power. This, however, can be used when designing an antenna. There are different ways to excite a slot, for example by applying a voltage over the slot, this however is a complicated and bulky setup, by connecting a rectangular waveguide directly to the slot, and by a plane incident wave [58]. The last way is what is used in a waveguide slot array antenna. By cutting slots into a rectangular waveguide (Fig. 1.11), the slots are excited by the transmitted wave inside the waveguide. By placing these waveguides in an array, a waveguide slot array antenna is formed. Waveguide slot array antennas designed for low frequencies are easily fabricated by milling metal. However, at high frequencies slot waveguide antennas are bulky and difficult to fabricate compared to microstrip antennas and SIW antennas, but they do

not suffer from dielectric losses, and they have relatively low ohmic losses. To integrate with an electronic component, a transition structure is needed. Also, at higher frequencies, the dimension of the walls needed are not mechanically stable. Therefore, they are not often used for high frequency applications.



Figure 1.11: A slot waveguide antenna.

1.4.4 Gap waveguide antennas

The first gap waveguide antenna designed and fabricated was a milled ridge gap waveguide antenna operating at 12 – 15 GHz, [65]. Later, gap waveguide technology was used together with SIW technology to design feed networks and cavities in multilayer planar antennas for higher frequencies, as in [66] where a PCB fabricated microstrip gap waveguide feed network was used at 60 GHz, or in [67] where an LTCC (Low temperature co-fired ceramic) gap waveguide feed network was used at 75 – 110 GHz. In 2016 a simulation comparing a multilayer planar antenna based on the different gap waveguide technologies, the ridge gap waveguide, the groove gap waveguide or the inverted-microstrip gap waveguide feed network was presented [68]. The three antennas had good impedance bandwidth and also good radiation patterns, however, the inverted-microstrip gap waveguide antenna was a little bit more lossy than the other two technologies. There have been many designs for planar antennas, solely based on gap waveguide technology. Groove gap waveguide antennas have so far only been simulated for 20 GHz [69], and 60 GHz [68, 70]. Ridge gap waveguide antennas have both been simulated [68, 71], and fabricated by either milling [72] or by Die-sink EDM (electrical discharge machining) [73]. However, even gap waveguide antennas are limited when fabricated by traditionally methods. To reach higher frequencies, new fabrication methods need to be used.

1.5 Thesis Objective

The development of microwave commercial devices are reaching the limit when approaching frequencies above 60 GHz. Microwave devices with small dimensions, and with the requirement of low loss and high precision have become an issue when fabricating with conventional methods. Micromachining or MEMS processing or, as referenced in this work, microfabrication, on the other hand can offer high resolution fabrication.

This thesis presents the development of microfabrication for gap waveguide devices above 90 GHz. Gap waveguides are especially suited for high-frequency applications since they can function very well even with gaps, so complicated and highly costly welding or diffusion bonding can be avoided. The thesis also presents a microfabricated microstrip-to-rectangular waveguide transition operating at 140 – 220 GHz.

The thesis includes the following chapters:

Chapter 1 introduces the field of microwave technology, RF MEMS, existing transmission line and waveguide technologies, waveguide-to-microstrip technologies and planar antenna technologies. The chapter ends with a thesis objective.

Chapter 2 discusses the various microfabrication techniques used to fabricate these devices. Microfabrication is not a straight forward approach. This chapter also presents the optimization processes of some of the microfabrication techniques.

Chapter 3 introduces gap waveguide theory, which covers soft and hard surfaces, the concept of the metamaterial "bed of nails" used for gap waveguides, the ridge gap waveguide, the groove gap waveguide, inverted-microstrip gap waveguides and gap waveguide resonators.

Chapter 4 presents first the 280 GHz ridge gap waveguide and resonator fabricated in Si. The ridge gap resonator can be used to determine losses, and therefore the design was also used to evaluate other materials as base material such as the polymer SU8 and carbon nanotubes (CNTs). When measuring on the 280 GHz ridge gap waveguide devices, the authors noticed how sensitive to gaps the measurement equipment is at these frequencies. A gap adapter was developed so that high frequency measurements could be performed without the requirement of full electrical contact between the measurement equipment and the device under test. This gap adapter was optimized with regard to the design, fabrication method and material used. Then the 100 GHz groove and ridge gap waveguide devices are presented. The groove gap waveguide device has the advantage of being able to directly be connected to a rectangular waveguide. The ridge gap waveguide needed a novel coplanar-to-ridge gap waveguide transition. Another transition is also presented, a fully micromachined microstrip-to-rectangular waveguide transition, which can be used for MMIC coupling to antennas. The last part of this chapter presents a fully micromachined ridge gap waveguide antenna. All devices are discussed after they are presented.

Chapter 5 presents an overall conclusion of the thesis.

Chapter 6 presents an outlook for future work.

Microfabrication

In this chapter, all the process steps used during the fabrication of the different devices presented in chapter 4, will be described. At some of the process steps, optimization studies were done to determine the different parameter values to get the desired results. These studies are also presented here.

2.1 Lithography

In microfabrication, lithography is the process used to pattern a wafer. The basic principle is to pattern a photo resist with an energy source. Often, the photo resist is used to pattern a thin film on the wafer to create a so-called etch mask. The etch mask, is in turn used to protect the areas of the wafer which should not be etched. In some cases the photo resist itself can be used as an etch mask.

To distribute the photo resist onto the wafer, a spinner is used. The photoresist is dispensed onto the wafer, this can be done by using a pipette, an automatic dispenser or even a syringe. The wafer is then spun to distribute the photoresist over the entire wafer. The thickness of the photoresist layer depends on the viscosity of the photoresist, the rotation speed of the spinner and the duration of the process. To improve the photo resists adhesion to the wafer a primer such as HMDS (hexamethyldisilazane) can be spun onto the wafer before the photoresist.

The wafer is then soft baked at an elevated temperature to evaporate the solvent in the photoresist. The soft bake temperature depends on which photoresist is used, and it can range from $90^{\circ} C$ to $150^{\circ} C$.

To pattern the photo resist, the photo resist needs to be exposed to an energy source, depending on if the photoresist is negative or positive, the polymers in the photoresist will bind stronger, or the polymer bonds will break, where it has been exposed. The weakened areas will then be dissolved more easily with an alkaline solution.

The most common exposure method, direct UV-lithography illuminates the wafer through a photo-mask, which is the method used in this thesis. However, there are other methods, such as using an electron-beam that directly writes the pattern into the photo-resist. By using an electron-beam, the resolution can be as low as a few nanometers. Another common method, is to use direct laser writing, that uses laser diodes in an array, to scan the wafer and pattern the photo resist. Direct laser writing, can offer a resolution in the sub-micrometer range. The benefit of using direct writing lithography like electron-beam and laser writing, is that it offers fast turnovers of designs. The downside is that each chip needs to be exposed one at a time, which is time consuming and not suitable for mass fabrication. Direct UV-lithography, exposes the entire wafer at once, and is therefore much faster.

A photomask is generally a chrome-coated glass or quartz plate that has been patterned with the help of a laser electron-beam mask generator and photoresist. This can be used to define the pattern on the wafer. When illuminating the photomask with UV-light the clear areas will let the UV-light through and expose the photoresist on the wafer below. However, if the requirement of the resolution of the pattern is low, a repro-mask (masks printed on plastic film) can be used instead, which are available at a low cost.

Direct UV-lithography have three exposure approaches: proximity, contact, and projection exposure. Proximity exposure allows the mask to have no contact with the wafer. The resolution will be slightly lower depending on the gap between the mask and the wafer. The larger the gap, the lower the resolution will be. However, the mask lifetime will be longer. Contact exposure is when the mask is pressed against the wafer during exposure, giving good resolution. Projection exposure uses a UV lens between the mask and the wafer, allowing the same resolution as for contact exposures without contact and longer distances from the wafer. During the lithography steps of the presented work in chapter 4, contact mode was used if a chrome mask was used. However, when working with repro-printed masks proximity exposure was used due to the sensitivity of the print.

After developing the photo resist in an alkaline solution, the photo resist can be hard baked, by placing the wafer in an oven or on a hot plate for an appropriate time depending on the photoresist and its thickness. If an oven is used, then typically 30 *min* to an hour at 120° C.

The resolution of direct UV-lithography depends on the thickness of the photo resist and how much energy was used during exposure. The development time and agitation during development, also affects the resolution of the wafer. Therefore each lithography process needs to be optimise depending on the photo resist thickness, exposure energy, photo mask, development time and the amount of agitation.

2.2 Deep Reactive Ion Etching

This section presents the basic principle of deep reactive ion etching (DRIE), one of the most common bulk microfabrication processes. The optimisation process of the recipes on the ICP STS machine at Chalmers University of Technology are presented, and also etch tests performed on the Centura machine at The Royal Institute of Technology. The two machines are compared to each other when it comes to etch rate, under etch, and surface roughness.

2.2.1 Basic principle

To etch deep into silicon, that is depths more than $2\ \mu\text{m}$ down to $2\ \text{mm}$, DRIE is used. The basic principle of plasma etching is to supply a gas into a vacuum chamber, make a plasma and accelerate ions through the gas using an electric field. When the ions are accelerated through the plasma they collide with the gas molecules and electrons. The energy from the collisions ionizes the gas more and increases the amount of ions and electrons. This continues until breakdown occurs, this voltage is called the Townsend discharge. The ions from the gas are directed towards the wafer by an electric field, and remove atoms from the wafer either mechanically and/or chemically.

The plasma can be created in different ways, in this work, inductive coupled plasma (ICP) is used. ICP is induced by a coil around the chamber. Through the coil, an RF current causes an alternating magnetic field. The changing magnetic field produces an alternating electric field circulating in the gas. The fast moving electrons collide with the slow ions and produce more ionizations. ICP plasma generates relatively high density plasma.

The two most known anisotropic dry etch methods are cryogenic etching and the Bosch process. The anisotropic etch method used here is the Bosch process. The Bosch process is an alternating process between isotropic plasma etching and applying a passivation layer. First, isotropic plasma etching with the gas SF_6 is done for a certain etch time. Then, the gas C_4F_8 is pumped into the chamber, the C_4F_8 is braked down to C_4F_x ions which covers all sides of the now isotropic trench in the wafer with a Teflon-like film. When etching again the plasma is mostly focused downward by an electric field (the platen power) and the plasma etches through the passivation in the bottom, but the passivation layer on the sides is not that much affected. When alternating between etching and passivation, a scalloped wall occurs. The unevenness of the walls depends on for how long each etch step is and how much passivation is used. The amount of passivation is determined by how long the passivation time is. If there is a build up of passivation or other residues due to insufficient etching then grassing or so called black Si can appear.

The DRIE is also affected by which etch mask is used. The etch mask needs to have a selectivity to the Si so that it survives the entire etch process. An extensive study of

etch mask and their selectivity to different substrates is presented in [74]. Oxide has a high selectivity to Si (about 1:100), however, the edges of the oxide are also etched during the process, and the resolution is affected. Metal etch mask can withstand the etch process almost completely, however, re-sputtering of the metal into the trenches which may result in black Si. Photoresists can also be used as an etch mask, with not as good selectivity to Si (about 1:65), and larger lateral etch than oxide, however, it is easy to pattern, and by using a photoresist as an etch mask removes a process step.

2.2.2 STS ICP

When applying DRIE to generate the structures with the STS ICP machine, four parameters can be tuned depending on the structures. The four parameters are: the etch time, the passivation time, the pressure and the platen power.

The etch and passivation times affect the surface of the walls and the anisotropy. By increasing the platen power, the electric field will increase, this results in transmitting more energy to the ions. The etch will become more mechanical than chemical and the hard-masks selectivity is decreased. The increase of the electric field will also increase the speed of the ions toward the wafer. The pressure in the chamber is controlled by a throttle valve. The pressure control can be automatic, or manual. The manual control locks the valve at a position, this is expressed in percent 0.1 – 100% which corresponds to an angle, 0.1 – 90°. The pressure control thus determines the gas flows of the SF_6 gas and the C_4F_8 gas. The increase of pressure have two opposite effects. The first is that there are more electrons and ions that can collide with each other, which leads to more free ions. However the mean free path of the electrons and ions before collision is reduced and the electron has less energy before colliding.

When etching high aspect ratio structures, the etch parameters need to be altered depending on the height of the aspect ratios of the structures, and the layout of the photomask that is used. Every mask will etch differently. In Tab. 2.1, five different recipes that have been evaluated and tested on the same mask with the STS ICP plasma etch are presented.

Table 2.1: Etch recipes that have been tested and evaluated. The parameters that were altered are the etch time, the passivation time, the automatic pressure control and the platen power. The average etch rate throughout the wafer is also presented.

Recipe name	SF6 (sccm)	SF6 (sec)	C4F8 (sccm)	C4F8 (sec)	Pressure Control	Platen power (W)	Average etch rate
SIFASTO	130	12+1	85	7+0.5	55%	10	2.5 $\mu m/min$
SRFASTO1	130	12+1	85	10+0.5	55%	12	2.6 $\mu m/min$
SRFASTO2	130	10+1	85	10+0.5	55%	12	Black Si
SRFASTO3	130	9+0.5	85	7+0.5	55%	12	1.9 $\mu m/min$
SRFAST1	130	10+0.5	80	7+0.5	68%	20	2.7 $\mu m/min$

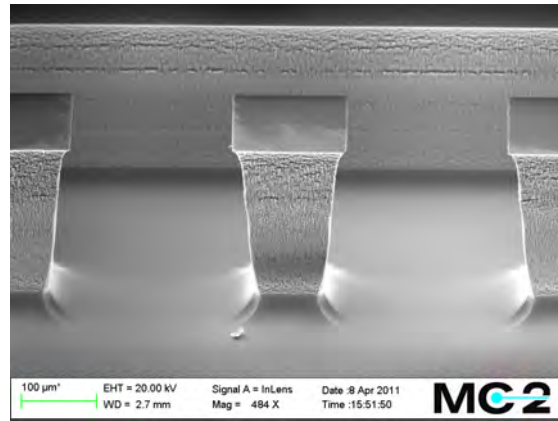


Figure 2.1: SEM image of one of the pins etched out for 280 GHz

The default recipe (SIFASTO, Tab.2.1) was used for the structures described in section 4.1 and appended Paper I, where pins with a height of $277 \mu\text{m}$ and a width of $165 \mu\text{m}$ needed to be etched. The total variation of the pin height over a 6" wafer was $\pm 10 \mu\text{m}$ of the desired pin height. As can be seen in Fig. 2.1, the walls of the pins are tilted inwards. This structure is similar to that of an inverted pyramid, which can increase the bandwidth, mentioned in section 3.2. Therefore, the slope is not a problem in this case.

When etching structures with a pin-height of $750 \mu\text{m}$ on the other hand as in section 4.3.2 and in the appended papers III, IV and IX, the slope of the sidewalls matter. The reason is that if the slopes are too large, the pins will eventually get cut off. To calculate the angle α of the pin wall (Fig. 2.2), the under etch b and the height h of the pins were measured, and α was calculated with the expression $\alpha = \arctan(h/b)$.

The structures in section 4.3.2 have pins with a width of $150 \mu\text{m}$, $300 \mu\text{m}$ and $450 \mu\text{m}$. The $150 \mu\text{m}$ wide pins are the most crucial ones. If the angle is smaller than 84.29° when the etch depth is $750 \mu\text{m}$, the pin was etched $75 \mu\text{m}$ from each side, the $150 \mu\text{m}$ will get cut off. Which is what happened when the SIFASTO (Tab. 2.1) recipe was used. The best slope achieved for a pin of $450 \mu\text{m}$ width with the SIFASTO recipe was 73° . The SIFASTO recipe needed to be modified so that the pins would survive the etch process.

The first modification to reduce the under etch was to increase the passivation and to increase the platen power (SRFASTO1, Tab. 2.1), this resulted in an average angle of 82.87° for the $450 \mu\text{m}$ wide pins. The slope was still too high so the next step was to have equal etch time and passivation time as in SRFASTO2 (Tab. 2.1), this resulted in black silicon appearing in the trenches. SRFASTO3 (Tab. 2.1) was inspired by a recipe from Berkeley University. In this recipe, both the etch time and passivation time were reduced, and with a less difference between them. For the $450 \mu\text{m}$ wide pins, the average slope was 83.66° , the $300 \mu\text{m}$ wide pins had an average angle of 82.87° and the

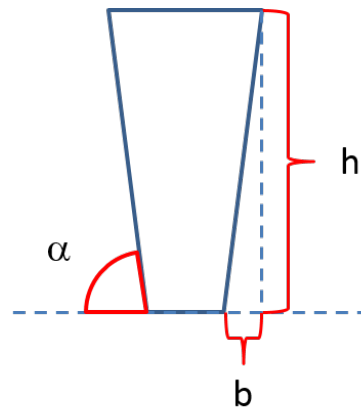


Figure 2.2: The pin structure with the height h , under etch b and the angle α marked.

150 μm wide pins had an average angle of 85.24° . The slope for the wider pins is not as good as for the small pins but because of their width it is acceptable. The angle of the 150 μm pin is better than 84.29° but then when etched all the way down to 750 μm , the base will only be 25 μm wide, which is still a fragile structure. SRFAST1 (Tab. 2.1) was also inspired by a recipe from Berkeley University. Only the etch time, passivation time and platen power had been modified in the previous recipes, here the pressure control valve position was changed from 55% to 68%, increasing the pressure and the platen power was increased to 20 W to have a more downward force of the ions. The average angle for the 450 μm wide pins was 85.24° , for the 300 μm wide pins, it was 85.24° and for the 150 μm wide pins it was 87.14° . The 150 μm wide pins slope gave a base width of 75 μm , which is a more stable structure.

The angles for the different pin width for each recipe is presented in Tab. 2.2.

Table 2.2: The average angle for each pin width (450 μm , 300 μm , 150 μm) for each STS ICP recipe is presented.

Pin width	450 μm	300 μm	150 μm
SIFASTO	73°	NA	NA
SRFASTO1	82.87°	NA	NA
SRFASTO2	83.66°	82.87°	85.24°
SRFAST1	85.24°	85.24°	87.14°

2.2.3 Centura II

The Centura II (DPS & MxP) has a three step process (deposition, breakthrough and etch) compared to the STS ICP that only has two steps. The purpose of the breakthrough step is to remove the passivation layer in the bottom of the trench first by increasing the platen power at this step. Three recipes, Centura 1/2/3 (Tab. 2.3) were created and tested. The Centura was used to etch the structures in section 4.4 and Paper VIII of the appended papers. Four levels with the depths of 364 μm , 283 μm , 283 μm and 70 μm , were etched in sequence with different etch masks. The Centura 1 recipe was used for the first two steps (364 μm + 283 μm ,) where the first step had an Al mask with its defining photoresist still present, and the second step had a thick photoresist etch mask. However, when etching the third step, a naked Al mask was present and therefore the risk of re-sputtering was bigger. Therefore, recipe Centura 2 was used, with a lower breakthrough power, shorter breakthrough time and a longer etch time, to reduce the re-sputtering. When etching the final step, that had an oxide mask, recipe Centura 3 was used. The platen power during breakthrough was increased back to 100 W since there was no metal to be re-sputtered anymore, and the etch time remained at 1.3 *sec* with the intention to remove any black silicon that might have manifested.

The Centura 1/2/3 recipes had an average etch rate of 14 $\mu\text{m}/\text{min}$, 14 $\mu\text{m}/\text{min}$ and 15 $\mu\text{m}/\text{min}$ respectively for this specific structure. Although the etch rate is much higher in the beginning, and the deeper the etch is, the rate is decreased, therefore it is also important to take into account at what depth the etch is performed at.

Table 2.3: The three etch recipes Centura 1/2/3 used with the Centura plasma etch machine. Each recipe consists of three steps, that are cycled, deposition (this parameter is the same for all three recipes), breakthrough and etch.

Parameters	Deposition	Breakthrough 1/2/3	Etch 1/2/3
Time (sec)	1.1	1.5 / 1.3 / 1.3	1.1 / 1.3 / 1.3
Pressure (mTorr)	55	90	90
Bias (Platen) Power (W)	5	100 / 50 / 100	60
Frequency (Hz)	125	125	125
Source power (W)	1900	1900	1900

The Centura recipes give a very low under etch as can be seen in Paper VIII. However, if there are any small particles such as passivation or re-sputtering of metal from the etch masks, these will create large spikes because of this vertical etch.

2.2.4 Comparison of the STS ICP machine and the Centura II

The most challenging etch structure is the high aspect ratio pin that appears in many of the designs presented in this thesis. Therefore, both machines were tested for the same Al mask with pins of the widths $200\ \mu\text{m}$ and $336\ \mu\text{m}$. The under etch b and the height h of the pins were measured, and the angle $\alpha = \arctan(h/b)$ was calculated, Fig. 2.2. The calculated average angle for the different widths and machines are presented in Tab. 2.4.

Table 2.4: Three different recipes (Centura 1, SIFAST0, SIFAST1) were used with the same mask. The angle was measured for pins with the width $200\ \mu\text{m}$ and $336\ \mu\text{m}$. The average angle for each recipe is presented.

Width	Centura 1	SIFAST0	SIFAST1
$200\ \mu\text{m}$	86°	83°	86°
$336\ \mu\text{m}$	86°	80°	84°

Although the optimized recipe SIFAST1 (Tab. 2.1) gave the best slope of the STS recipes, the Centura recipe gives slightly more vertical walls.

The average etch rate for the Centura machine is also very high ($\sim 14\ \mu\text{m}/\text{min}$) compared to the ICP machines best recipe SIFAST1 ($\sim 2.7\ \mu\text{m}/\text{min}$).

2.3 Sputtering

Sputtering is a thin film deposition method. The tool used in the presented work is the FHR MS 150, it that can handle substrates up to $150\ \text{mm}$ in diameter. It has five $200\ \text{mm}$ magnetron sputter cathodes used for different targets. A magnetron sputter has magnetron tubes attached to the target. With a power source, the target can have a negative voltage of around $-300\ \text{V}$. This attracts positive ions at a high speed towards the target. If the energy is high enough at impact, the bound atoms of the target will emit, hitting the substrate. Not all ions will have this effect. Some will be buried inside the target causing defects and some will create secondary electrons that will sustain the glow discharge. Magnets beneath the target help keep the secondary electrons close to the target. The electrons will spiral around the magnetic field. The plasma is easily ionized and the sputter rate is enhanced. This also allows for lower pressures inside the chamber.

The target is rotated above the substrate to enable uniformity of the deposited layer. The step coverage for sputters are better than evaporation techniques because of the different impact angles, although electroplating would be even more uniform. Both the target and the substrates are in a low pressure chamber with a pump connected to it for evacuation of gases. Of the five magnetron cathodes, three are used for DC sputtering

and the rest for RF. RF sputtering is good when using non conductive substrates to avoid charge build-up. The gases used are argon, nitrogen and oxygen.

The targets used in this work were Al, Ti and Au where the Ti is used to get better adhesion for the Au. The different deposition rates for the FHR MS 150 can be seen in Tab.2.5.

Table 2.5: Deposition rate for different materials

Material	Al $8 \cdot 10^{-3}$ mbar, 1 kW	Ti $5 \cdot 10^{-3}$ mbar, 1 kW	Au $5 \cdot 10^{-3}$ mbar, 0.2 kW
Deposition rate	2 nm/sec	1.1 nm/sec	1.2 nm/sec

2.4 Electroplating

Electroplating is a process to deposit a metal on a surface through electrolysis. A source of direct current is attached to two electrodes that are immersed in an ion solution. When there is an electrostatic potential between the anode and the cathode, positive metal ions are attracted to the cathode. If a conductive object is immersed in the solution and connected to the cathode, it will be covered in the metal. If the object is not conductive, a metal seed layer needs to be deposited on the object before electroplating. In this work, the metal is Au and is used to create a conductive surface on the devices presented in chapter 4.

A beaker with the positive Au ion solution (Enthronex Neutronex) is placed in a bath. The bath is heated and the solution is heated by the bath. Two electrodes connected to a voltage source are dipped in the solution. A platina net is attached to the anode and the object to be plated is attached to the cathode. The area of the platina net that is dipped in the solution is twice the surface area on the chip that will be plated. A current is chosen depending on how large the surface area that will be plated is. The surface roughness depends on the applied current, and how fast it is ramped up. A low surface roughness can be achieved with a slow ramping, or plating with a low current for a longer time. The thickness of the Au layer depends on how long time the chip is electroplated. To measure the thickness of the plated Au, a part of the surface is not covered with a Au seed layer, this is used as a reference after electroplating, to measure how much Au has been deposited. When the electroplated chip is removed from the solution, it is then washed in a deionized water bath with a lower temperature than the electroplating solution, and then rinsed again with room temperature deionized water.

2.5 Utilizing SOI Wafers

An SOI (Silicon On Insulator) wafer is a three part wafer where a handle wafer and a carrier wafer of silicon are bonded together with an insulator usually oxide between them. Sapphire can also be used, these wafers are called silicon on sapphire (SOS). SOIs can be used in microelectronics to reduce parasitic device capacitance by isolating the devices from the bulk. SOI wafers can also be used to create thinner devices by having all processes done first and then remove the handle wafer. The oxide layer can also be used as an etch-stop, i.e. during etching, the wafer they will not be etched anymore when they reach the oxide because oxide have a high selectivity to silicon. This can be used to achieve a uniform height all over the wafer when using DRIE.

2.6 SU8

SU8 is an epoxy-based negative photoresist developed by IBM, patented in 1989 [75]. It was first developed as a high resolution photoresist. SU8 can be made viscous and spin up to $650 \mu\text{m}$ in one step [76], an aspect ratio of more than 18 has been reported [77], and it is highly biocompatible [78], these qualities makes it suitable for applications such as a sacrificial layer for MEMS processing [79], microfluidics [80], high aspect ratio structures in MEMS [81], and also recently RF-MEMS [82].

Unexposed SU8 consists of a polymeric epoxy and a solvent. When exposed to UV-light within the range ($350 - 400 \text{ nm}$) a photoacid is produced. When the SU8 is then heated during post exposure bake (PEB), the photoacid works as a catalyst to allow the polymers to crosslink between them. The PEB temperature needs to be higher than the glass transition temperature T_g for crosslinking to happen. The parts that are not exposed to UV-light will not crosslink and during development will dissolve.

An issue that can occur is that during spinning the SU8 is not distributed properly, there are many suggestions how to avoid this at <http://memscyclopedia.org/su8.html> which is a MEMS forum. Four ways to distribute the SU8 better were examined.

Fig. 2.3a, the most common way is to simply apply a click of SU8 with a syringe on the wafer and then spin. This resulted in the whole wafer not being fully covered and bubbles were visible throughout the surface. Small bubbles came from the syringe, when applying the SU8 on the wafer, which were increased during spinning.

Fig. 2.3b, the wafer with SU8 was first heated to decrease the viscosity and allow the bubbles to be released before spinning. The SU8 was heated up to 35° and cooled repeatedly until no more bubbles were visible. The wafer was completely covered but there were still some bubbles observed.

Fig. 2.3c, an attempt to smear a thin layer of SU8 on the wafer with a squeegee technique and then add the desired amount on top of it to enable the distribution of the SU8. The squeegee technique is when a spatula is used to cover the wafer with SU8.

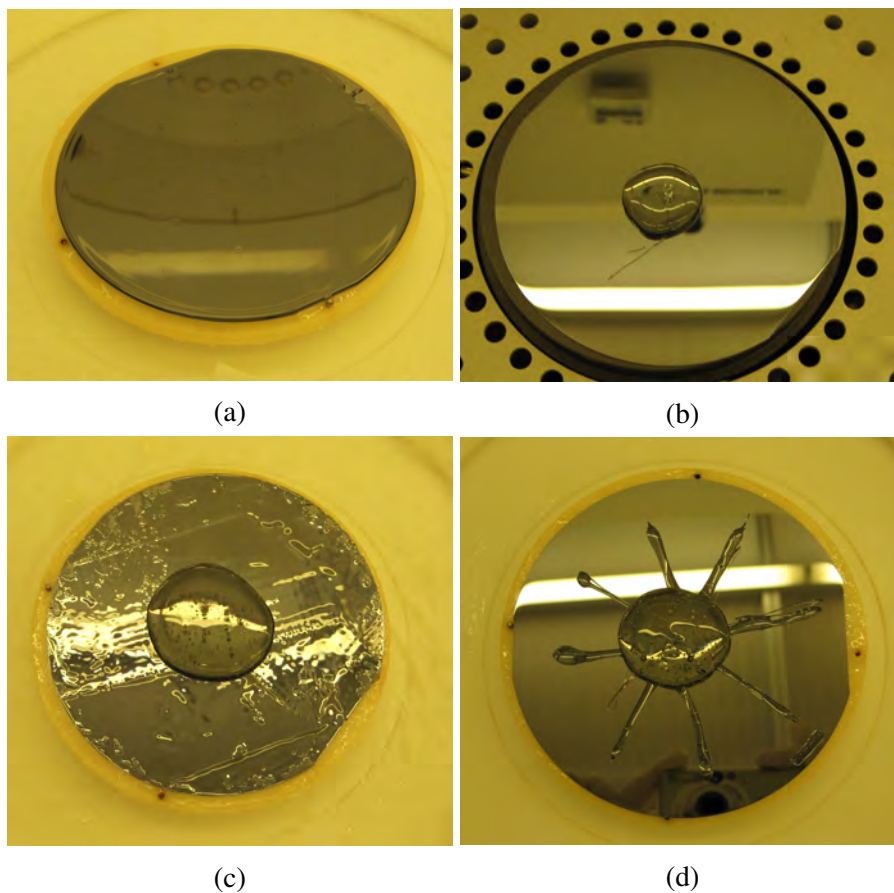


Figure 2.3: (Four different distribution ways of SU8. a) a small amount of SU8 was poured on the wafer and then spun. b) preheating the wafer three times for one minute at 35° with the SU8 on to enable the distribution during spinning. c) SU8 distributed by squeegee technique. d) SU8 distribution by star pattern

This method is messy and there were still a large amount of bubbles after spinning.

Fig. 2.3d, a star pattern was made with the intention to guide the SU8 all the way to the edges, to enable the distribution. This resulted in the wafer not being completely covered after spinning and containing many bubbles in the surface.

It was concluded that a combination of the explored techniques can be used avoid bubbles and enable the distribution. The SU8 was poured instead of using a syringe which reduced the amount of initial bubbles. There was a distribution spin before at a 500 rpm and then the SU8 was spun at a higher speed to get the desired thickness. Relaxation times were implemented between the steps to give time for the bubbles to surface.

2.7 Carbon Nanotubes

In 1991 Sumio Iijima discovered the first synthesized carbon nanotubes [83], and in 1992, three papers presented theoretical studies of the properties of carbon nanotubes [84–86].

Carbon nanotubes can be described as sheets of graphene rolled up into tubes. There are three types of tubes, zig-zag, armchair and chiral, the names indicating in which direction the atoms are connected. In Fig. 2.4 the lattice vectors of a graphene sheet is shown. The different lattice vectors determine the carbon nanotubes chirality. If $n=0$, the chirality of the carbon nanotube is zig-zag, and if $m=n$ then the chirality is armchair. If the chirality indices (n,m) satisfy the condition $n-m=3i$, where i is an integer, the carbon nanotube has metallic properties. In Fig. 2.4, the circled dots mark vectors with metallic behaviour, while the dots marks the vectors with semiconducting behaviours. If we assume that the distribution of lattice vectors are uniform, then one third of the carbon nanotubes are metallic and two-third are semiconducting [86].

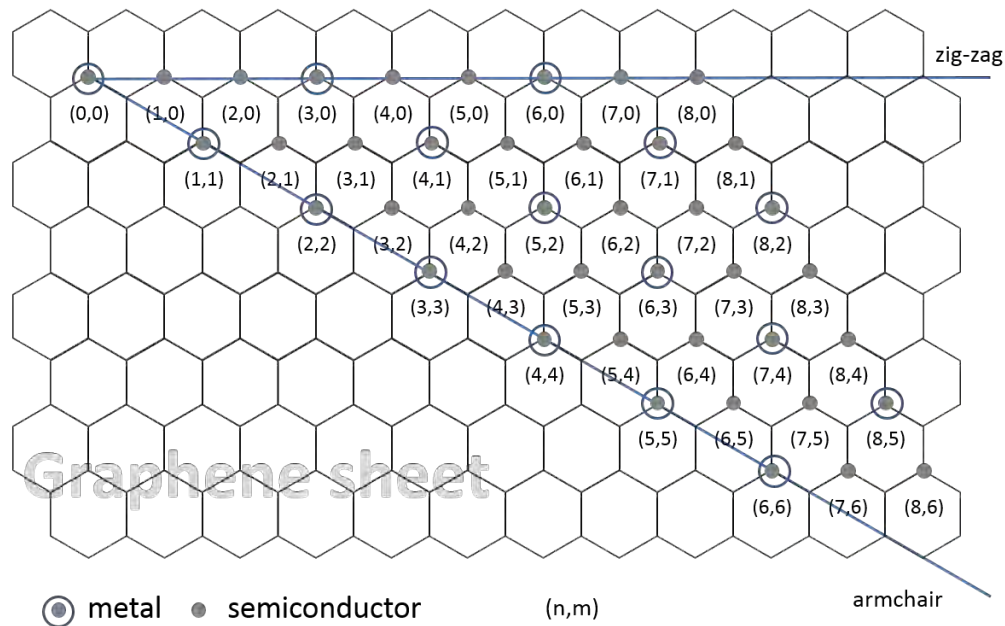


Figure 2.4: Lattice vectors, of a graphene sheet.

The three most common ways to synthesize carbon nanotubes are: Arc-Discharge (this method was used to synthesize the carbon nanotubes Iijima discovered), Laser ablation and Chemical Vapor Deposition (CVD). The carbon nanotubes presented in this thesis have been synthesized with thermal CVD, and therefore, only this method will be discussed.

Carbon nanotubes synthesized with thermal CVD do not have the same quality as the above mentioned methods [87], however, the benefit is that the substrate can be patterned: the catalyst is patterned on the wafer and the carbon nanotubes will grow according to the pattern.

The wafer is patterned with a catalyst such as nickel, cobalt, iron, Au or platinum. In this thesis aluminum and iron was used. The wafer with the catalyst pattern is then placed in the CVD chamber where it is pretreated with a hydrogen gas at $500^{\circ} C$. The hydrogen gas activates the catalyst and then the temperature in the chamber is risen ($500 - 1000^{\circ} C$) so that the catalyst will separate into nano islands. The hydrocarbon gas, in this case acetylene, is pumped into the chamber. The gas reacts with the catalyst and starts to build tubes on each nano island. The tubes can grow either with the catalyst particle staying at the bottom of the tube or with the particle at the top with the tube manifesting underneath it, so called base respectively tip growth.

Gap Waveguide Theory

Gap waveguides enables the transmission of high frequency waves without the need for conductive solid walls connected to each other. The theory behind gap waveguide technology, two types of gap waveguides, the ridge and the groove, and how the resonator is used to determine losses are described in this chapter.

3.1 Hard and Soft Surfaces

The terms hard and soft surfaces come from acoustic theory referring to surfaces that stop respectively allow propagation of waves at the surface. In electromagnetic field theory, they are a form of metamaterial. In acoustic theory a soft surface damps the acoustic wave, and a hard surface allows propagation of the acoustic wave. Hard and soft surfaces for electromagnetic waves were presented in [88] and [89]. A metamaterial is a material that can achieve certain physical characteristics by changing the texture of the material. Gap waveguides are based on the kind of metamaterial that acts as a magnetic conductor, i.e. an artificial magnetic conductive (AMC) surface, which does not exist in nature. The boundary conditions for smooth conductors, soft surfaces and hard surfaces are defined in Tab.3.1.

Soft surfaces can be realized with transverse corrugated surfaces with a depth $d = \lambda/4$, Fig. 3.1a. Every groove acts as an open circuit, that is the corrugation transforms from a short circuit to an open circuit giving the surface infinite impedance in the direction that is perpendicular to the corrugations. If a wave is traveling in this direction E_{VER} "sees" an AMC and is equal to zero due to the transformation from short to open circuit. E_{HOR} "sees" a perfect electric conductor and is also equal to zero.

Table 3.1: Boundary condition of smooth conductors, soft surfaces and hard surface.

Type of surface	Boundary condition	Wave propagation at surface
Smooth conductor	$E_{HOR} = 0$ $\partial E_{VER} / \partial n = 0$	STOP for HOR pol. GO for VER pol.
Soft surface	$E_{HOR} = 0$ $E_{VER} = 0$	STOP for HOR pol. STOP for VER pol.
Hard surface	$\partial E_{HOR} / \partial n = 0$ $\partial E_{VER} / \partial n = 0$	GO for HOR pol. GO for VER pol.

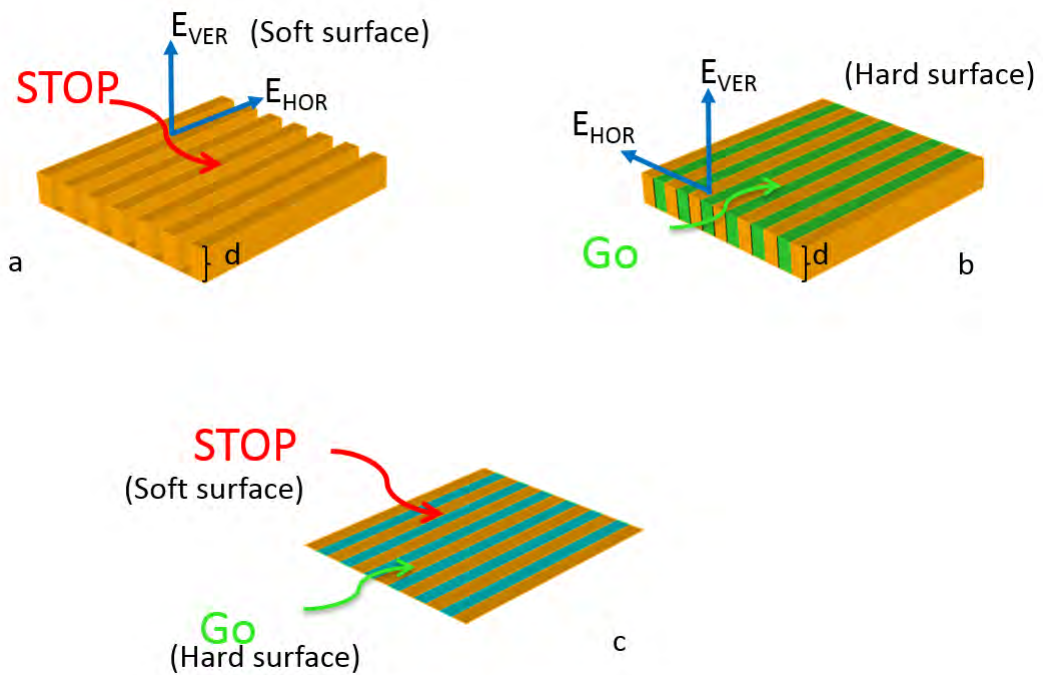


Figure 3.1: a) soft surface realized with transverse corrugations, b) hard surface realized with longitudinal corrugations filled with dielectric and c) soft hard surface ideally realized with PEC/PMC (gold/blue) strips

If the grooves are filled with a dielectric, a hard surface can be achieved in the longitudinal direction, Fig. 3.1b. The depth d is determined by

$$d = \frac{\lambda}{4\sqrt{\epsilon_r - 1}} \quad (3.1)$$

where ϵ_r is the permittivity of the dielectric. Here E_{VER} sees a perfect electric conductive surface and E_{HOR} meets an AMC surface, iterative transformations from short to open circuits due to the grooves as for the soft surfaces for TEM waves.

Hard and soft surfaces are realized ideally by PEC (perfect electric conductive) and PMC (perfect magnetic conductive) strips as in Fig. 3.1c. This surface is soft when the strips are transverse and hard when the strips are longitudinal.

3.2 Bed of Nails

The "Fakir's Bed of Nails" [90] is a metamaterial used to realize an AMC surface. In this case, metallic pins are arranged periodically on a conducting ground plane, Fig. 3.2. The pins create an array of open circuits for a certain frequency range, which in turn makes the tangential magnetic field zero at its surface and the tangential electric field has nonzero value. This surface is therefore the equivalent of an AMC surface. It is artificial because that its electromagnetic characteristics for the desired frequency range comes from the materials macro structure. The pins are periodically placed in all directions to assure that the tangential magnetic field is zero at all azimuth directions at a grazing incidence.

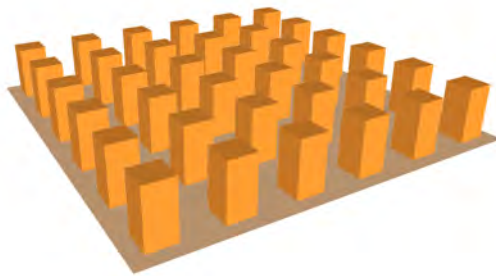


Figure 3.2: Periodically placed electrical conductive pins also called "bed of nails".

An electrically conducting surface has the opposite characteristic, here, the tangential electric field is zero and the tangential magnetic field has a nonzero value. When the two surfaces are placed opposite each other at a short distance (Fig. 3.3), less than

$\lambda/4$, a stop band is created due to the contradicting boundary conditions and no waves can propagate in the gap between the two surfaces [91]. A stop band can also be seen as a magnetic wall in a rectangular waveguide, where two opposing walls are electric conductors and the other two opposing walls are magnetic conductors.

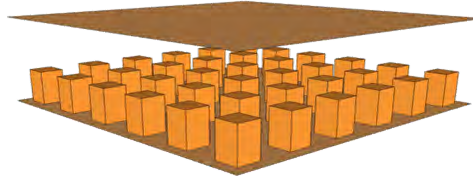


Figure 3.3: An electrically conductive surface placed parallel above the magnetically conductive "bed of nails" surface with $\lambda/4$ space apart.

Another way of looking at it is to think of three simple rules for electromagnetic waves (Fig. 3.4a): 1) Electromagnetic waves do not pass through electric conductors, but rather, they are reflected. 2) Any electric field that touches an electric conductor must be perpendicular to it. 3) Any magnetic field close to an electric conductor must be parallel to it. For magnetic conductors, the opposite applies (Fig. 3.4b).

When these two surfaces are brought together and are close enough ($\lambda/4$) the wave cannot exist due to the boundary conditions, Fig. 3.5.

There are many parameters affecting the stop band that the bed of nails create together with an upper electrically conductive lid. In [91], a numerical study was done on the squared pin surface of the bed of nails. For the bed of nails, five factors affect the stop band: the gap h , the height of the pins d , the period of the pins p , the radius r (for square pins, r is half the width) and the lattice geometry. The strongest condition for the gap is that it needs to be smaller than $\lambda/4$ to create a stop band. The study shows that the stop band size increases when the gap decreases. The pin height d needs to be at least $\lambda/4$, when d reaches $\lambda/2$, the upper limit is reached. In [91], the square geometry and the triangular geometry were studied. It was shown that for both geometries the results are quite similar for different gaps h . In [91] the periodicity of the pins was studied, and how they can affect the placement of the stop band. Different patterns and shapes of the pins were evaluated also in [91]. For simplicity and its isotropic properties, only the "bed of nails" structure with rectangular pillars was implemented.

There are other kinds of pins that can be used to realize an AMC, such as the mushroom shape, the inverted pyramid pin, and even a spring shaped pin [92–94].

The so-called mushroom shape (Fig. 3.6 and 3.7) are conventionally made out of conductive vias and patches on a dielectric substrate. For a specific frequency range,

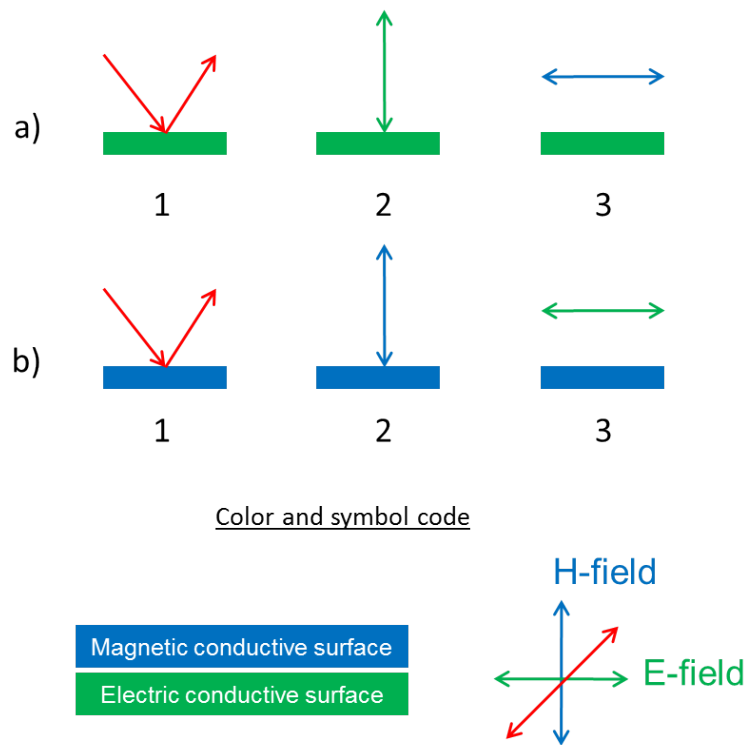


Figure 3.4: A schematic view of the rules for electrical conductors and electromagnetic waves, at the top. And the implementation of these rules for magnetic conductors, at the bottom.

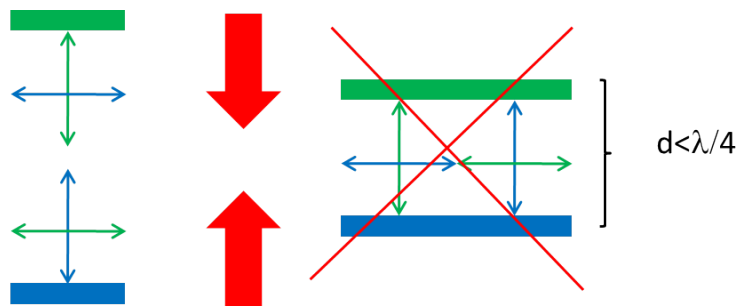


Figure 3.5: When an electrically conductive surface is opposite a magneticly conductive surface and the distance is $< \lambda/4$, a stop band occurs due to the boundary conditions.

the array of mushrooms acts as a two-dimensional electric filter [92]. An AMC surface based on mushroom shaped pins was studied in [91]. The parameters that can have

impact on the stop band are the via radius r , the height of the mushroom d , and where the via is placed relative to the center of the patch. It was concluded in [91] that the start frequency of the stop band was shifted to higher frequencies when the radius r is increased. The opposite occurs when the height of the mushroom is increased, that is that the start stop band is shifted to lower frequencies. The benefits of the mushroom pins are that they are more compact than the previous mentioned pins, and that they can offer a wider stop band.

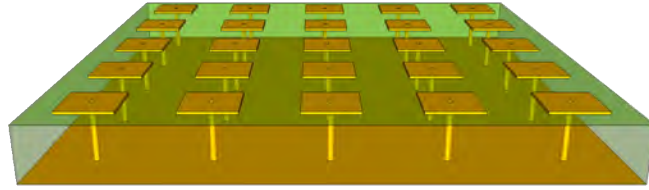


Figure 3.6: A "mushroom" surface area creating a magnetically conductive surface.

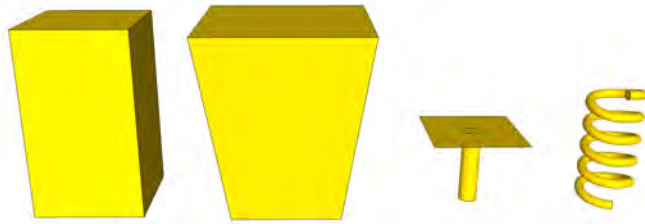


Figure 3.7: Figures of the different types of pins explored. From the left: The squared pin, the inverted pyramid, the mushroom and the spring.

The inverted pyramid pin (Fig. 3.7) was studied in [93], and compared to an equally high square-shaped pin with the same gap to the above placed electrically conductive lid. The bandwidth increased from 43% with the square-shaped pin to 66% with the inverted pyramid shaped pin [93].

The spring-shaped pin (Fig. 3.7) was studied in [94], the total length of the pin is the same as a squared pin for the same frequencies, however due to its shape, the effective

length can be much shorter, thus offering a more compact setup. The spring surface showed equal performance to the squared shaped pin, although the spring pin was much shorter and can offer a more compact AMC surface, [94].

3.3 Ridge Gap Waveguides

Ridge gap technology utilizes the magnetically conducting properties of the bed of nails surface and the stop band that it creates together with an electric conductive surface. If one places an electrically conductive ridge in between the AMC structures then one has a surface where the wave is allowed to propagate (Fig. 3.8), because there now are two electrical conductive surfaces opposing each other, where the wave can propagate in between. The wave is then confined by the stop band generated by the AMC around the electrically conductive ridge. This eliminates the need for electrically conducting sidewalls. The ridge gap waveguide supports only quasi-TEM modes.

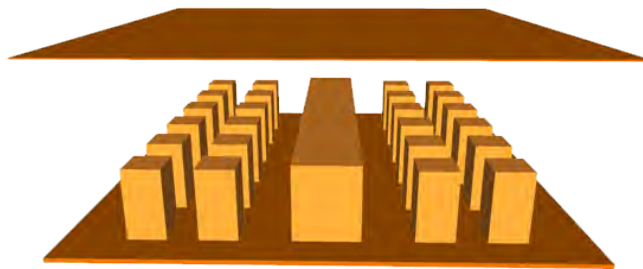


Figure 3.8: A ridge gap waveguide consist of an electrically conductive ridge embedded in the AMC surface with a parallel electrically conductive plate above it.

3.4 Groove Gap Waveguides

The groove gap waveguide utilizes the bed of nails surface in the same way as the ridge gap waveguide does. The difference is that instead of having a ridge guiding the wave between it and the top electric conductive plate, there is now a groove guiding the wave in its interior, Fig. 3.9. The allowed modes propagating are similar to a rectangular waveguide. Therefore, the opening of the groove for vertical polarization has the same width as a rectangular waveguide and the distance from the groove to the top plate is the same as the height of a rectangular waveguide for the same frequency range. The groove gap waveguide supports TE/TM modes and can be compared to a rectangular waveguide. The width of the groove and the distance between the bottom plate and the

top plate are often designed to have the same dimensions as a rectangular waveguide for the same frequencies, allowing it to be connected to a rectangular waveguide.

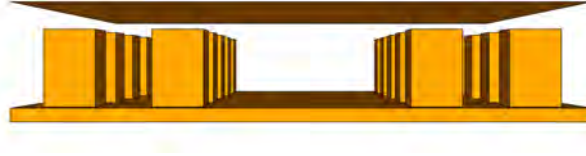


Figure 3.9: A groove gap waveguide where the wave propagate within the groove instead of along a ridge.

3.5 Resonators, Q-factors and Losses

The gap waveguide resonators can be compared to a microwave cavity. Microwave cavities can be hollow or filled with a dielectric and are made from short-circuited waveguides. The only losses that exist are from the cavity walls and the dielectric. Gap waveguides have no dielectric and therefore there are only conductive losses on the surface. Which frequencies that are resonant depends on how the electromagnetic field modes satisfy the boundary conditions of the cavity walls. The cavity length needs to be $n\lambda/2$ to satisfy the boundary condition for resonance at a certain frequency [1].

With resonators, the quality factor (Q) can be extracted, which in turn can be used to determine losses. To use Q-factors to determine losses in transmission lines, is well-known in the field of microwave theory [1].

The Q-factor is the ratio between the energy stored in the resonator and the power loss. The approximate Q-factor which is extracted from measurement is called the loaded Q (Q_L). Q_L is defined as the ratio between the center frequency of the resonant cavity and its 3-dB bandwidth, equation 3.2 from [1].

$$Q_L = \frac{f_0}{\Delta f_{3dB}} \quad (3.2)$$

Q_L can be divided into two parts. The unloaded Q (Q_U) which is the Q-factor for an ideal resonator and corresponds only to the losses of the resonator. The other part is the external Q (Q_E) which is due to the loss of all external connections such as the feeding network [95].

$$\frac{1}{Q_L} = \frac{1}{Q_U} + \frac{1}{Q_E} \quad (3.3)$$

where Q_E is determined from S_{21} as, [96]:

$$Q_E = 10^{-S_{21}(dB)/20} \cdot Q_L \quad (3.4)$$

We can then express Q_U as:

$$Q_U = \frac{Q_L}{1 - 10^{-S_{21}(dB)/20}} \quad (3.5)$$

For transverse electromagnetic (TEM) modes transmission line resonators, the attenuation α can be expressed using the unloaded Q and the propagation constant β .

$$\alpha = \frac{\beta}{2Q_U} \quad (3.6)$$

To obtain the most accurate value for the unloaded Q, it is best to measure a weakly coupled resonator (low S_{21}), in which case the external Q (Q_E) contributes very little. If the resonator is strongly coupled, that is if S_{21} is high, an uncertainty calculation can be done with equation 3.7, [97]. Where $\Delta Q_U/Q_U$ is the relative uncertainty of the unloaded Q, $\Delta BW/BW$ is the bandwidth uncertainty, and ΔS_{21} is the insertion-loss uncertainty. In [97], ΔBW is calculated to be $\Delta BW = 0.23BW\Delta S_{21}$.

$$\frac{\Delta Q_U}{Q_U} = \sqrt{\left(\frac{\Delta BW}{BW}\right)^2 + \left|\frac{\ln 10}{20} \cdot \frac{10^{-S_{21}(dB)/20}}{1 - 10^{-S_{21}(dB)/20}}\right|^2 (\Delta S_{21})^2} \quad (3.7)$$

The attenuation for the ridge gap resonator can be expressed by equation 3.6, however, the groove gap resonator cannot be considered as a TEM line [95] and equation 3.6 cannot be used in this case.

Devices

4.1 280 GHz Ridge Gap Waveguide and Resonator

In Paper I, two ridge gap waveguide devices are presented, a ridge gap 90° bend waveguide and a ridge gap resonator, both fabricated with gold-covered Si. The resonator as described in chapter 3 can be used to determine losses, and is therefore well suited to test different materials as base material for high frequency components. In Papers V and VI, SU8 and carbon nanotubes are explored separately as base materials for low-cost and rapid prototyping. This is done by fabricating a 280 GHz resonator with these materials, covering them with gold, and measuring the Q -values to determine how lossy the system is compared to the simulations.

4.1.1 Si ridge gap resonator and waveguide

The first micromachined gap waveguide devices are presented in Paper I, and had an operation frequency range of 210 – 340 GHz. The two devices were a ridge gap 90° bend waveguide and a ridge gap resonator, Fig. 4.1.

The two devices are based on gap waveguide technology and utilize the "bed of nails" metamaterial surface to confine the wave as described in chapter 3. The pins and the ridge have a designed height of 277 μm , and the squared pins all have a width of 167 μm . In Fig. 4.2, a schematic view of both the resonator and the waveguide with dimensions are presented. The chip has a large area outside the active pin area (Fig. 4.1). This is deliberate so that when electroplating the chips, there is enough surface to connect the electrode as mentioned in section 2.4, and easier handling and mounting of the chips.

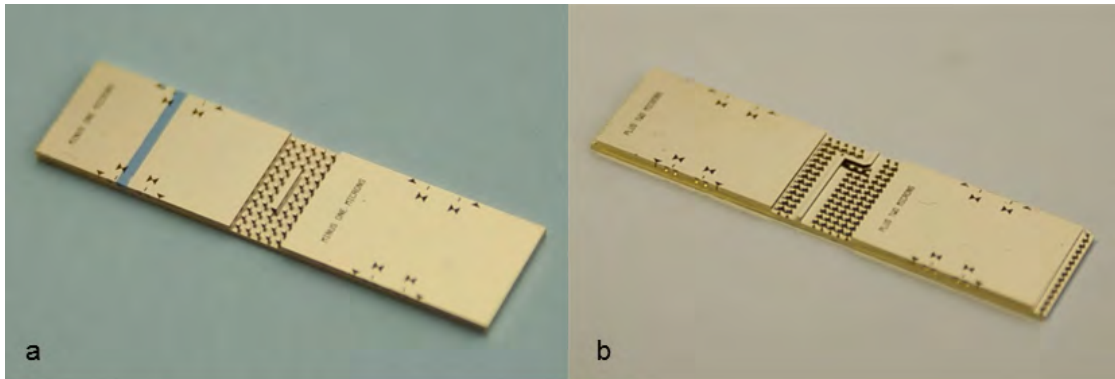


Figure 4.1: a) A ridge gap resonator micromachined for 210-325 GHz. b) A micromachined ridge gap waveguide with two 90° bends micromachined for 210-325 GHz.

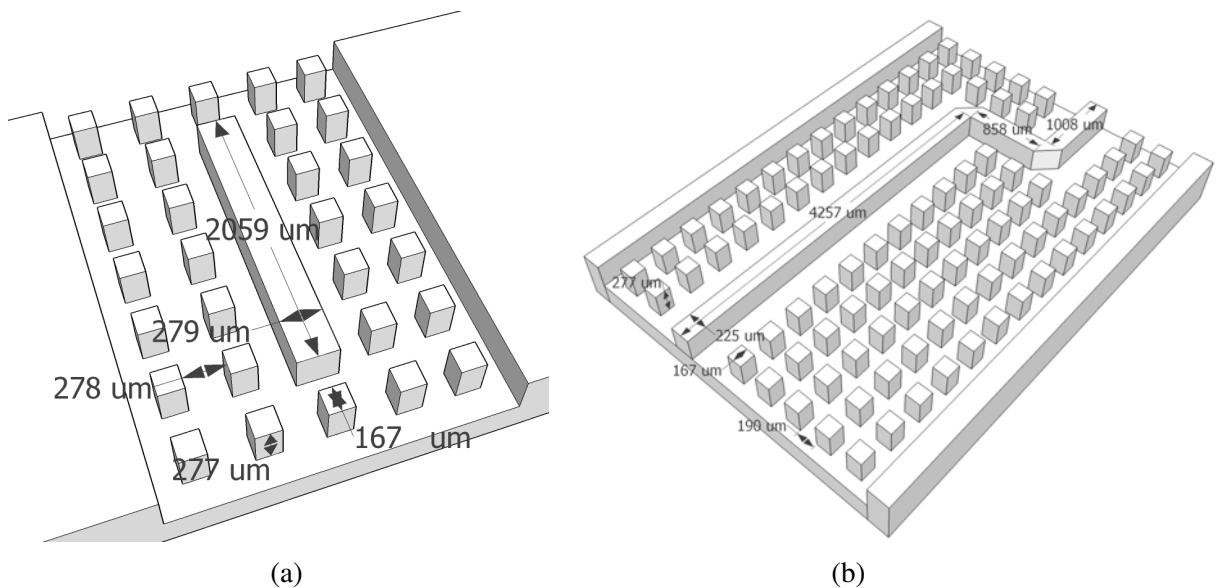


Figure 4.2: (a) The ridge gap resonator. (b) The ridge gap waveguide.

The gap needed above the ridge gap waveguide was $55 \mu m$ and above the resonator $167 \mu m$. The gap was realized with the help of a gold-plated brass support structure mentioned in Paper I, for the ridge gap waveguide, the support structure had a third purpose of also having a transition structure from rectangular waveguide to ridge gap waveguide milled into it. Fig. 4.3 shows the schematics of the resonators support structure (Fig. 4.3a), the ridge gap waveguide with the bottom part of the support structure (Fig. 4.3b), and a close up of the rectangular waveguide to ridge gap waveguide transition (Fig. 4.3c).

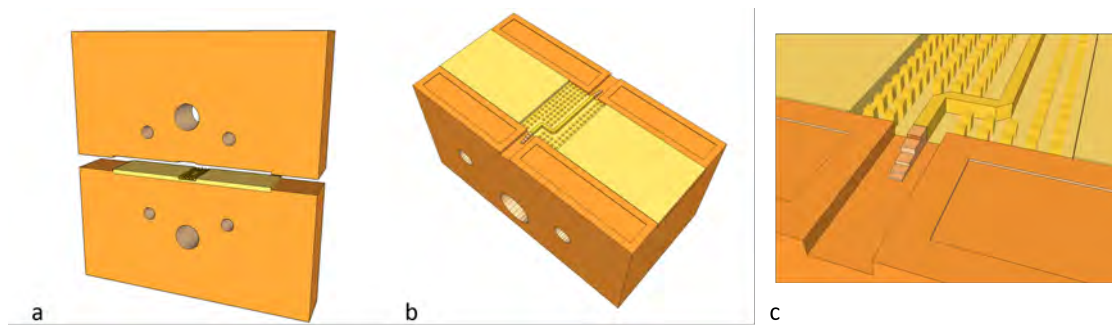


Figure 4.3: a) The ridge gap resonator with the top and bottom part of the measurement package. b) The ridge gap waveguide in the bottom part of its package. c) A close up of the rectangular waveguide to ridge gap waveguide transition.

In Fig. 4.4 the schematic process plan for both the ridge gap waveguide and the resonator can be seen. A $0.5 \mu\text{m}$ Al layer was sputtered on a 6" Si wafer (Fig. 4.4a). A photolithography pattern with the photoresist was made on top of the Al and then the Al was patterned through wet etching (Fig. 4.4b). DRIE etching was used to define the structures, down to a depth of $277 \mu\text{m} \pm 10 \mu\text{m}$ (Fig. 4.4c). The wafer was later diced and the device was then sputtered with a seed layer of Ti/Au (50/200 nm) and then electroplated with Au to a thickness of $1 \mu\text{m}$ to avoid skin-effect at these frequencies (Fig. 4.4d).

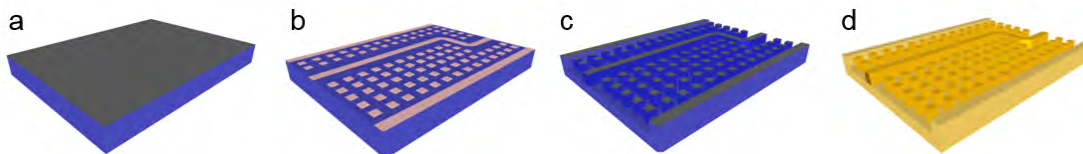


Figure 4.4: Process plan for both the waveguide and the resonator. (a) A layer of Al is sputtered on a Si wafer. (b) The Al is patterned. (c) DRIE is used to etch the pillars. (d) The ridge gap waveguide and resonator are covered in Au.

The connection between the ridge and the transition structure shown in Paper I and Fig. 4.3c was very sensitive, and it needed less than $1 \mu\text{m}$ gap between the ridge and the transition structure. When measuring on the 90° bend waveguide, the reflection was too large. Soldering was thereafter used with the intention to close the gap between the ridge and the transition (See Fig. 4.5). However, no transmission could be detected in the 90° bend ridge gap waveguide.

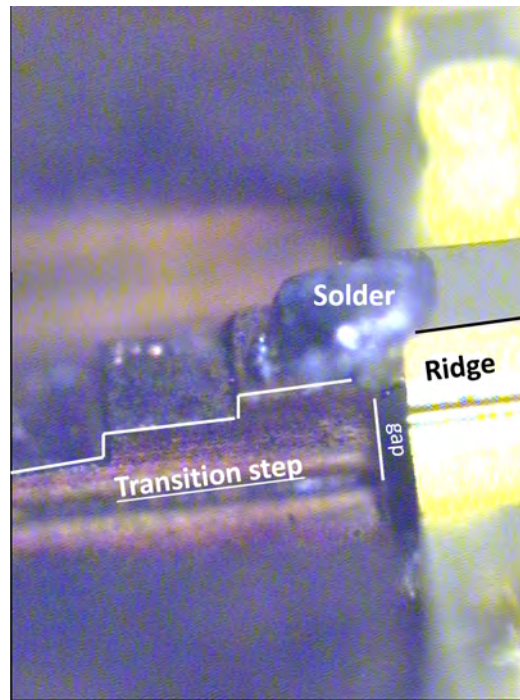


Figure 4.5: A microscope image of the transition seen in Fig. 4.3c with soldering covering the gap between the transition step (highlighted) and the ridge gap waveguide.

The resonator, on the other hand, only needs weak coupling so a transition structure was not necessary. The initial measurement showed quite a lossy connection and difficulties to detect the resonances, Fig 4.6. This can be explained by looking at the simulation of the resonator. The two resonance peaks are present below -60 dB, Fig. 4.7. The resonator is designed to have peaks at low dB levels to be able to exclude external losses (see section 3.5). However, the noise floor of the measurement equipment used at the time (Agilent's 4-port PNA N5222AS Network Analyzer, connected to Oleson Microwave Labs extenders) was around -40 dB. To increase the resonance peaks dB-level, two pin rows were removed from each of the connecting sides of the resonator. Every pin row supplies a damping of around -20 dB and the three pin rows as seen in Fig. 4.1a for the case of the resonator gave resonance peaks below -60 dB as shown in the simulation (Fig. 4.7), therefore, by removing one row of pins, the peaks will rise around 20 dB. In Fig. 4.7 the simulations for the resonator with three pin rows and one pin row on each side of the ridge, and the measurements for the resonator with one pin row on each side of the ridge are presented.

By using equation 3.6 in chapter 3, the attenuation can be calculated with the unloaded Q-factor obtained from the extracted loaded Q-factor. Table 4.1 shows the sim-

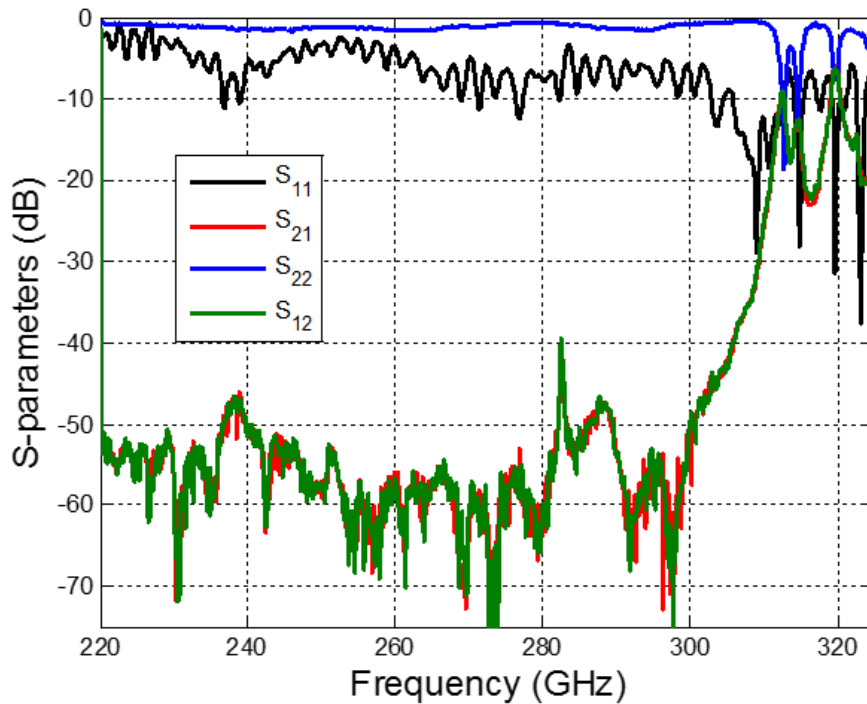


Figure 4.6: The initial measurements of the three pin row ridge gap resonator.

ulated and measured unloaded Q-values for the resonator with three pin rows and the resonator with one pin row. The simulations are performed for a solid Au structure. The attenuation values extracted from these Q-values are also presented.

Table 4.1: Simulated and measured Q-values together with the corresponding losses extracted from them.

	Three pin rows resonator			One pin row resonator			
	Simulated		Measured	Simulated		Measured	
Frequency (GHz)	230	280	282	234	284	234	284
Unloaded Q	1030	1171	$73 \pm 6.9\%$	859	992	$642 \pm 9.2\%$	$597 \pm 7.1\%$
Loss (dB/mm)	0.020	0.022	0.035	0.025	0.026	0.033	0.043

The benefit of having three pin rows on each side of the ridge is to have a weakly coupled resonator. This in turn gives a more accurate calculated unloaded Q value (see section 3.5). When there is only one pin row at each side of the ridge, the resonator is strongly coupled. This gives a higher uncertainty than for a weakly coupled resonator.

The uncertainty of the unloaded Q values can be calculated with equation 3.7. The

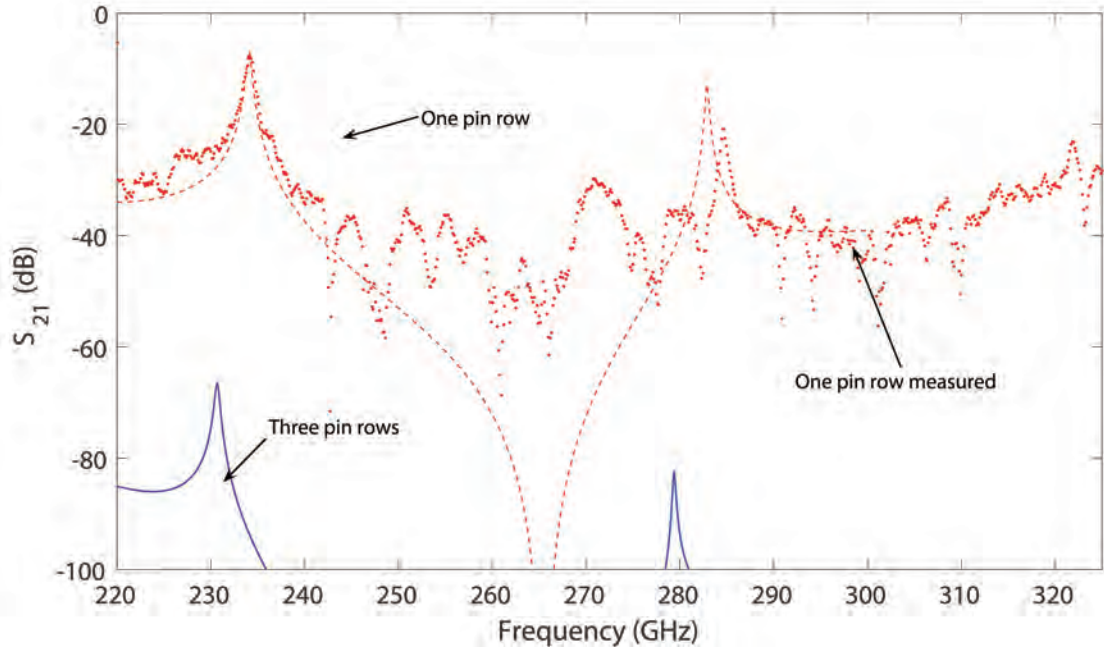


Figure 4.7: Simulated S_{21} of the ridge gap resonator with three pin rows on each side (blue solid line), simulated S_{21} of the ridge gap resonator with one pin row on each side (red solid line), and measured S_{21} of the ridge gap resonator with one pin row on each side (red dotted line).

insertion loss uncertainty ΔS_{21} is affected by many factors, such as temperature, noise, and drift of the system. Therefore, to estimate the insertion loss uncertainty, a measured magnitude stability value of ± 0.3 dB on a similar system with WR3.4 extender from *Virginia diodes* is used. The magnitude stability was measured after 1 hour of system warm-up. The uncertainty of the unloaded Q values are calculated with $\Delta BW = 0.23BW\Delta S_{21}$ (section 3.5) and $\Delta S_{21} = \pm 0.3$ dB, and are presented in Tab. 4.1.

The losses calculated from the ridge gap resonator with one pin row on each side of the ridge are compared to existing technologies in Tab. 4.2.

Table 4.2: The calculated losses of the ridge gap resonator are compared to reported losses for rectangular waveguides and microstrip lines operating at 220 – 325 GHz.

Transmission line	Loss (dB/mm)
Rectangular Waveguide [82]	0.017-0.025 dB/mm
Microstripline [98]	0.6-0.9 dB/mm
Ridge gap waveguide	0.033-0.043 dB/mm

4.1.2 SU8 ridge gap resonator

All the micromachined gap waveguides in the section above were fabricated in silicon. Silicon's advantage is that there are many standardized processes available to manipulate silicon with, down to nanometer resolution. Silicon is a strong material if exposed to even forces. However, if subjected to uneven forces, it is as brittle as glass. Therefore it is of interest to explore alternative materials which are more robust and that can be microfabricated. Standard CNC-milled WR03 waveguides and metallized SU8 based rectangular waveguides were measured and compared in [82]. SU8-based rectangular waveguides were also shown to have a comparable loss to the CNC milled rectangular waveguides ($\sim 0.02 \text{ dB/mm}$ for $220 - 325 \text{ GHz}$). This shows that SU8 has a huge potential for microwave technology based prototypes. SU8 is a relatively low cost material with an uncomplicated process, it can easily be mass produced and it can achieve high aspect ratio structures.

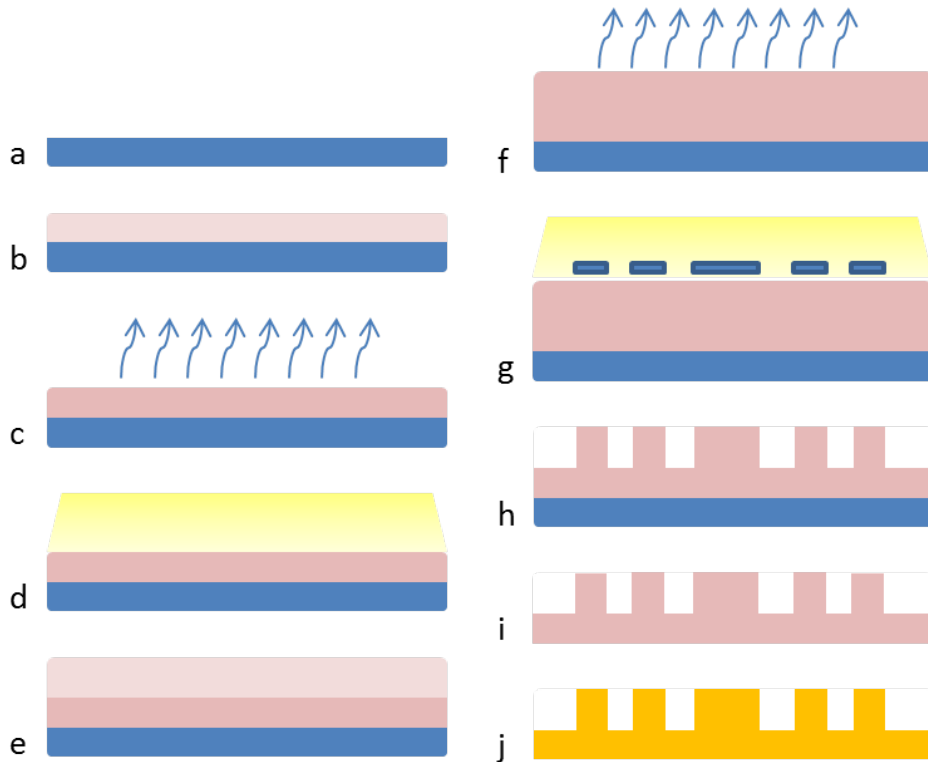


Figure 4.8: a) Si wafer, b) first layer of SU8 dispensed, c) soft bake, d) flood exposure, e) second layer of SU8, f) second soft bake, g) patterning, h) developing the SU8, i) KOH etch of the Si, j) sputtering and electroplating of Au.

In the process presented in Paper V, SU8 2150 was dispensed on a silicon carrier wafer (Fig. 4.8a). The SU8 was spun to achieve a desired thickness of $245\ \mu\text{m}$. This layer will act as the carrier layer (Fig. 4.8b). The wafer was soft baked to evaporate the solvent in the SU8 before exposure, Fig. 4.8c. The whole wafer was then flood exposed, Fig. 4.8d.

A second layer of the same SU8 was dispensed, and then spun to achieve a height of $275\ \mu\text{m}$, Fig. 4.8e. A second soft bake was done, Fig. 4.8f. The second SU8 layer was patterned with a negative photomask (Fig. 4.8g), followed by a post-exposure to increase the cross-linking in the exposed areas.

The whole wafer was developed. Due to the large aspect ratios, strong agitation was needed, Fig. 4.8h. The silicon wafer was removed through immersion in KOH, left was a wafer completely made out of SU8 (Fig. 4.9 and Fig. 4.8i). The SU8 wafer was diced, sputtered with a Ti/Au seed layer and electroplated with Au, Fig. 4.8j. The pin height over the entire wafer was not uniform and could vary $\pm 20\ \mu\text{m}$ over a 4" wafer.

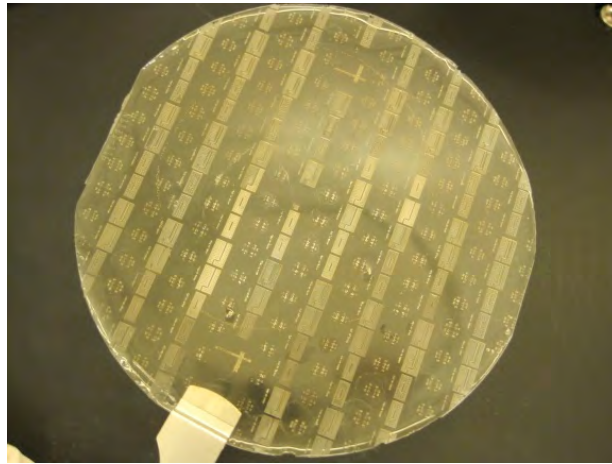


Figure 4.9: A complete SU8 "wafer"

Fig. 4.10 shows SEM images of a pin from the silicon ridge gap resonator and a pin from the SU8 ridge gap resonator. As seen in Fig. 4.10, the SU8 pin has straight side walls and no under etch compared to the silicon pin, and the slope of the pin as mentioned in section 2.2.2 for Si devices is not an issue.

The measurement was divided into two frequency ranges, to have more measurement points in each range and therefore get a more accurate resonance peak. Fig. 4.11a shows simulations together with measurements for the SU8 based resonator, between $220 - 260\ \text{GHz}$. Fig. 4.11b shows for the same devices but for the range between $270 - 310\ \text{GHz}$.

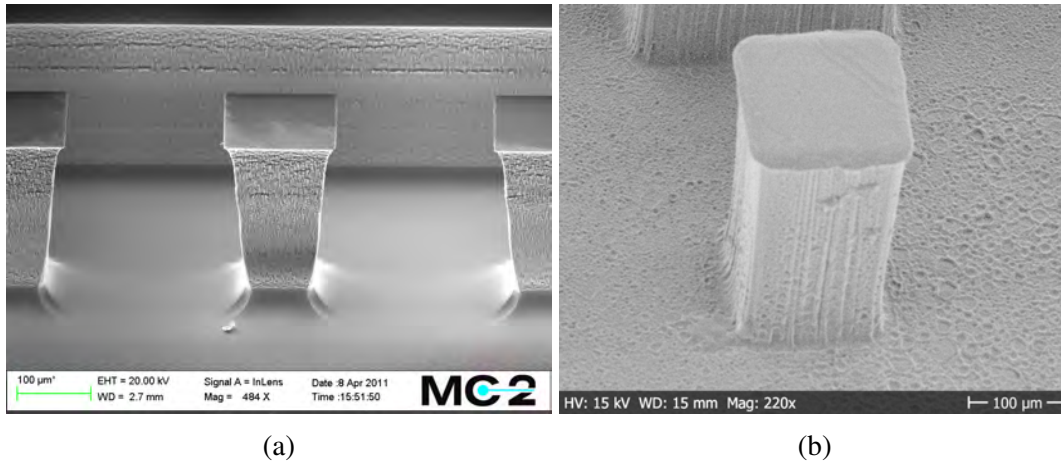


Figure 4.10: (a) SEM image of the Si pins (b) SEM image of a SU8 pin on the SU8 carrier.

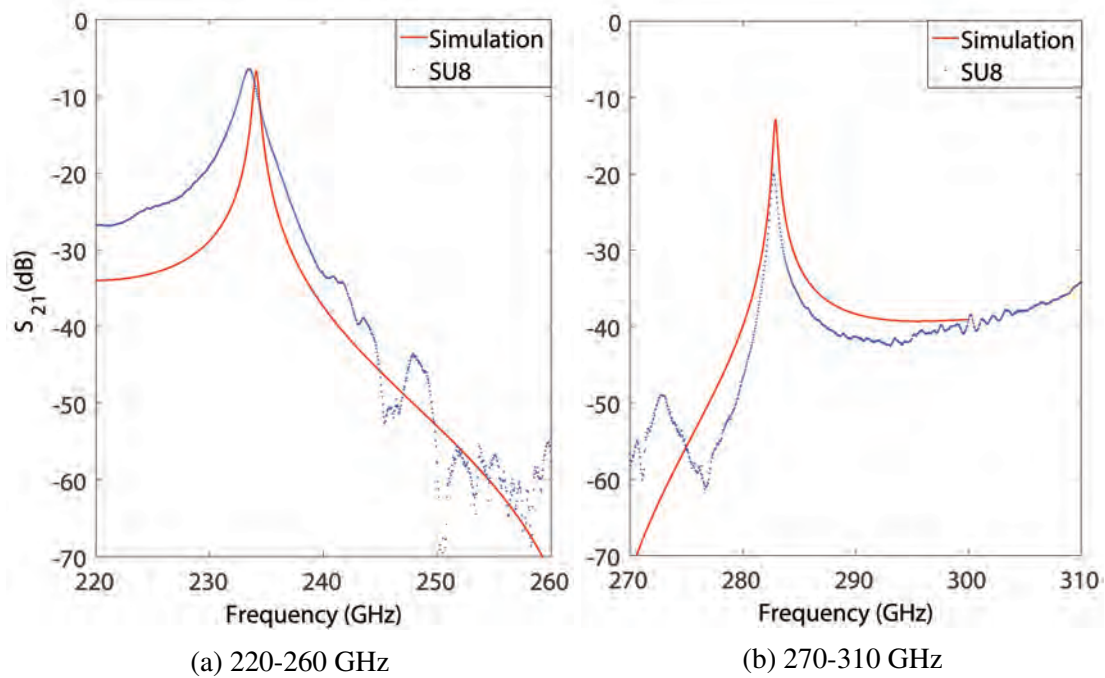


Figure 4.11: Comparison between the measurements of the SU8 resonator and simulations.

Tab. 4.3 shows the calculated unloaded Q-values, and the corresponding loss/mm from the simulations, and the measured SU8 based resonator. The loss was calculated with equation 3.6, and the uncertainty was calculated in the same way as in section 4.1.1.

Table 4.3: Measured unloaded Q-values and corresponding loss/mm for the SU8 ridge gap resonator. The simulated values from section 4.1.1 are also presented.

	Simulated		SU8	
Frequency	234.1 GHz	282.9 GHz	233.4 GHz	282.8 GHz
Q_U	866	993	$319 \pm 7.6\%$	$628 \pm 6.9\%$
Loss dB/mm	0.025	0.026	0.067	0.041

4.1.3 Carbon nanotube ridge gap resonator

Another material that has not been used before as a base material for microwave applications are carbon nanotubes (CNTs). CNTs can grow several hundred micrometers within minutes, and if they are grown with the help of CVD (see section 2.7), then they will use much cheaper gases than what the ICP plasma process does during Si processing.

In Paper VI, CNTs are used to fabricate the ridge gap resonator, to determine how successful CNTs as a base material can be. The design is the same as the one presented in section 4.1.1, with one pin row on each side of the ridge.

The process presented in Paper VI starts with patterning of a negative resist on the Si wafer. The catalyst, consisting of 5 nm Al and 2 nm Fe, is evaporated on the wafer and then the negative photoresist is removed, leaving a pattern of the catalyst by lift-off, Fig. 4.12a. The growth of CNTs is a bottom-up process compared to previous mentioned processes. The catalyst-patterned wafer is placed inside the CVD chamber. The catalyst is first pre-treated with a hydrogen gas at 500°C for 3 min to be activated. The temperature is then raised within seconds to 700°C, where it stays at 700°C for 3 min. It is during this time that the CNT growth process is performed (see section 2.7), Fig. 4.12b.

Two different samples are processed individually, but with the same process time. The samples had a pin height of $283 \pm 5 \mu\text{m}$ respectively $287 \pm 5 \mu\text{m}$, now referred as CNT A and CNT B. Because the growth is so fast, it is difficult to achieve the exact target height, since seconds can result in ending up a few micrometers off target.

As the CNTs are used as a base material because of their rapid growth, and not their physical properties, they need to be covered with a conductive metal, Fig. 4.12c. At first they were sputtered with 1 μm Al, 20 nm Ti and 100 nm Au. The thin layer of Ti and

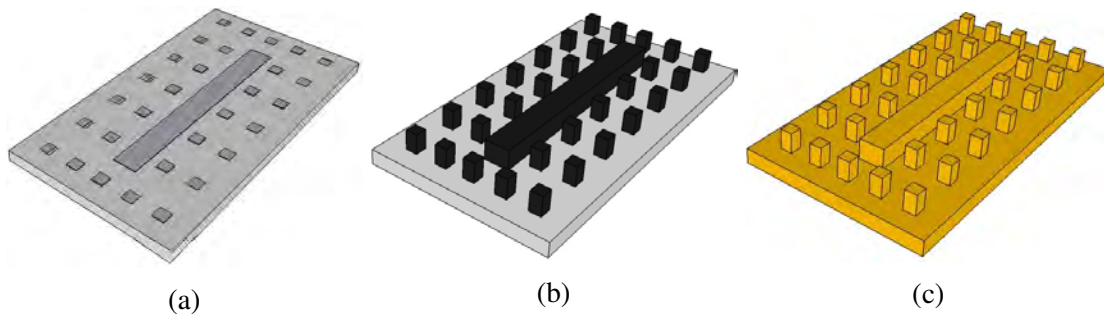


Figure 4.12: (a) The wafer with the patterned catalyst. (b) The CNTs are grown for the desired length. (c) The wafer is covered with Au.

Au was to avoid oxidation of the Al. The initial measurements of the samples CNT A and CNT B, presented in Fig. 4.14, shows a quite low loaded Q .

To increase the loaded Q -values, the samples were sputtered with 20 nm Ti and 1 μm Au, so as to increase the loaded Q -values. As can be seen in Fig. 4.13, the metal coverage is better after Au was sputtered on the tubes. CNT A and CNT B were then measured again (Fig. 4.14) and the loaded Q -values had increased.

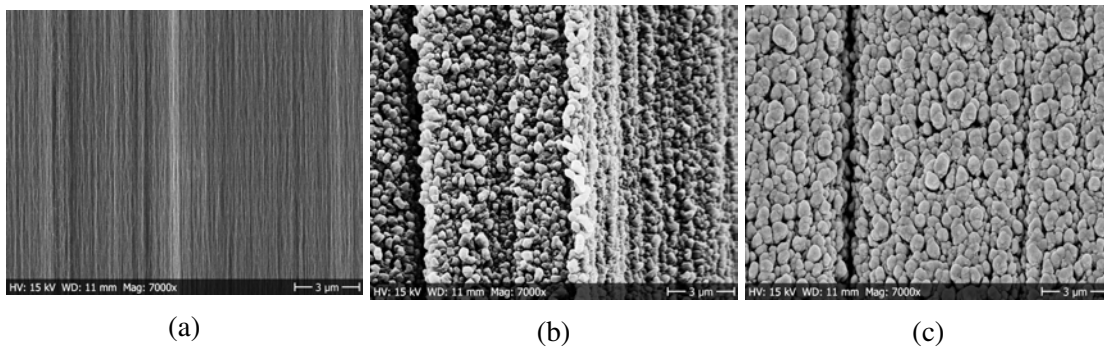


Figure 4.13: The side walls of the CNTs (a) before sputtering, (b) after sputtering of Al and Fe, and (c) after the additional sputtering of Au.

The CNTs cannot be electroplated as the previous ridge gap resonators since if they are immersed in the electroplating solution, the CNTs would start to bundle together, and they will not form pin structures anymore. The calculated unloaded Q -values together with their uncertainty and corresponding attenuation (dB/mm) for the best sample (CNT B) are presented in Tab. 4.4.

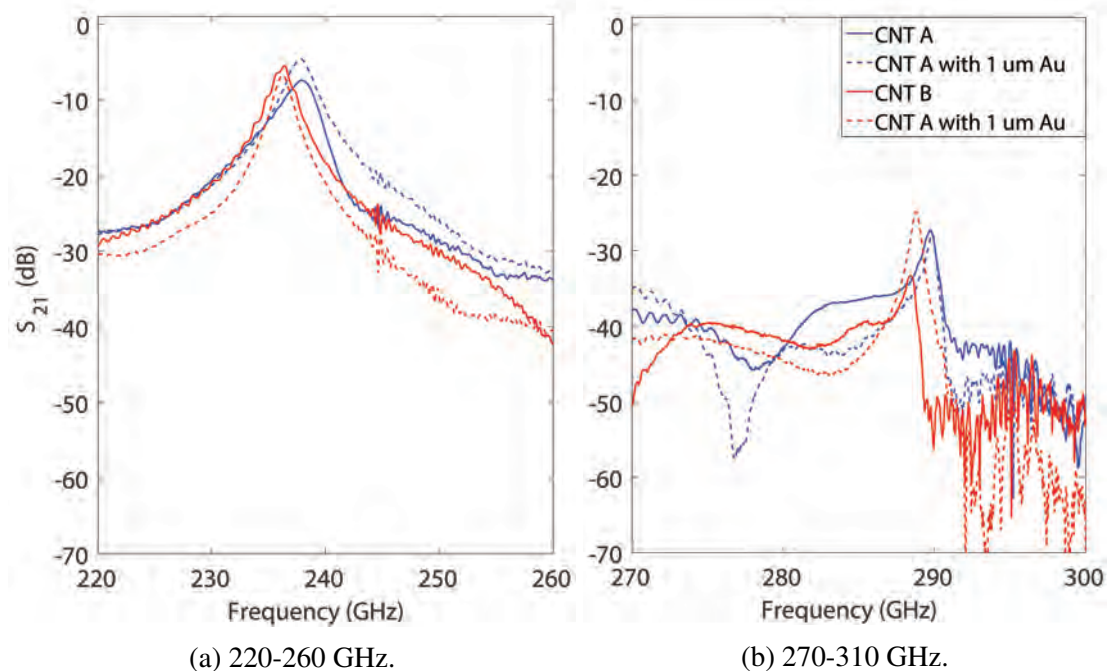


Figure 4.14: Measurement of CNT A and CNT B before and after sputtering of Au. The measurement was performed for two ranges to be able to increase the number of measurement points, thus more accurate loaded Q-values can be measured.

4.1.4 Discussion

The Si fabrication process was fairly straight forward. Only one depth was etched and only one etch mask was needed. The process gave a height of $277 \mu\text{m} \pm 10 \mu\text{m}$. The walls of the pins were slanted due to under etch (Fig. 4.10), this shape is similar to the inverted pyramid pin which could give a wider bandwidth (section 3.2). For pins of this size, the under etch is not a problem, but for tall pins, the under etch can cause the pins to collapse (section 2.2.1).

The SU8 pins have vertical walls, as they are defined by UV light (section 2.6). The height distribution of the wafer mentioned in Paper V was $\pm 20 \mu\text{m}$, which is larger than the distribution for Si. In Paper V it is stated that the SU8 process takes about the same time as the Si process (not considering the removal of the Si wafer), however the cost of the tools and material needed are lower. A way not to sacrifice the Si wafer could be to spin *Omnicoat* on the Si wafer before the SU8 process. *Omnicoat* acts as a release layer and is dissolved with a development solution. This way, the SU8 structures can be released without sacrificing the Si and thus reducing the process time.

The CNTs can also offer vertical pins and a growth time of only a few minutes. The

Table 4.4: Measured unloaded Q-values and corresponding loss/mm for the CNT ridge gap resonator. The simulated values from section 4.1.1 are also presented.

	Simulated		CNT B	
Frequency	234.1 GHz	282.9 GHz	236.2 GHz	288.8 GHz
Q_U	866	993	$274 \pm 7.5\%$	$518 \pm 6.9\%$
Loss dB/mm	0.025	0.026	0.079	0.051

CNT process is cheaper than the Si process, however not as cheap as the SU8 process. It was also found that the CNT "forests" making up the pins are not dense enough, even after two attempts of covering the pins with both Al and Au, the SEM images still showed a porous material. The two presented samples showed a pin height variation of $285 \pm 7 \mu m$. However, the target height was difficult to achieve due to that a difference in seconds could give a height difference of several micrometers.

The removal of two pin rows from each side of the resonator increased the transmission enough to measure on it, compared to previously when the resonance peaks were below the noise floor. Although now there is new equipment available to measure at these frequencies, which may be able to measure resonance peaks around $-60 dB$. It would be interesting to remeasure the ridge gap resonator with three pin rows on each side of the ridge with the new equipment.

The calculated unloaded Q-values and the loss for the Si, SU8 and CNT ridge gap resonator are presented in Tab. 4.5. The reason of the shift in frequency of the SU8 resonator and the CNT resonator can be the difference in pin height. As mentioned in section 3.2, it is stated that the start and stop frequencies of the stop band depend on the pin height. A short pin height would shift the stop band to higher frequencies, and a tall pin height would shift the stop band to lower frequencies.

Table 4.5: The calculated unloaded Q-values and loss from simulation and measurements of the Si-, SU8-, and Carbon nanotube ridge gap resonator.

	Simulated		Si		SU8		CNT B	
Frequency (GHz)	234	284	234	284	233	283	236	289
Unloaded Q	859	992	642	597	319	628	274	518
			$\pm 9.2\%$	$\pm 7.1\%$	$\pm 7.6\%$	$\pm 6.9\%$	$\pm 7.5\%$	$\pm 6.9\%$
Loss (dB/mm)	0.025	0.026	0.033	0.043	0.067	0.041	0.079	0.051

For the low frequency resonance, the Si ridge gap resonator shows the lowest attenuation, while for the high frequency resonance, the SU8 resonator shows the lowest loss. The CNT resonator had the highest loss for both resonance frequencies. The reason is probably its high surface roughness ($rms = 127 nm$ on top of the ridge and pins), compared to the Si resonator surface roughness ($rms = 34 nm$), as well as the porous

side walls of the CNT resonator, as seen in Fig. 4.13.

The gold quality of all resonators also affects the loss. In [99] it is mentioned that if surface irregularities are larger than the skin depth, then the propagation path would be longer, thus the attenuation would be larger. There is also a question of accuracy, the second resonance peak for all devices are below -20 dB, thus the impact of the external losses are less than for the first resonance peak which are all higher than -10 dB. The Si ridge gap resonator shows overall the best performance out of all the described devices.

4.2 Gap Adapters

An issue that appeared when measuring on the original three pin row ridge gap resonator in section 4.1.1 (Paper I) was to have a good electrical contact between the standard WR03 measurement flange (Fig. 4.15a) and the measurement object. Even though the resonator needs to be weakly coupled, a gap between the measurement flange and the resonator would give too low coupling to be measured at all.

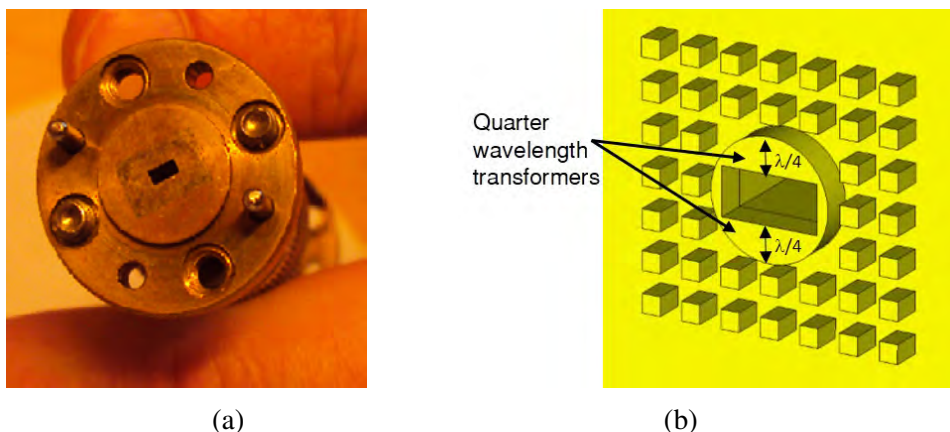


Figure 4.15: (a) Standard WR03 measurement flange opening. (b) A design of the pin-flange surface.

Fig. 4.16 shows a schematic view of the measurement setup used in section 4.1. To get good electrical contact, the measurement flange needs to be tightly screwed to the measurement package. If these screws are screwed unevenly or something is in the way, a gap can occur which will result in high leakage. Simulations of a gap of $20 \mu\text{m}$ between two waveguide flanges for the range $220 - 325$ GHz showed that the return loss would go from around -45 dB to around -15 dB [99].

Simulations of a gap waveguide based solution here referred to as the gap adapter, was presented to solve this problem [99]. The purpose of the gap adapter was to suppress leakage with the "bed of nails" structure surrounding the waveguide opening.

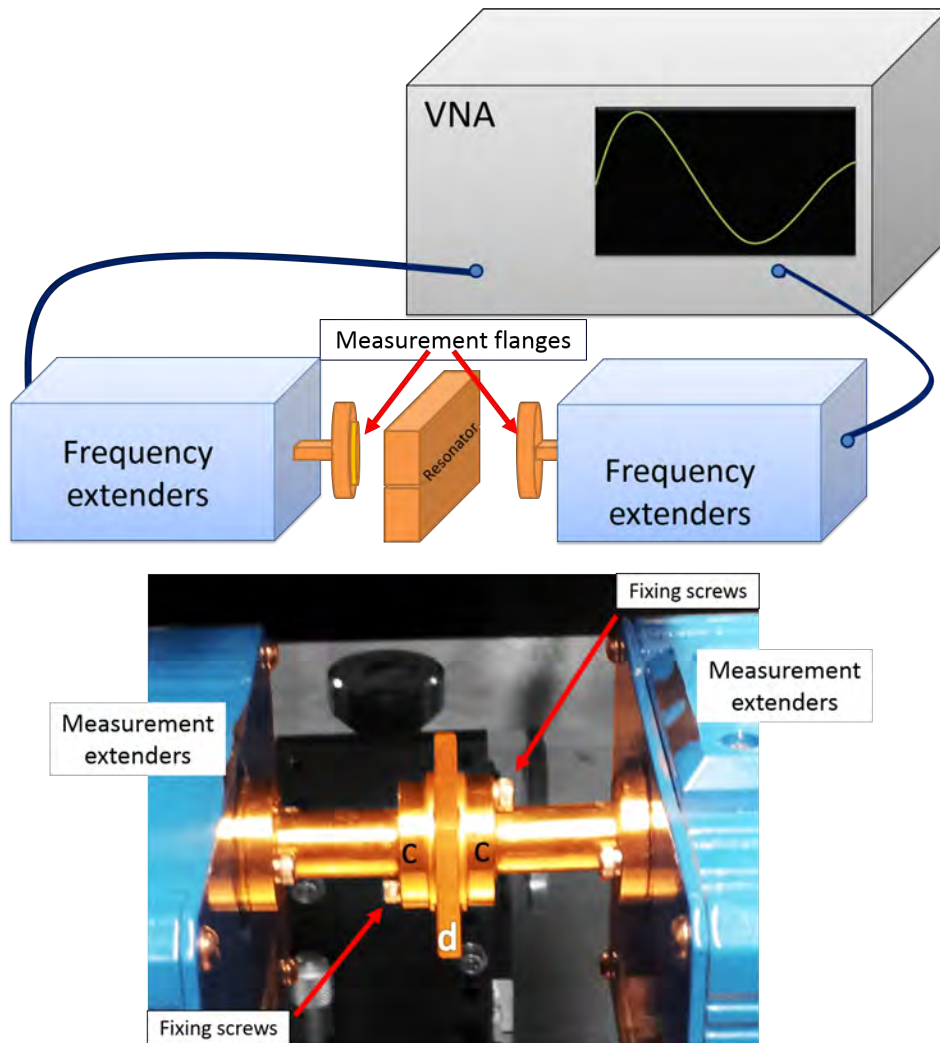


Figure 4.16: The measurement setup used in section 4.1.

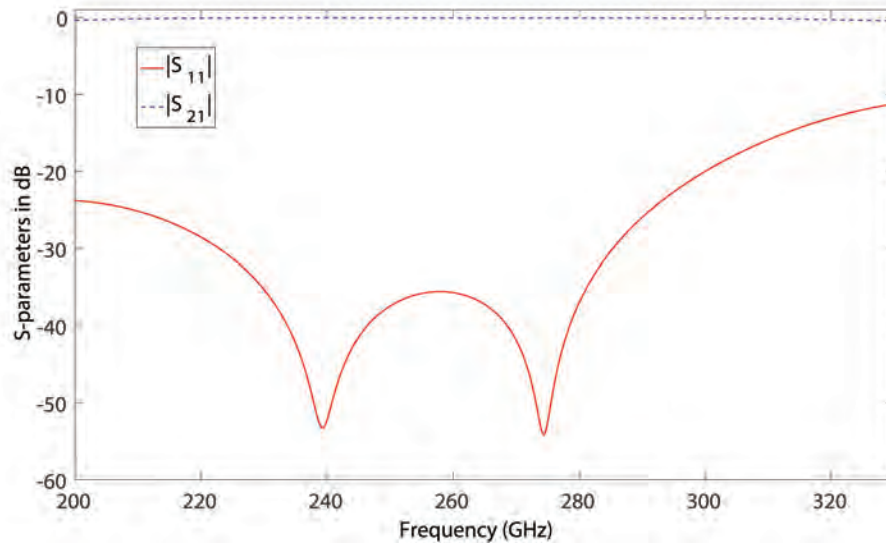


Figure 4.17: Simulation of standard waveguides connected to a double-sided pin-flange adapter as shown in Fig. 4.19c

In Fig. 4.15b, a close up of the gap adapter design presented in [99] can be seen. Around the waveguide opening there is a round wall. At the waveguide opening's widest side, the wall is $\lambda/4$ wide, so that the wall acts as an impedance transformer, from open to short circuit. The purpose of the wall is to avoid reflections that can occur between the flange and the measurement object. Around the wall, two pin rows are placed on each side to create the AMC surface around it, which is the minimum number of rows needed to create an AMC surface.

The gap adapter presented in [99], was a flange with the AMC surface around its opening. In Paper II, it was proposed to change the design to be a double-sided gap adapter. This way, the gap adapter can be placed on any WR standard flange without performing any changes to the standard measurement equipment, see Paper II. The simulation of the double-sided gap adapter can be seen in Fig. 4.17.

4.2.1 280 GHz gold plated brass prototype

In Paper II, a gold plated, double-sided brass prototype was presented, see Fig. 4.18. The prototype was milled with CNC milling, it was compared to a double-sided choke flange and a reference flat plate, Fig. 4.18. The choke flange has a $\lambda/4$ deep ring around the waveguide opening with the same purpose as the pin-surface in the gap adapter.

Two types of measurements were done on these milled brass prototypes. The first set of measurements only measured on the brass flanges alone. That is, the reference plate,

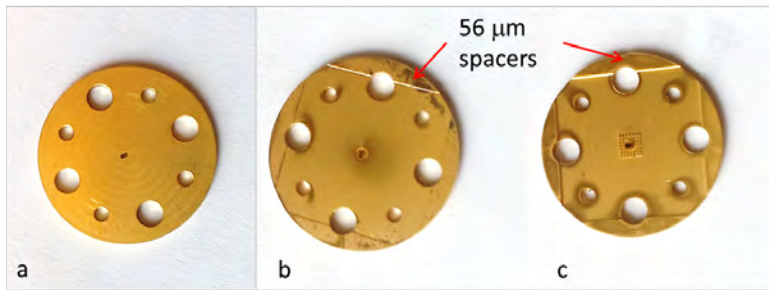


Figure 4.18: The milled double-sided brass: a) flat reference plate, b) choke flange, and c) gap adapter.

the choke flange and the gap adapter were each placed between the two measurement flanges in Fig. 4.16 and measured back-to-back as in Fig. 4.19.

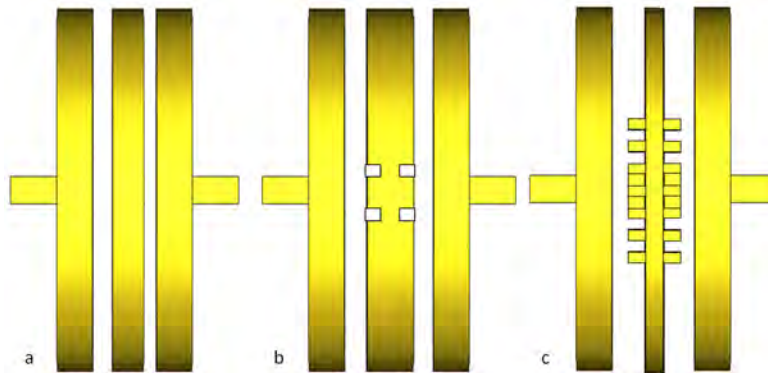
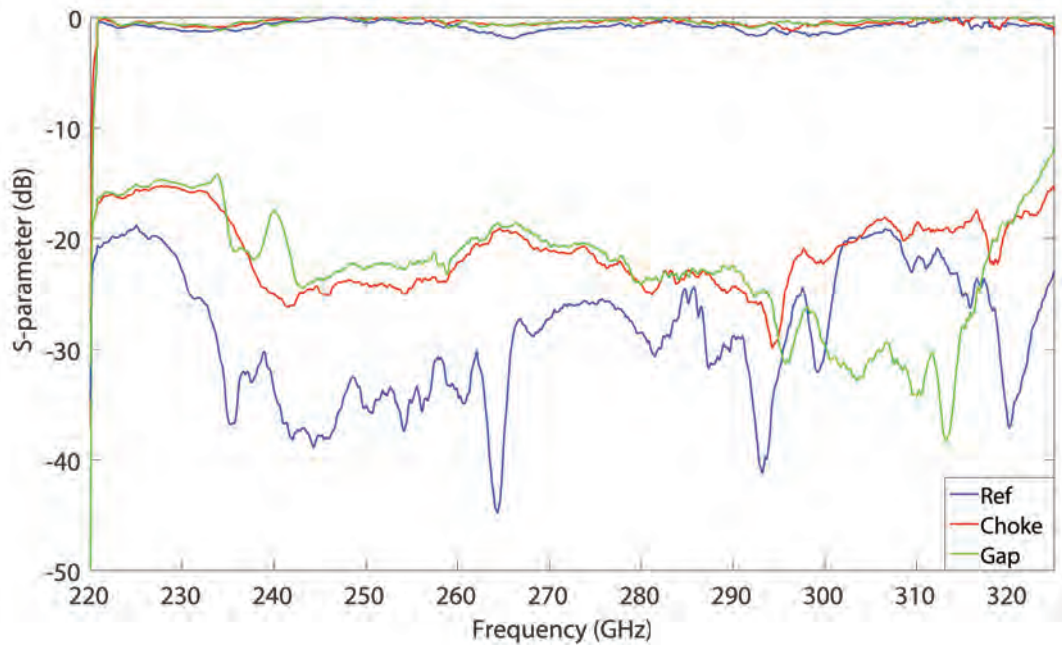


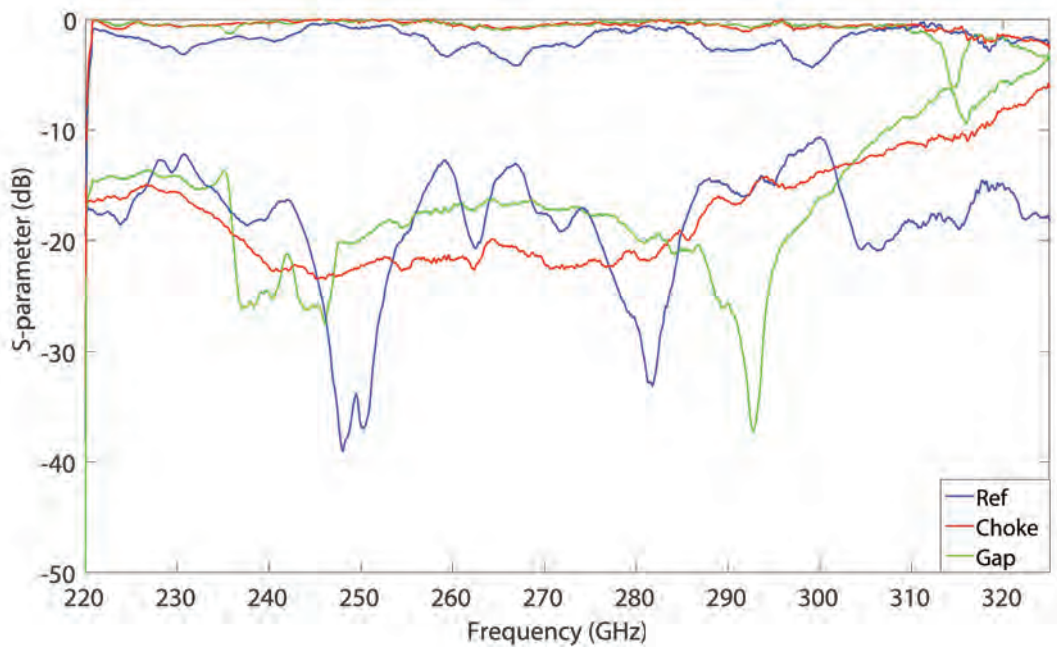
Figure 4.19: Measurement setup for comparing the different flanges. (a) Measurement setup for the flat reference plate, (b) measurement setup for the double-sided choke and (c) the measurement setup for the double-sided gap adapter.

Each of the setups in Fig. 4.19 was tested for two cases: with and without screws. The results can be seen in Fig. 4.20a.

The second type of measurement was done on a straight rectangular waveguide section of 25.425 mm , with the measurement flanges connected directly to the straight rectangular waveguide section, and for two of the prototypes: the double-sided gap adapter, the double-sided choke flange. The setup can be seen in Fig. 4.21 where the double-sided gap adapter can be replaced with a double-sided choke flange instead. The measurements can be seen in Fig. 4.22, the double-sided gap adapter and the double-sided choke flange are comparable to when the measurement flanges are connected directly to the straight rectangular waveguide section.



(a) With screws



(b) Without screws

Figure 4.20: Measured S_{11} and S_{21} of the setup in Fig. 4.19 with a $50 \mu\text{m}$ gap on each side, double-sided gap adapter (green), double-sided choke (red) and the standard flanges (blue).

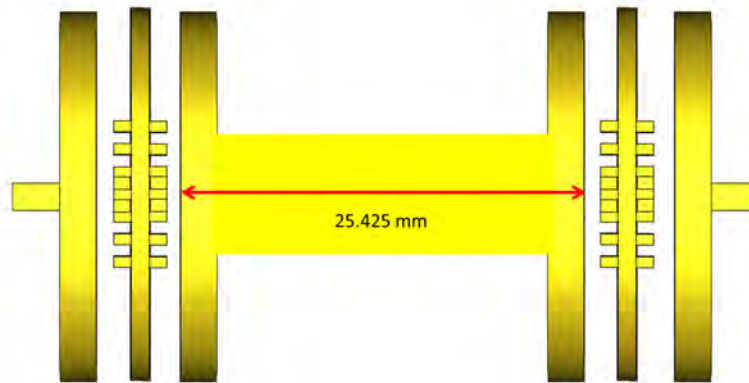


Figure 4.21: Measurement setup for comparing the straight rectangular waveguide with pin flanges between the waveguide and the measurement flanges on both sides. (Spacers not shown in the figure)

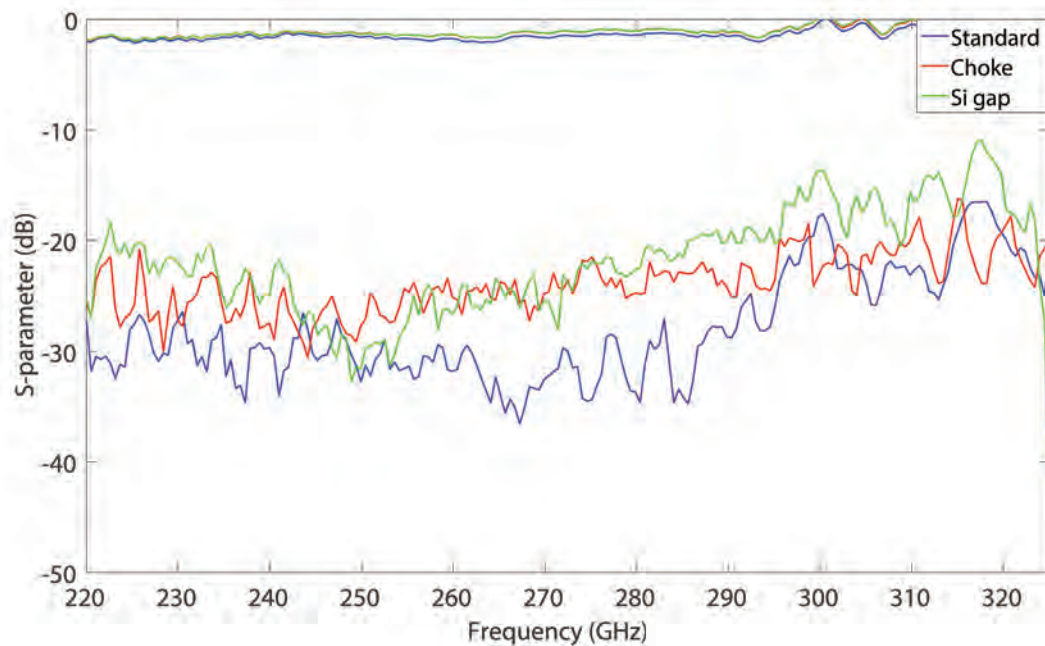


Figure 4.22: Measurements on a straight rectangular waveguide, with a length of 25.425 mm. With a standard (red line) connection, with a choke flange on each side (blue line) and with a gap adapter on each side (green line)

4.2.2 280 GHz micromachined Si gap adapter

The brass prototype presented in section 4.2.1 was CNC-milled. As mentioned in Paper II, milling at this scale has limitation of a width to depth ratio of 1:2. This means that the spacing between the pins had to be increased to enable milling of the structure. Milling is a time consuming and costly process that can only produce one gap adapter at a time. To mass-produce the gap adapter with a high precision, microfabrication can be used. In Paper II, a microfabricated Si gap adapter is presented.

The process plan can be seen in Fig. 4.23. The photomasks used here were reprinted masks (see section 2.1).

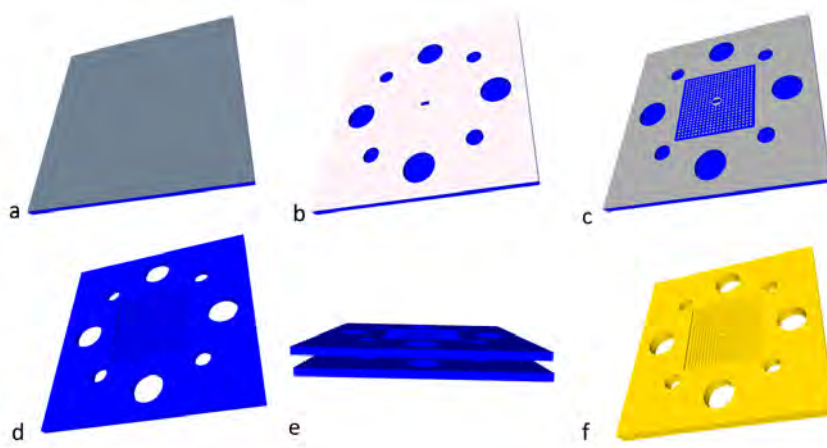


Figure 4.23: Process diagram, blue: Si, grey: Al, pink: photoresist, yellow: Au.

A 6" (150 mm) Si wafer with a thickness of 540 μm was sputtered with a 0.5 μm Al layer on the front side (Fig. 4.23a) and patterned. A layer of photoresist was spun on top of the Al layer on the front side achieving a thickness of about 6 μm . The photoresist was patterned with the second mask (Fig. 4.23b). Both layers were used as etch masks during DRIE.

The wafer was etched down to the first level of around 270 μm , the photoresist etch mask was then removed (Fig. 4.23c). Al was sputtered on the back side of the wafer to act as an etch stop to protect the chuck of the ICP (see section 2.2.2).

The wafer was then etched all the way down to the Al stop layer, after which the Al was removed (Fig. 4.23d). Two gap adapter halves were bonded back to back, Fig. 4.23e. The now double-sided gap adapter was sputtered with a seed layer of Ti/Au that was later electroplated to have a Au thickness of 1.5 μm to assure conductivity at these frequencies, Fig. 4.23f. Fig. 4.24 shows photographs of the Si gap adapter process.

The microfabricated double-sided gap adapter was used to do a tolerance study with gaps ranging from 0 – 100 μm . The gaps were realized with feeler gauges with the

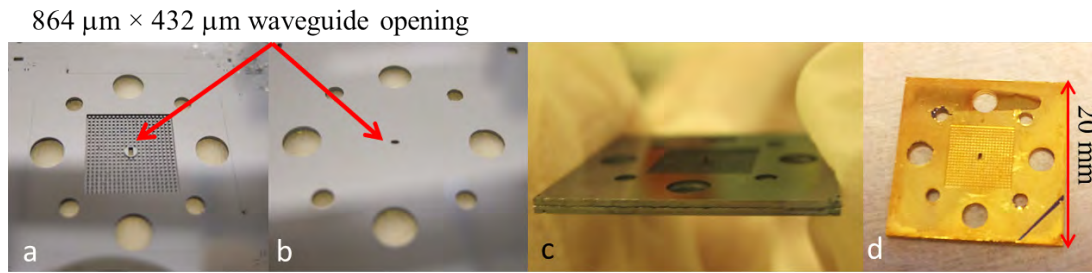


Figure 4.24: a) Front side view of the wafer after etching through the wafers. b) Back side view of the wafer after etching through the wafer. c) Side view of the two bonded pin-flange sides. d) Fully fabricated pin flange after Au-deposition.

different thicknesses. The measurements can be seen in Fig. 4.25. It was shown that a stop band was still present with a 100 μm gap. Though it is more narrow for larger gaps than for smaller gaps. This behaviour agrees with the behaviour for gap waveguide stop bands described in section 3.2.

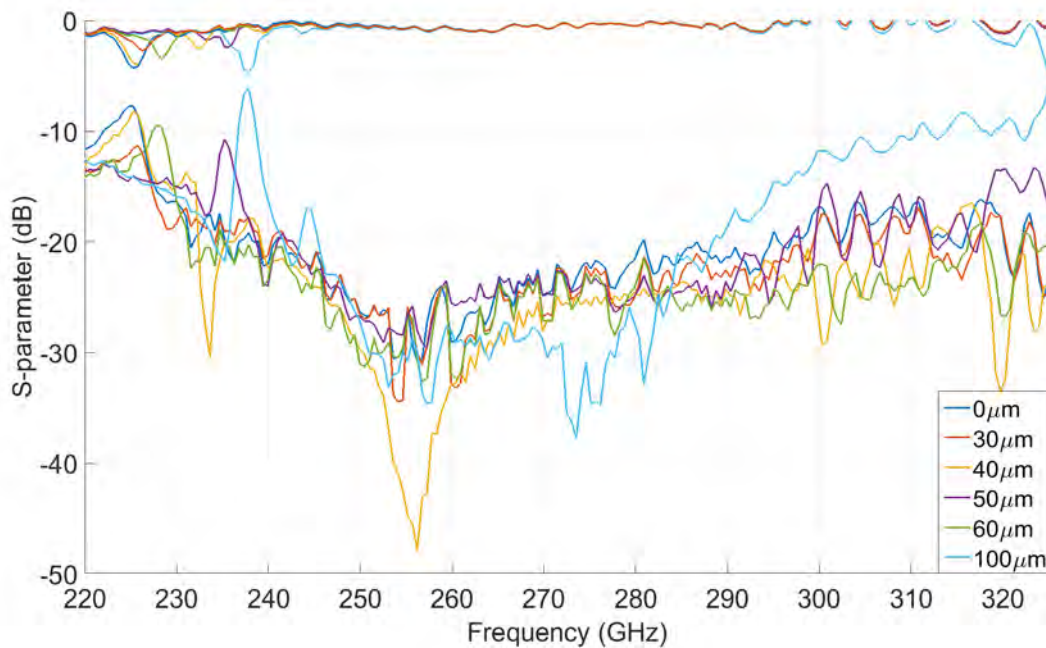


Figure 4.25: Measurements performed on the micromachined pin flange with different gaps (30 μm , 40 μm , 50 μm , 60 μm and 100 μm).

The micromachined double-sided gap adapter was also compared to the milled brass prototypes (gap adapter, choke flange, and flat reference plate). All measurements (Fig. 4.26) were performed with a $50\ \mu\text{m}$ gap on both sides with the same setup as in Fig. 4.19.

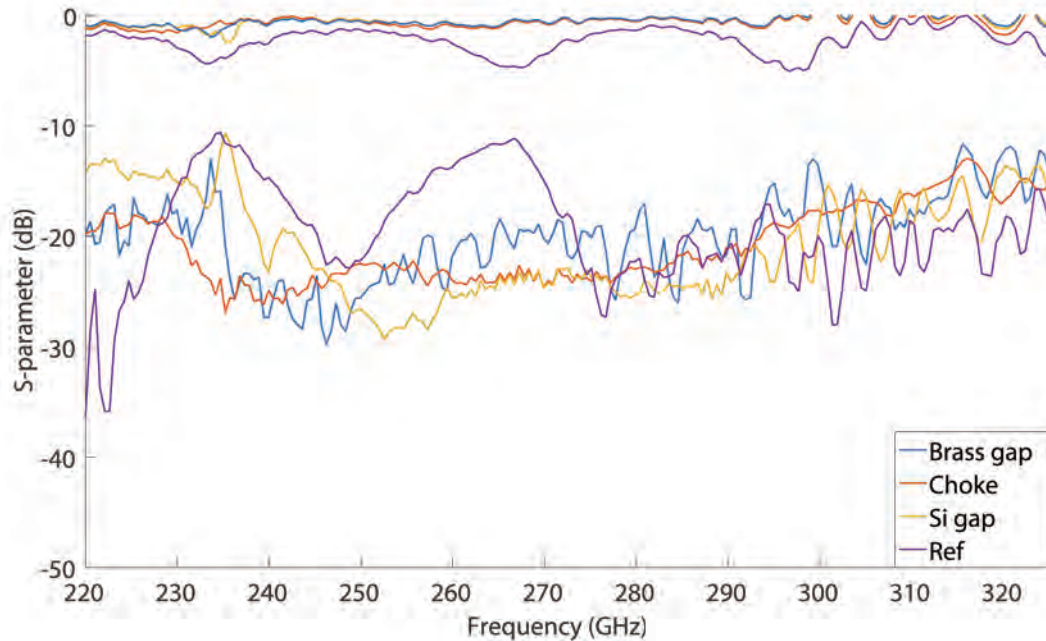


Figure 4.26: Measurements on the milled gap adapter (blue), the choke (red dashed), Si gap adapter (yellow), flat reference plate (purple) with a $50\ \mu\text{m}$ gap.

4.2.3 280 GHz micromachined SU8 gap adapter

In Paper VII, a polymer gap adapter was fabricated and measured. The polymer SU8 is a more robust material and in Paper V it was shown that gold-coated SU8 was promising for fabricating gap waveguide devices. The SU8 gap adapter is more robust than the Si gap adapter and more forgiving when it is subjected to rough handling. The SU8 fabrication process can also be done at a lower cost compared to the Si process.

The process plan can be seen in Fig. 4.27. The Si wafer is patterned with Al, to be used for alignment of the following SU8 layers. The first layer is spun to a thickness of $245\ \mu\text{m}$, followed by a soft bake step and then UV exposure through the first photo mask. The exposure defines the guiding pin holes, screw holes and waveguide opening. The next SU8 layer is spun to a thickness of about $277\ \mu\text{m}$. The whole wafer is soft baked for a longer period, and both layers were UV exposed through the second photo

mask, defining again the opening of the previous layers, and also the pin surface around the waveguide opening. After development and curing the Si wafer is removed. The SU8 gap adapter halves are diced and bonded back to back and together they make up a double-sided SU8 gap adapter. The adapter is sputtered with a seed layer of Ti/Au and then electroplated with a Au thickness of at least $1 \mu m$. When removing the gold-plated gap adapter, special care was taken not to cool it down too quickly during rinsing. If the gap adapter was rinsed in room temperature deionized water, the Au would start to wrinkle at the large open surfaces, and detach from the SU8. Therefore, the deionized water used to rinse the gap adapter after electroplating, needed to be heated and after rinsing, the gap adapter needs to cool down slowly in room temperature.

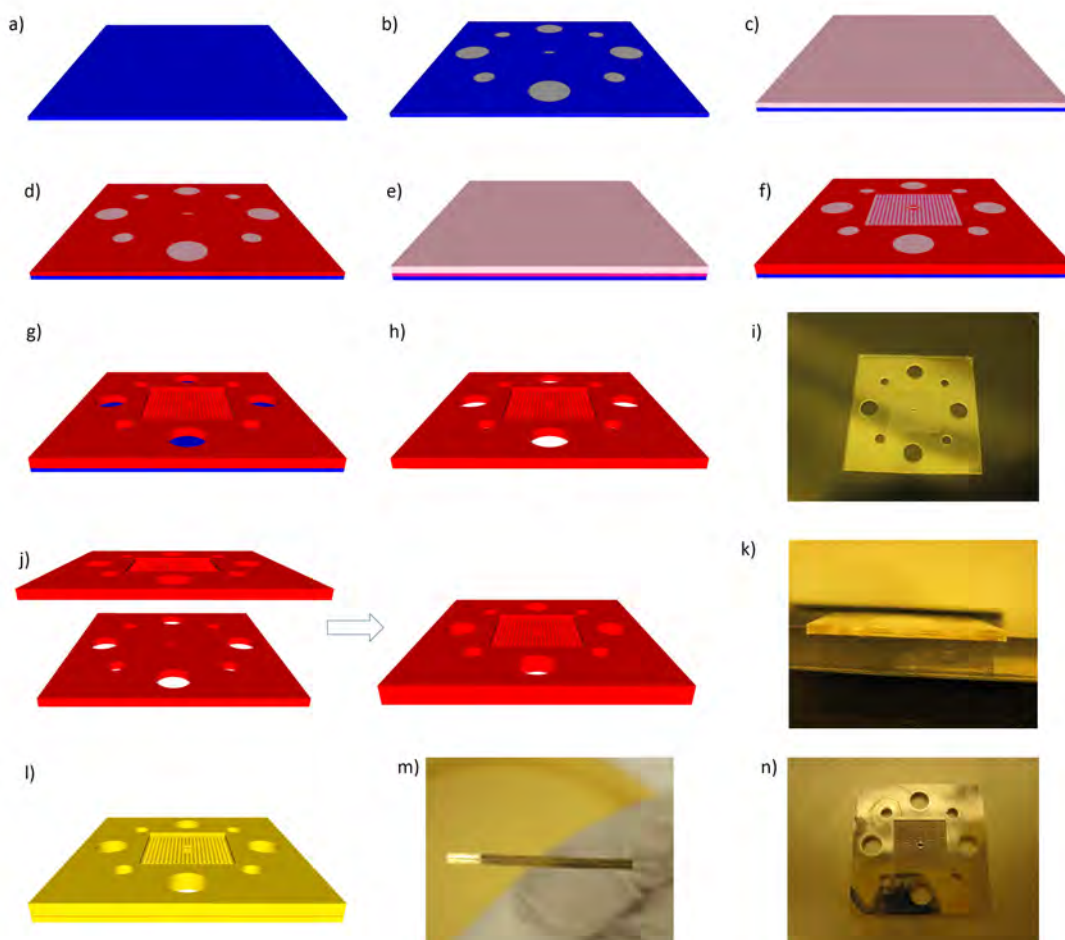
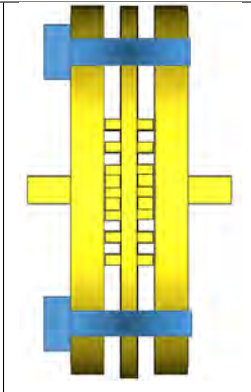
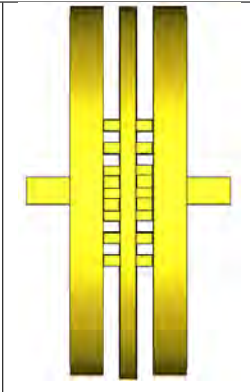
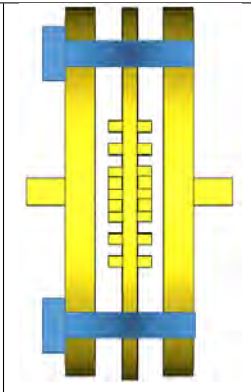
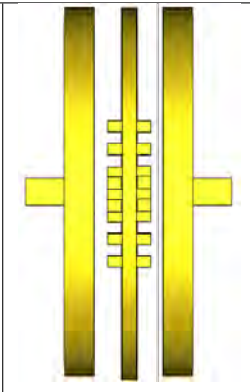


Figure 4.27: Process diagram, blue: Si, grey: Al, pink: SU8, red: cured SU8, yellow: Au.

Table 4.6: Figures of each setup of the four cases.

	Screws	No screws
0 μm gap		
50 μm gap		

The measurements in Paper II indicated that the gap adapter might not need any screws to connect to the device under test. Therefore, in Paper VII, a study with four cases was performed.

Case 1 Screws and no gap.

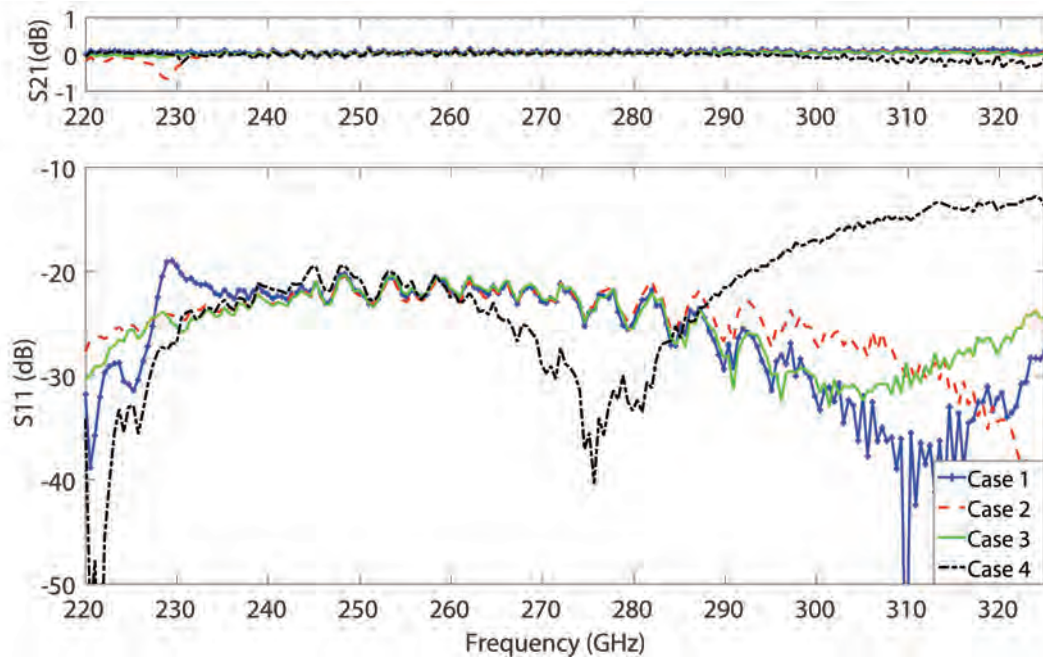
Case 2 No screws and no intended gap.

Case 3 Screws and a 50 μm gap on each side of the gap adapter.

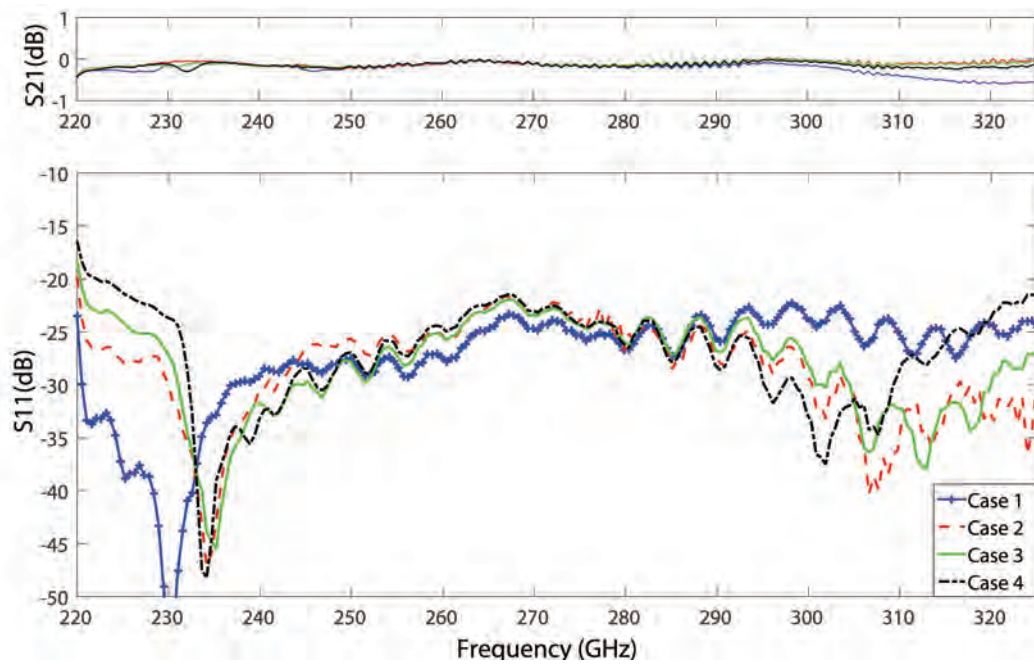
Case 4 No screws with a gap of at least 50 μm gap on each side of the adapter.

Illustrations of the four cases can be seen in Tab. 4.6. The gaps on both side of the gap adapter was realized with 50 μm feeler gauges. The measurements for the four cases for two different SU8 adapters are presented in Fig. 4.28.

The gap adapter was also compared to the Si gap adapter presented in section 4.2.2 and Paper VII, and the flat reference plate (Fig. 4.18), measurements can be seen in Fig. 4.29

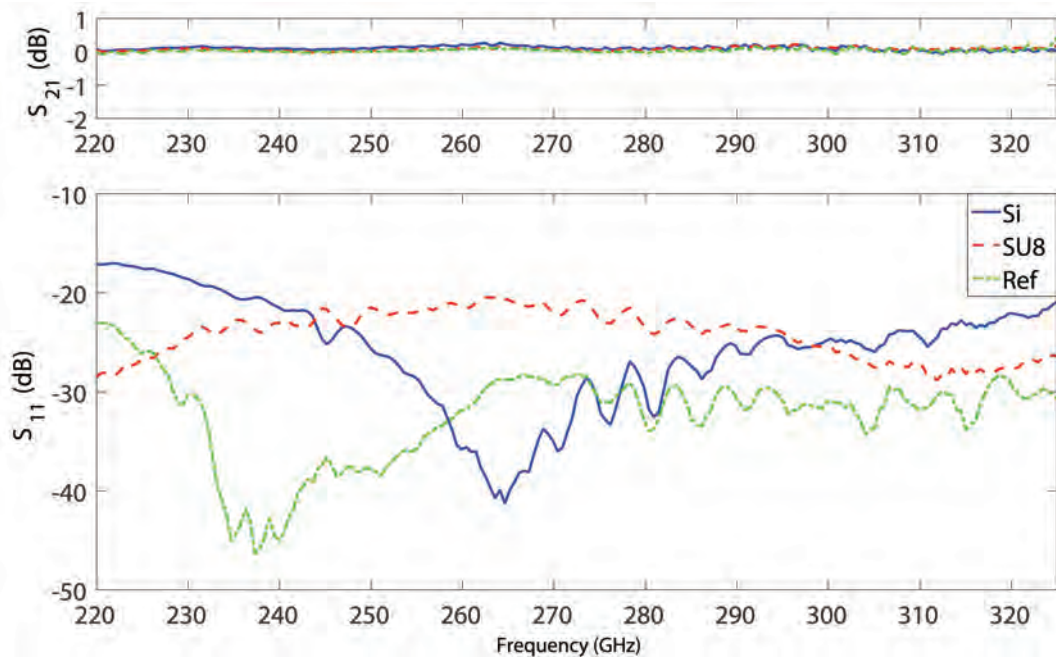


(a)

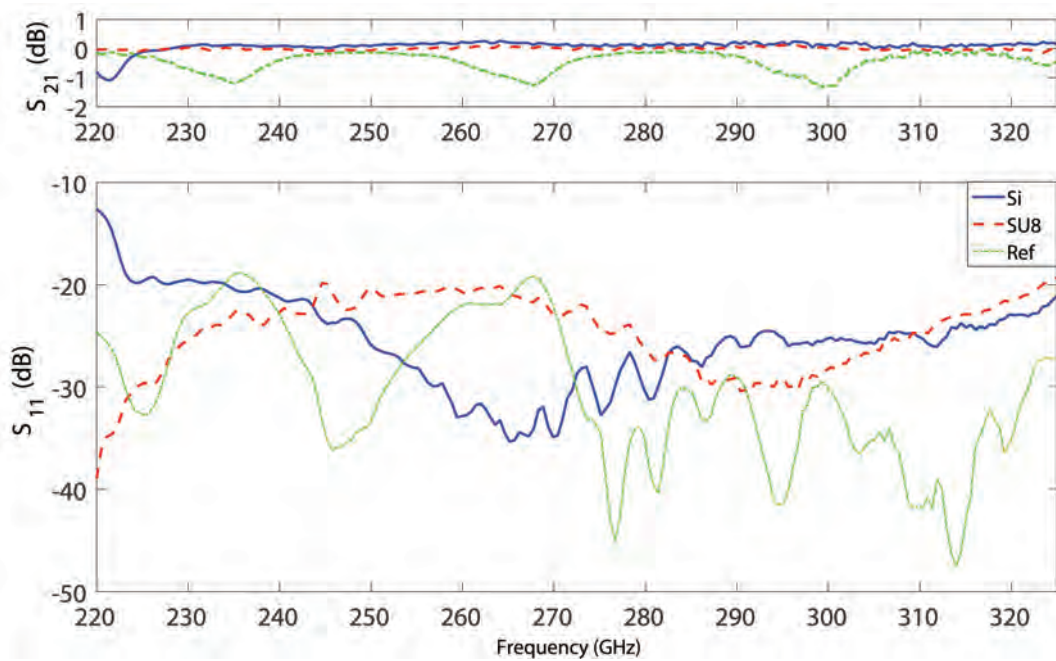


(b)

Figure 4.28: Measurements of two SU8 gap adapters from different batches. The measurements were performed for all four cases presented in Tab. 4.6.



(a) Case 1



(b) Case 2

Figure 4.29: S_{21} and S_{11} measurements on the SU8 pin-flange gap adapter (red line), the Si pin-flange gap adapter (blue line) and the flat surface reference (Ref, green line). The gap adapters and the flat surface reference are placed as the top row of Tab. 4.6.

The maximum displacement was measured and studied in Paper VII. It was concluded that a gap between the measurement flange and the device under test had a bigger impact on the return loss, compared to misalignment between two waveguide ports.

The gap adapter was dropped 25 times from 1 *m* at a marble surface and then from a height of 5 *m* without any notable damage to it.

4.2.4 Discussion

Measurements on the gap adapter for 280 *GHz* show results comparable to those on the choke flange. When the standard waveguide flanges were screwed together tightly to the flat reference plate, the return loss was lower than the double-sided gap adapter and the double-sided choke flange, however, as can be seen in Fig. 4.20a, the transmission is slightly lower. What needs to be noted is that the double-sided gap adapter and the double-sided choke flange each have a 56 μm gap on both sides between them and the measurement flanges, compared to the reference plate that has no gaps.

Without screws, the results are more clear. The return loss for the standard connection is now much higher than before and the transmission is visibly lower. For the gap adapter and the choke flange, the results are almost the same as those with screws. The gap adapter and the choke flange are thus shown to enable more reliable setups.

Overall, the brass gap adapter and the choke flange with a 56 μm gap, had a better performance than the standard waveguide flange connection with the flat reference plate in between.

By milling the gap adapter, the resolution is lowered due to the 2:1 ratio of the length and width of the micromill. The fabrication method is also limited to milling one device at a time, which is not suitable for mass fabrication.

By fabricating the gap adapter with microsystem technology in Si, the desired resolution can be achieved, and the process can be used for mass fabrication.

In the Si gap adapter process, Al was used as an etch stop instead of the traditional SiO_2 , the reason is that if the wafer would be covered in SiO_2 , there will be SiO_2 on all sides. This, in turn, would mean that the SiO_2 on the front needed to be either removed or patterned. Al was chosen as an etch mask due to its sharp resolution. SiO_2 would probably lead to less re-sputtering, although, this was not noticed.

The Si gap adapter with 50 μm gaps on each side showed comparable results to the brass gap adapter with 56 μm gaps on each side. The flat reference plate, however, showed an insertion loss at -5 dB and a return loss at -10 dB with a 50 μm gap, indicating a huge leakage.

A tolerance study was performed on the Si gap adapter and a stop band was present even with gaps of 100 μm , although more narrow than for smaller gaps. The measurements in Fig. 4.28 show that to keep a stop band ($S_{11} < -20 \text{ dB}$) for the whole frequency range, the gap should not exceed more than 50 μm .

The Si gap adapter is sensitive to rough handling and will crack if not mounted properly. Therefore, an SU8 polymer gap adapter was investigated. SU8 is cheaper than Si, it can give high aspect ratio and high resolution structures, it is robust, and it survived a drop test from 5 m.

The previous measurements with the Si gap adapter led to a study with the SU8 gap adapter that investigated the need for screws. The study showed that with and without screws, and with gaps up to 50 μm , the performance was the same. In Fig. 4.28, two SU8 gap adapters are measured for the same four cases. The SU8 gap adapter in Fig. 4.28a shows the same performance up to 50 μm gaps and for the fourth case (gaps $> 50 \mu\text{m}$) the stop band is smaller but the behaviour is similar to the simulation in Fig. 4.17. The SU8 gap adapter in Fig. 4.28b shows a lower return loss and a wider stop band than gap adapter in Fig. 4.28a. The reason is that they are from two different batches with probably a slight difference in pin height.

The SU8 gap adapter was also compared to the Si gap adapter and a flat surface reference. The SU8 gap adapter showed comparable results (Fig. 4.29) to the Si gap adapter for all four cases in Tab. 4.6. The flat reference indicates leakage already for case 2, which is increased for case 3 and 4. The Si gap adapter and flat reference plate performed slightly better in Fig. 4.29 than for the same case in Fig. 4.26. The most notable difference between these measurements is that the measurement in Fig. 4.26 was performed with old and worn measurement flanges, and calibration kit from *Hewlett Packard*, while the measurement in Fig. 4.29 was performed with a new set of measurement flanges, and newly acquired Virginia Diodes' calibration kit WR-3.4. It would be interesting to perform the tolerance study with the later setup. However, according to simulations, the general behaviour of the stop band becoming narrower for a larger gap will not change.

4.3 100 GHz Gap Waveguides

Paper III and IV presents three kinds of groove gap waveguides and four kinds of ridge gap waveguides designed and fabricated for F-band (90-140 GHz). They were all fabricated with the same process utilizing SOI wafers to achieve uniform pin-height during ICP DRIE. The buried oxide layer acts as an etch stop, allowing all pins to be etched to the same height as mentioned in section 2.5.

A 6" SOI wafer was sputtered with 1 μm Al and patterned using lithography (Fig. 4.30a and b). The pin structures were etched with DRIE (Fig. 4.30c) and the etch process was tuned to assure that even the smallest pins with a width of 150 μm would survive (see section 2.2.2). The wafer was later stripped, diced and sputtered with a seed layer of Ti/Au. The devices were then electroplated in the same procedure described in section 2.4 (Fig. 4.30d).

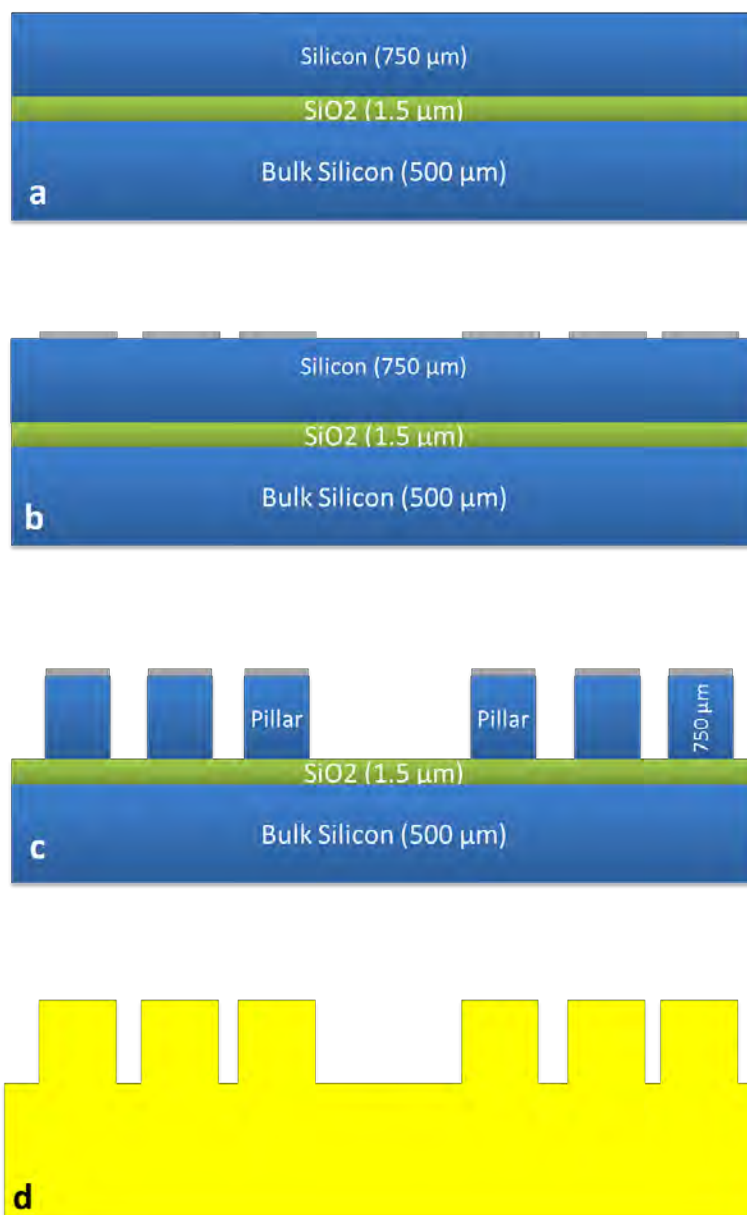


Figure 4.30: a) A 6" SOI wafer. b) The wafer is then patterned with an Al etch mask. c) DRIE was used to etch down to the oxide to achieve an uniform pin-height. d) The wafer was diced, sputtered with Ti/Au and then electroplated with Au.



Figure 4.31: The measurement fixture for the groove gap waveguide, where the PEC metal lid is incorporated in the top part of the fixture.

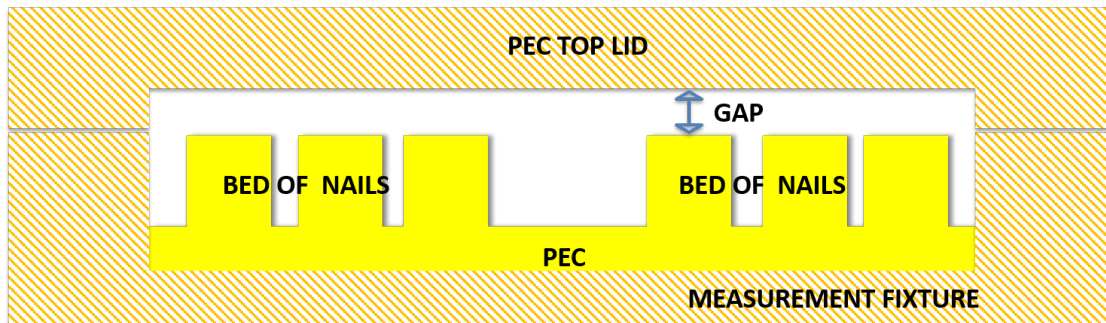


Figure 4.32: Schematic close-up of the measurement fixture for the groove gap waveguide, where the PEC metal lid is incorporated in the top part of the fixture.

As in Paper I, support structures used to connect to the measurement flanges were also fabricated. They also acted as the electrically conductive lid needed above the gap waveguide. The support structures were milled in brass and then electroplated with Au (Fig. 4.31 and Fig.4.32).

4.3.1 100 GHz Groove Gap Waveguides

Measurements were performed on the groove gap waveguides and the results were compared to simulations in Paper III. Three devices were fabricated: a straight waveguide, a waveguide with two 90° bends and a resonator (Fig. 4.33). The benefit of the groove gap waveguides is that they do not need any transition structure to connect to a standard rectangular waveguide, like the ridge gap waveguide in section 4.1. To create a stop band at these frequencies, the pin height needs to be $750 \mu m$. The width of the pins varies depending on where it is placed and what the pins purpose is. The smaller pins

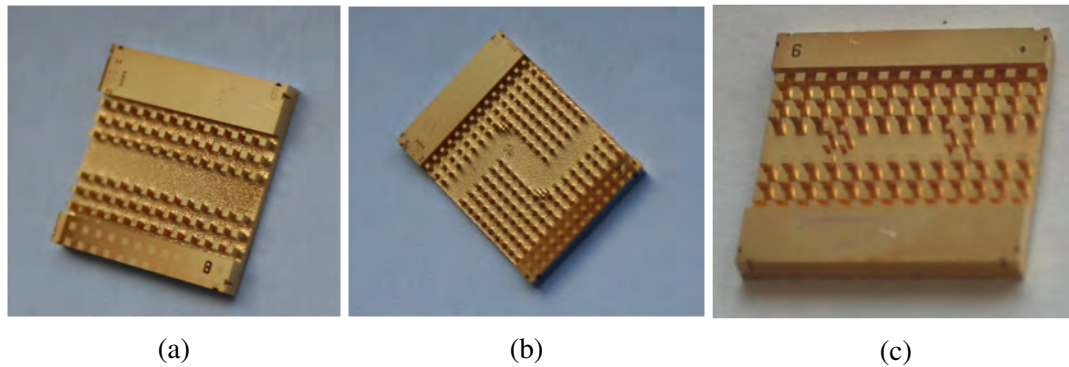


Figure 4.33: (a) Straight groove gap waveguide, (b) groove gap waveguide with two 90° bends, (c) groove gap resonator.

in the corners of the 90° bend waveguides path in Fig. 4.34b are used to smoothen the corners, so as to reduce reflection. The smaller pins in Fig. 4.34c defines the resonance cavity and the weak coupling to it, whereas the larger pins create the "side walls".

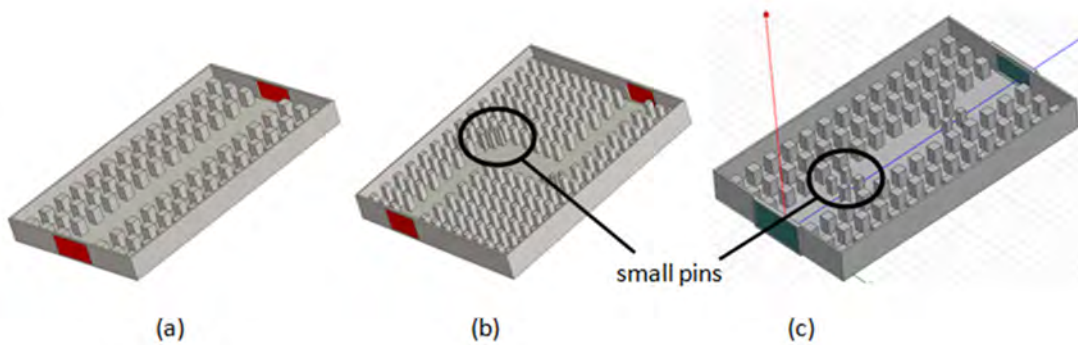


Figure 4.34: The simulated designs of the groove gap waveguides a) straight waveguide, b) waveguide with the two 90° bends and c) resonator.

The groove gap waveguides were designed for F-band ($90 - 140 \text{ GHz}$) but the only measurement equipment available at that time, was for W-band ($75 - 110 \text{ GHz}$). The W-band measurement equipment could, however, be adjusted to measure up to 118 GHz . The return loss for the straight waveguide was below -10 dB between $90 - 118 \text{ GHz}$ (Fig. 4.35) and for the waveguide with two 90° bends the return loss was below -15 dB between $97 - 118 \text{ GHz}$ (Fig. 4.36).

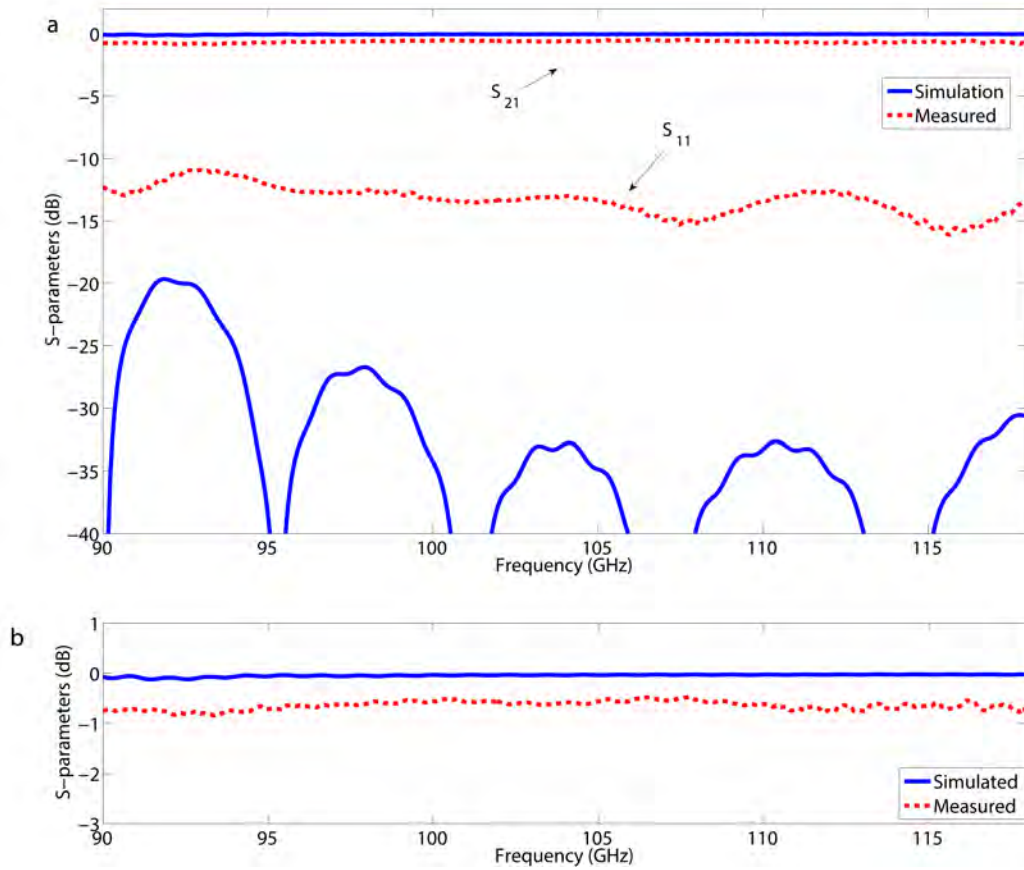


Figure 4.35: a) Simulated (solid blue line) and measured (dashed red line) S_{11} and S_{21} for the straight waveguide from 90 to 118 GHz. b) Shows a close up of S_{21} in the same frequency range for the dB range -3 to 1 dB.

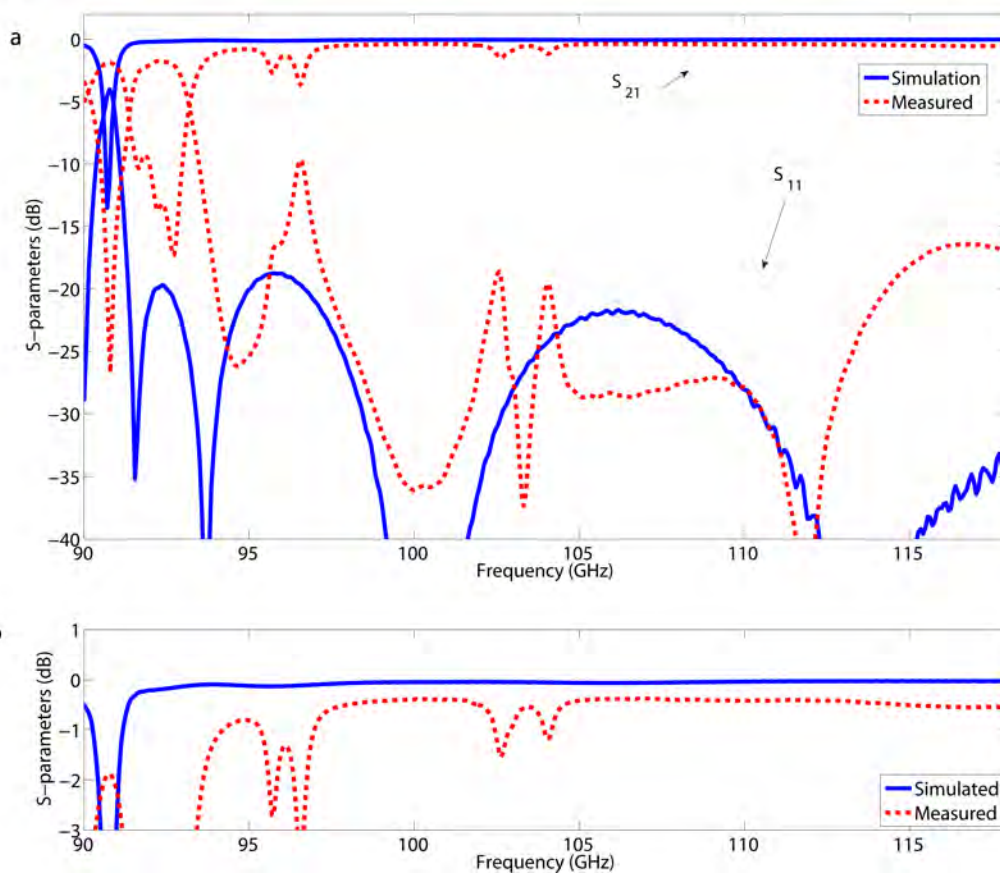


Figure 4.36: a) Simulated (solid blue line) and measured (dashed red line) S_{11} and S_{21} for the waveguide with two 90° bends from 90 to 118 GHz, b) shows a close up of S_{21} in the same frequency range for the dB range -3 to 1 dB.

Tab. 4.7 shows the simulated and measured Q -values for the groove gap resonator. As seen in the close-up of Fig. 4.35 and 4.36 there is a difference between the simulated and measured transmission constant. To be able to interpret these results one needs to remove the effect of the outer components such as the feeding network (section 3.5) and calculate the unloaded Q . If the groove gap waveguide is approximated to be a TEM line, equation 3.6 can be used to determine the attenuation for the straight and the 90° bent waveguide. Tab. 4.8 from Paper III shows the simulated and measured S_{21} at 100 GHz and 110 GHz for the straight and the 90° bent waveguide. It also shows the approximated attenuation calculated from measurement.

Table 4.7: Simulated and measured Q s for the groove gap resonator

	Q_1	Q_2
Simulated	760 at 99.75 GHz	2000 at 119.9 GHz
Measured	1210 at 95.64 GHz	1160 at 115.60 GHz

Table 4.8: Attenuation in the straight groove gap waveguide and the groove gap waveguide with two 90° bends.

	Straight waveguide ($L = 12.8 \cdot 10^{-3} m$)		90° bend waveguide ($L = 13.7 \cdot 10^{-3} m$)	
	100 GHz	110 GHz	100 GHz	110 GHz
Frequency	100 GHz	110 GHz	100 GHz	110 GHz
Simulated $ S_{21} $ of waveguide:	0.03 dB	0.03 dB	0.05 dB	0.04 dB
Measured $ S_{21} $ of waveguide:	0.56 dB	0.62 dB	0.38 dB	0.42 dB
Frequency	95.64 GHz	115.60 GHz	95.64 GHz	115.60 GHz
Estimated from measured Q s of resonator:	0.09 dB	0.10 dB	0.12 dB	0.12 dB
Corresponding per wavelength from Q s:	0.022 dB	0.024 dB	0.022 dB	0.024 dB

4.3.2 100 GHz Ridge Gap Waveguides

In Paper IV, the ridge gap waveguide is presented in four different varieties, a straight, a bent and two resonators, Fig. 4.37. The difference between the two resonators is that there are one or two pin rows separating the resonance ridge from the waveguide port, Fig. 4.37c and d. The number of pin rows separating them determines how strongly coupled the resonator is. As mentioned earlier, a weakly coupled resonator gives a more accurate Q_U , although it is more difficult to measure it.

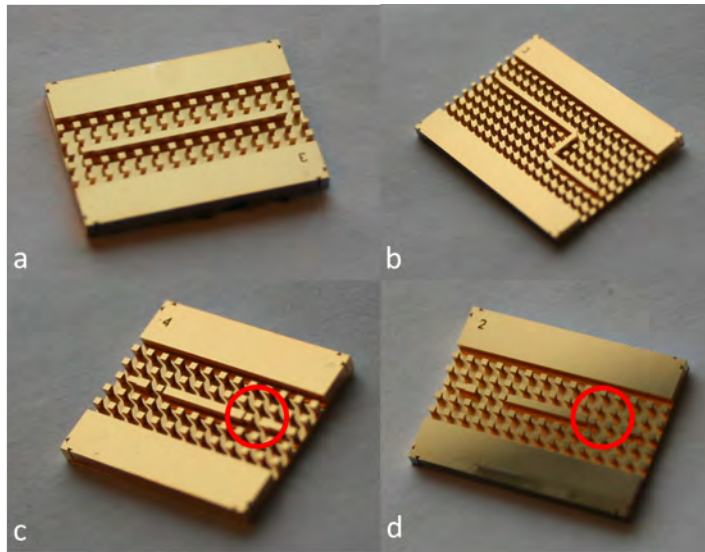


Figure 4.37: a) Straight ridge gap waveguide, b) ridge gap waveguide with two 90° bends, c) ridge gap resonator with one pin row (marked with a red circle) between the ridge and the transition, d) ridge gap resonator with two pin rows (marked with a red circle) between the ridge and the transition.

Due to the issues mentioned in Paper I, when connecting to the ridge gap waveguide for 280 GHz , a new connection needed to be designed. In [100], a new transition from microstrip-to-ridge gap waveguide was presented, Fig. 4.38.

This connection allows coupling to the ridge gap waveguide with probes. The ridge gap waveguide is flipped upside down and placed above the transition patch on the PCB (Printed Circuit Board) substrate, Fig. 4.39.

Measurements were performed on the ridge gap resonators, however only the resonator with one pin row between the transition and the ridge showed a measurable resonance peak. Since the simulated and measured peaks were around -35 dB and -45 dB respectively, one can approximate the unloaded Q -value to be the loaded Q -value due to the low S_{21} values, see section 3.5. This measurement is compared to simulations in Fig. 4.40. Simulated and measured Q s together with corresponding resonance frequencies can be seen in Tab. 4.9.

At that time, no measurement results could be obtained from the 100 GHz ridge gap waveguides, due to misalignments with the PCB. A study was later performed about the tolerances for this transition in [101].

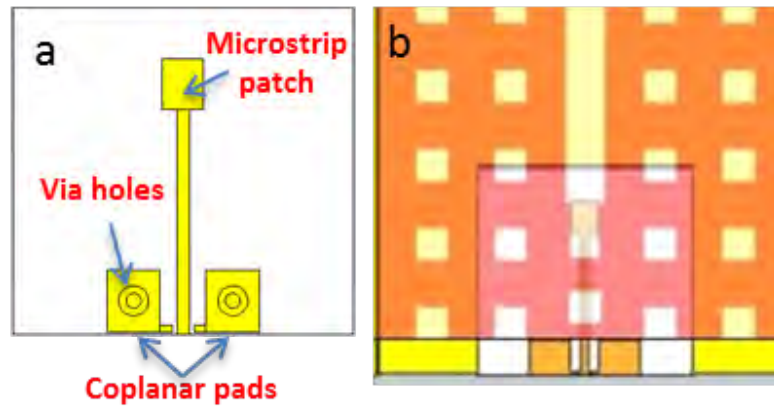


Figure 4.38: a) The microstrip transition and b) how the ridge will overlap the transition when being flipped on top of it.

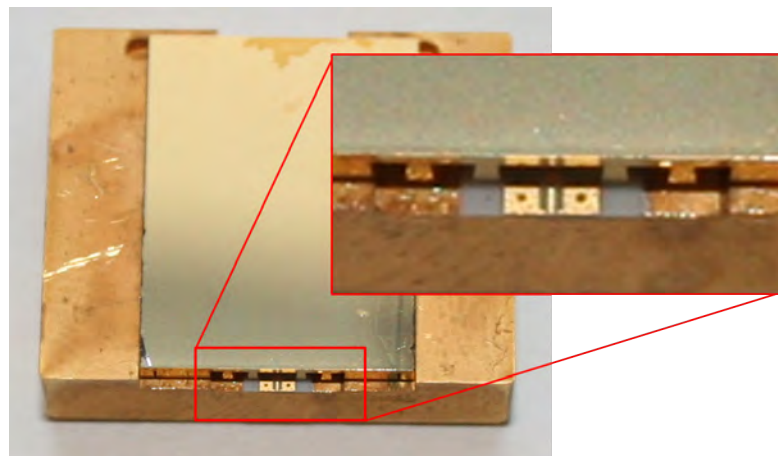


Figure 4.39: View of the microstrip-to-ridge gap waveguide transition. The chip is flipped upside down, facing the microstripline. The visual part of the microstripline is where the contact probes will connect.

Table 4.9: Simulated and measured Q_s for the ridge gap resonator

	Simulated	Measured
Resonance frequency	108.9 GHz	107.3 GHz
Loaded Q-value	1168	755
Loss (dB/λ)	0.023	0.036

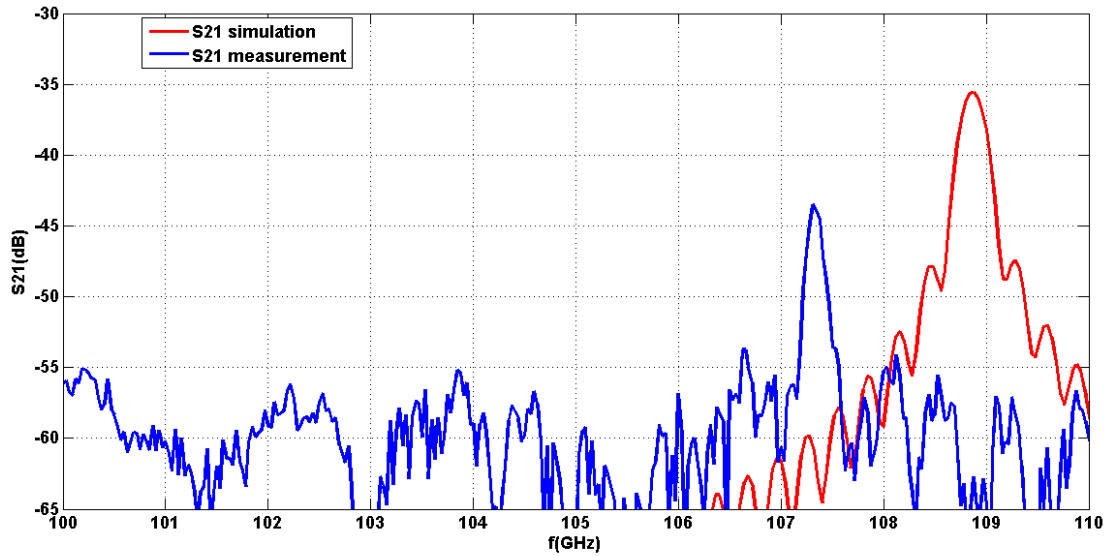


Figure 4.40: Computed and measured S-parameters of the ridge gap resonator with the microstrip-to-ridge gap waveguide transitions.

4.3.3 Discussion

The high aspect ratio of the pins for all devices was an issue and complicates the DRIE process, as discussed in section 2.2.1. A way to avoid this is to either design the gap waveguide devices to have wider pins, or to use another fabrication process, where this is not an issue, like the SU8 process.

The groove gap waveguide was easy to connect to because it does not need any transition structure. The ridge gap waveguide was able to connect via probes through the new transition structure and it is the first of several future ways to connect to a ridge gap waveguide device.

The return loss from the measurement of the straight and 90° bend groove gap waveguides are good, $S_{21} < -10$ dB for the straight waveguide and $S_{21} < -15$ dB for the waveguide with two 90° bends, but not as good as the simulations for the groove gap waveguide. One reason could be that the groove gap waveguides are designed for F-band (90 – 140 GHz) but they were measured with W-band (75 – 110 GHz) flanges thus there is some mismatch between the two waveguide openings. Another reason could be the surface roughness of the bottom of the grooves, see Fig. 4.33. The reason to why they look so rough is that although an SOI wafer was used, the wafer was etched so differently in the center of the wafer compared to the edges that before the center structures had reached the SiO_2 , the outer structures had already reached the SiO_2 , and

the pins of the groove gap structures on the edges were starting to get cut-off from the under etch. The etch process was therefore stopped when only half of the structures had reached the SiO_2 , to protect the pins. Therefore the groove gap structures that survived the process does not have a complete SiO_2 bottom, and therefore the surface in the bottom is so rough. The ridge gap waveguide devices have less roughness due to the pins' close proximity to each other, which results in less under etch. Also, the bottom surface roughness for a ridge gap waveguide is not as important as for the groove gap waveguide since the wave propagate on top of the ridge instead of the bottom of the structure.

The initial measurements on the ridge gap resonator shows that the transition works, however it is still a bit lossy. This could be due to the uncertainty of the alignment of the PCB to the ridge gap waveguide, this was the reason to why no measurements could be done on the straight and 90° bend ridge gap waveguide. The PCB can be misaligned both laterally and vertically but also there could be an angular misalignment. A better way of fixating the chip to the PCB is needed, right now the PCB is placed by hand and aligned via alignment marks. The misalignment sensitivity was later explored in [101].

The calculated attenuation per wavelength from the ridge and groove gap resonators is presented in Tab. 4.10, together with the attenuation loss of a commercial straight waveguide, a micromachined Si rectangular waveguide and a diamond milled brass waveguide. The approximated attenuation from the resonators are comparable to the standard WR10 waveguide measured in [102] and better than the silicon-based rectangular waveguide also presented in [102], but not as good as the recently presented brass diamond drilled waveguide [103].

Table 4.10: Attenuation calculated from the unloaded Q-values of the groove and ridge gap resonator, together with values from existing technology

	Frequency	Attenuation per wavelength
Groove gap resonator	95.64 GHz	0.022 dB
	115.60 GHz	0.024 dB
Ridge gap resonator	107.3 GHz	0.036 dB
Micromachined Si straight WR10 Waveguide with Au coating. [102]	100 GHz	0.04 dB
Commercial straight WR10 waveguide. [102]	100 GHz	0.024 dB
Diamond drilled brass WR10 Waveguide 2015. [103]	100 GHz	0.015 dB

4.4 H-bend Rectangular Waveguide-to-Microstrip Transition

As mentioned in section 1.3, there are many benefits having a rectangular waveguide-to-microstrip transition, and many ways to achieve them. In Paper IV, a ridge gap waveguide to coplanar waveguide transition was presented. In Paper VIII, another transition is explored, a rectangular waveguide-to-microstrip transition operating at 140 – 220 GHz. The transition was fabricated in Si by using DRIE. At the same time a similar hollow structures was fabricated with the same process. The so called hollow waveguide was used to test the quality of the fabrication method.

The rectangular waveguide is connected to the transition, the wave propagates inside the rectangular cavity until it reaches the MMIC probe in the center. The signal is transferred from the cavity to the probe, and then through the probe to the other waveguide cavity. If there was no probe, then there would be no transmission. Therefore, to evaluate the H-plane bend rectangular waveguide-to-microstrip transition, a hollow waveguide was also fabricated with the same process.

The cross-section of the rectangular waveguide-to-microstrip and the hollow waveguide are presented in Fig. 4.41. Both structures can be fabricated in the same batch since they both have four etch steps with the same desired depths: 70 μm , 283 μm , 283 μm and 364 μm .

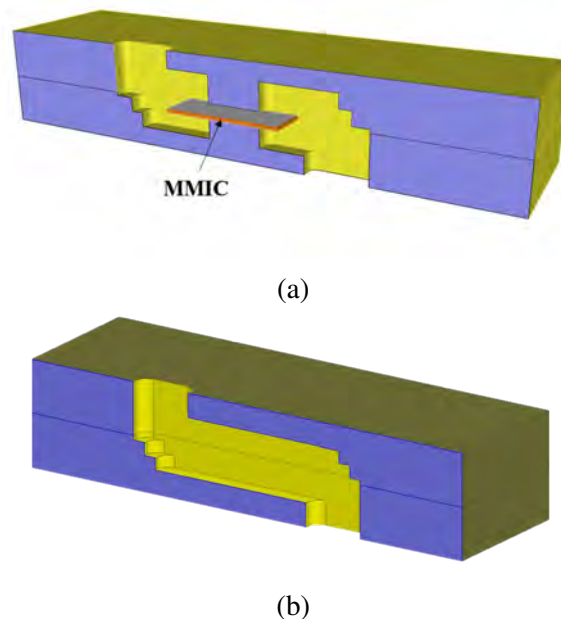


Figure 4.41: Cross-section of (a) the rectangular waveguide-to-microstrip transition and (b) the hollow waveguide.

The structures in Fig. 4.41 are made in mirror halves, cut in the H-plane. Each half is placed inside the package, which is then closed with the halves inside. The package is designed so that standard rectangular waveguide flanges can be connected to each side of the package, Fig. 4.42.

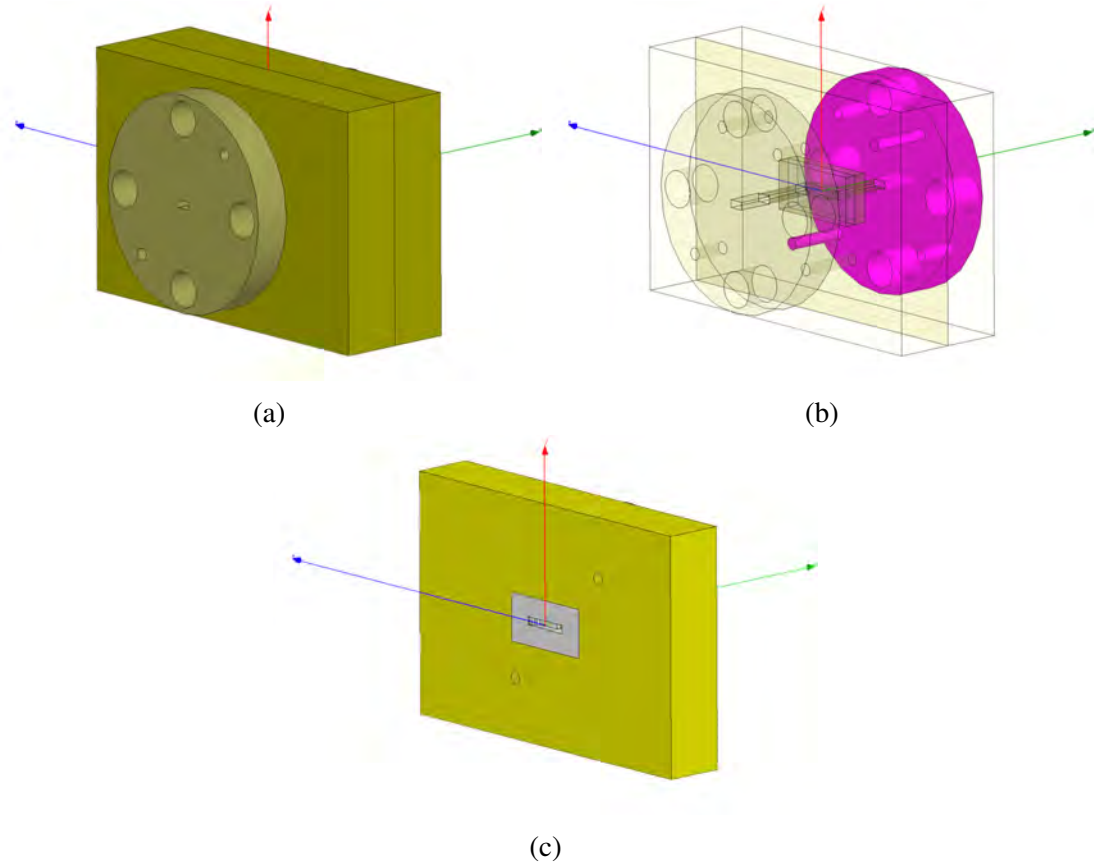


Figure 4.42: (a) Schematic image of the package from the outside. (b) Transparent view of the package with the rectangular waveguide-to-microstrip transition halves inside. (c) View of one of the package halves from the inside with one side of the rectangular waveguide-to-microstrip transition halves inside of it.

One of the difficulties with this design is that four etch masks, with high selectivity to each other and to Si are needed. The process presented in Fig. 4.43 have the following etch masks (in order): SiO_2 , Al, AZ4562 photoresist and another Al layer. Another difficulty is to etch these deep levels without too much under etch, or too much movement of the side walls. Two processes were run, one with the ICP STS plasma machine (section 2.2.2) and the other with the Centura II (DPS & MxP) (section 2.2.3).

4.4. H-BEND RECTANGULAR WAVEGUIDE-TO-MICROSTRIP TRANSITION 79

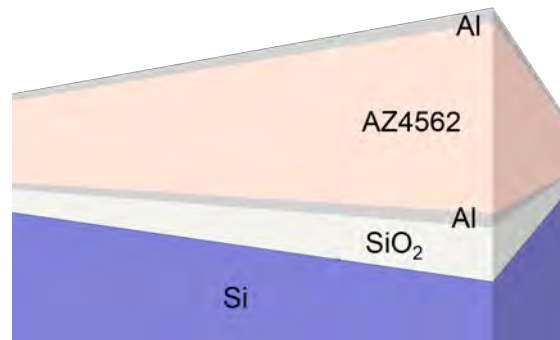


Figure 4.43: Close-up of the four etch masks used during the four step etch process.

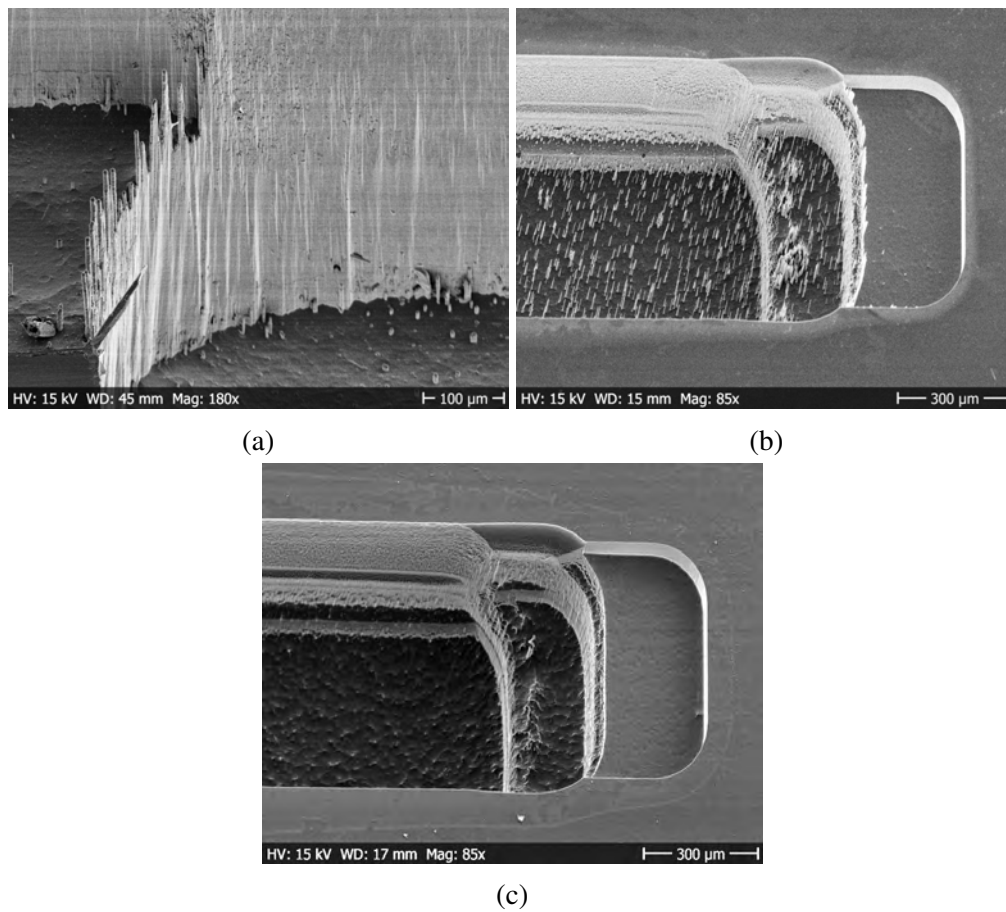


Figure 4.44: (a) Spikes that occurred at the edges of the steps after the ICP STS plasma process. (b) Grassing that occurred after the Centura process. (c) The grassing removed after the SF₆ plasma etch.

In Paper VIII, the processes were evaluated on three properties: 1) how much under etch the steps have, 2) how much the widths of the openings deviate from the mask design, and 3) the surface roughness. It was concluded that the process with the STS ICP plasma machine gave lower surface roughness ($rms > 0.19 \mu m$) but a large under etch, and the Centura II (DPS & MxP) process had almost no under etch at the price of a high surface roughness ($rms > 0.23 \mu m$ measured after the isotropic SF6 plasma etch). Both processes showed comparable behaviour when it comes to the movement of the side walls, and both processes suffered from high ratio spikes in the trenches and on the edges, Fig. 4.44. This is due to re-sputtering of the Al mask into the trenches, and misalignments between etch masks. This was solved by exposing the structure to a 6 min isotropic SF6 plasma etch, which removed the grassing, Fig. 4.44c. The effect of this was measured on what was a 50 μm wide line prior to the isotropic SF6 etch. After measuring on 28 lines, it was concluded that the lines had expanded with $11.43 \pm 1.90 \mu m$ in total.

A measurement was performed on a hollow waveguide that was fabricated with the Centura process and exposed to the 6 min isotropic plasma etch. The measurement presented in Fig. 4.45, shows an insertion loss of around 1.5 dB up to 210 GHz and a return loss below -10 dB between 148 – 214 GHz.

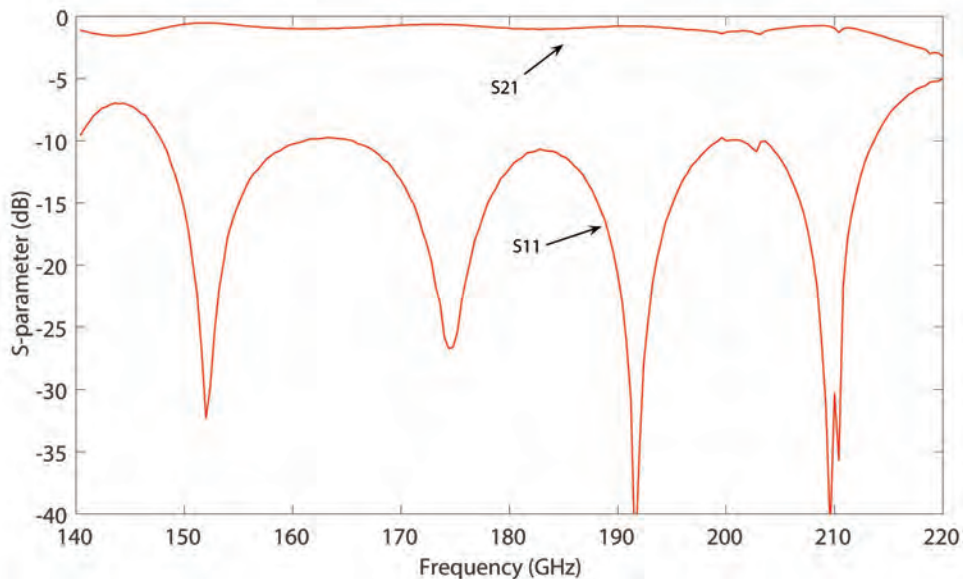


Figure 4.45: Measured S_{21} and S_{11} of the hollow waveguide.

4.4.1 Discussion

The measurement on the hollow waveguide showed that there was transmission from one side to the other. However, the insertion loss and return loss are higher than expected $S_{21} \sim 1.5 \text{ dB}$ and $S_{11} < -10 \text{ dB}$ compared to simulated $S_{21} \sim 0 \text{ dB}$ and $S_{11} < -20 \text{ dB}$. The high insertion loss could be due to that the surface roughness is larger than the skin depth for Au at these frequencies ($0.17 - 0.21 \mu\text{m}$), thus adding to the propagation path and increasing the insertion loss. Also, the measurement was measured from waveguide port to waveguide port, so there are many places in between the ports that could create losses. First, the connection from the rectangular waveguide flange to the package, where it has been concluded from section 4.2 that this is quite sensitive to gaps and misalignments. Second, the hollow waveguide half is not soldered to the inside of the package, therefore, there could be leakage between the package and the hollow waveguide half. Third, the two hollow waveguide halves are not bonded to each other, maybe allowing leakage to occur between the plates.

One way to avoid leakage between the rectangular waveguide flange and the package is to use a gap adapter as in section 4.2. The leakage between the package and the hollow waveguide halves could be avoided if the pin and screw holes were incorporated in the hollow waveguide half chip, like they are in the gap adapter designs (section 4.2). To avoid any potential leakage between the hollow waveguide halves themselves, one can on one of the halves incorporate an AMC surface (as mentioned in section 3.2) facing the other half, thus creating a stop band between the two halves even if they are not in full contact. Another way is to bond the two halves together with for example eutectic Au bonding.

To avoid complications with several selective etch masks, re-sputtering, and having to choose between little under etch or low surface roughness, SU8 can be used as a structural material instead. SU8 can create structures up to 2 mm , complete vertical walls, and it has a smooth surface. The downside with SU8 is the long baking times needed for the thick layers needed in this structure.

4.5 100 GHz Ridge Gap Waveguide Antenna

After exploring the many possibilities of gap waveguide transmission lines and different kinds of waveguide-to-microstrip transitions, the next step is to use this knowledge to work with antennas. In Paper IX, the first gap waveguide antenna operating above 100 GHz was fabricated with microfabrication.

The gap waveguide antenna was based on a design made for the frequency range $12 - 15 \text{ GHz}$ [65], the rectangular waveguide-to-ridge transition, however, has been modified. The gap waveguide antenna consists of two plates: the bottom plate with the rectangular waveguide-to-ridge transition (Fig. 4.46a) and the ridge gap waveguide feed

network, and the top plate with the gap incorporated with spacers. The top plate also has four radiating slots (Fig. 4.46b).

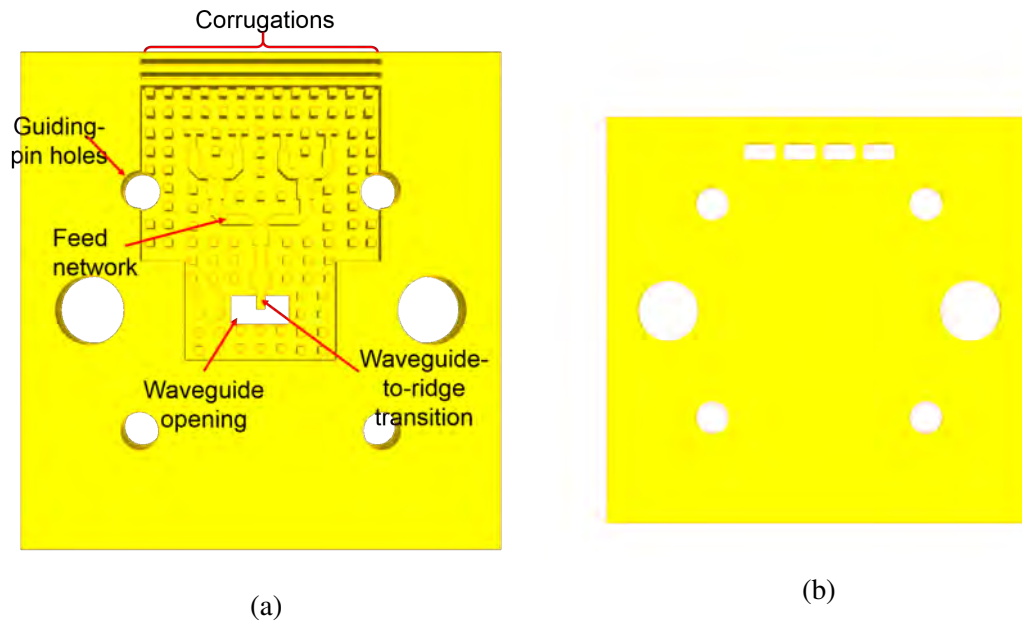


Figure 4.46: a) The bottom plate, displaying the feed network, and the screw and guiding pin holes. b) The top plate, displaying the four radiation slots, and the screw and guiding pin holes.

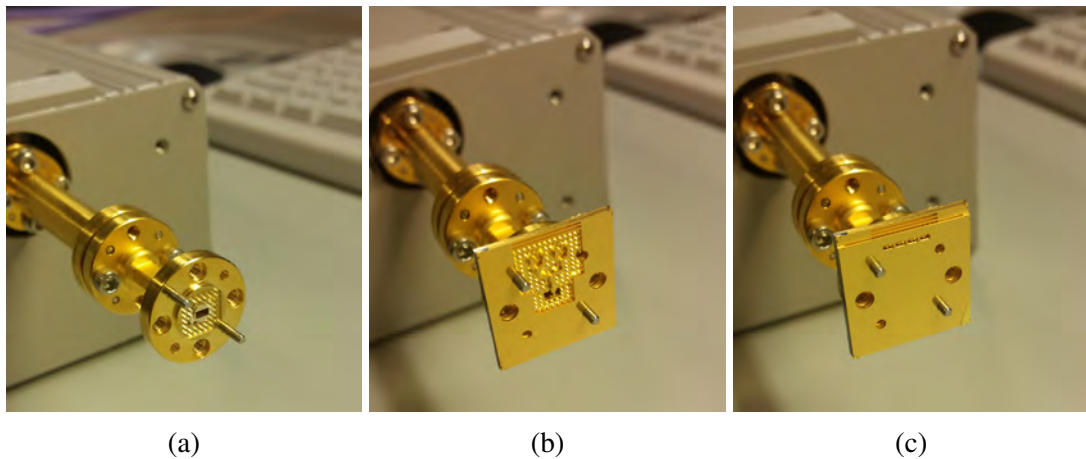


Figure 4.47: a) The waveguide flange with the pin surface around it [99], Paper II and V. b) The gap waveguide feed network fitted onto the guiding pins of the waveguide flange. c) The lid with the radiating slots.

To avoid problems with package alignments, as those mentioned in sections 4.1 and 4.4, the gap waveguide antenna was designed similar to the gap adapter (section 4.2) with holes for the guiding pins and screws, etched in the Si, Fig. 4.47b. To avoid exposing the Si antenna to uneven forces and risk cracking the Si, a rectangular waveguide flange with a pin surface similar to the one on the gap adapter was used to couple to the antenna, Fig. 4.47a. This way, the two gap waveguide plates can just be slid on (Fig. 4.47), and no screws were needed to fixate them (see section 4.2).

To fabricate the overhang that makes up the rectangular waveguide-to-ridge transition, an SOI wafer as the one presented in section 4.3 was used. The feed network was etched with DRIE from the top of the wafer, and the rectangular waveguide opening was etched with DRIE from the back of the wafer. The SiO_2 in the rectangular waveguide opening was etched with plasma etch from the back side of the wafer to open up the transition, and still leave the ridge overhang intact, Fig 4.48.

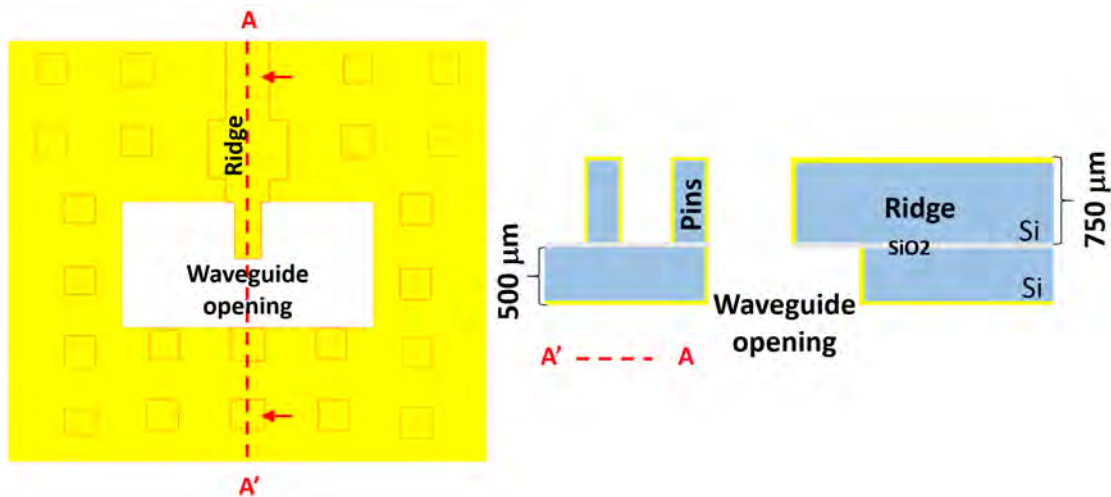


Figure 4.48: Close-up of the rectangular waveguide-to-ridge transition, together with a cross-section.

The return loss of the antenna was measured and is presented in Fig. 4.49. The antenna bandwidth was measured to be 15.5% ($S_{11} < -10$ dB between 92.6 – 108.2 GHz) compared to the simulated bandwidth of 18%.

The measured and simulated gain are presented in Fig. 4.50, where the measurement point at 100 GHz shows a gain of 10.4 dBi, the average gain calculated from the measurement points between 99.6 – 100.4 GHz was 10.3 dBi. Both values are close to the simulated value of 10.5 dBi at 100 GHz.

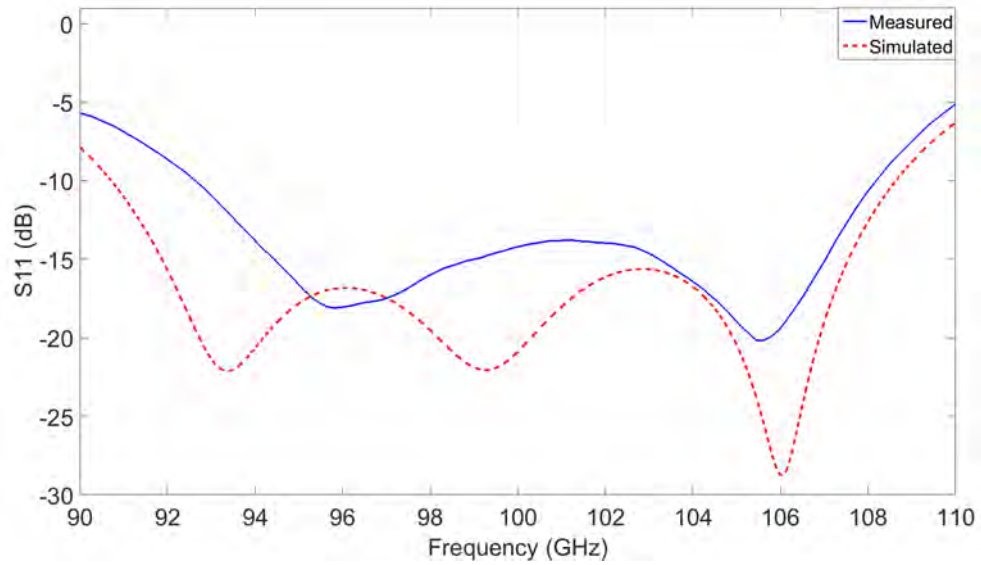


Figure 4.49: Measured (solid blue) and simulated (dashed red) input reflection coefficient S_{11} at the WR10 port.

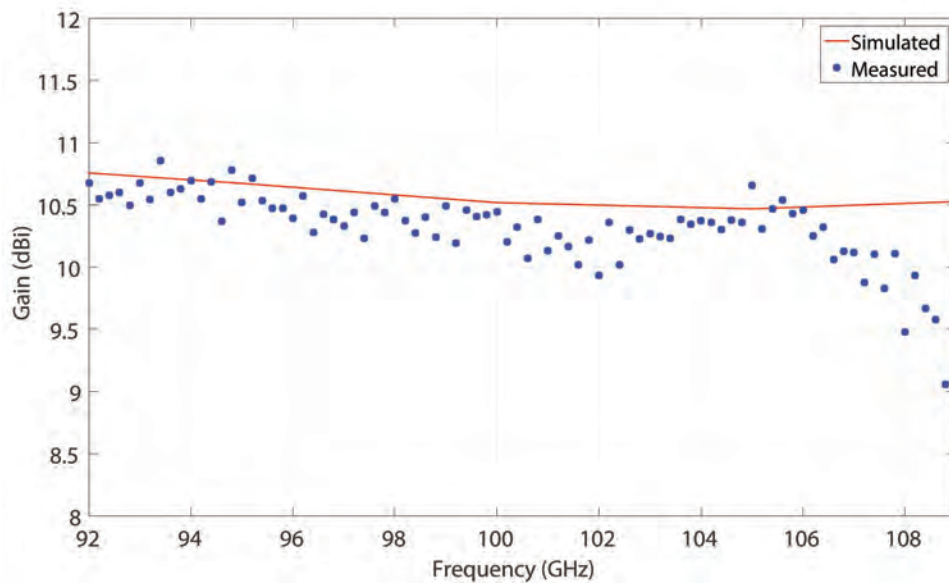


Figure 4.50: Simulated and measured gain.

4.5.1 Discussion

The gap waveguide antenna presented in Paper IX is a good example of how all of the knowledge from the previous papers could be used into making a complete device. The rectangular waveguide-to-ridge coupling was an issue that already appeared in Paper I, and it was further investigated in Paper IV and iterated until the transition in Paper IX was presented. The idea of removing the package and incorporating the pin and screw holes in the Si was inspired from Papers II and VII, and to use a gap adapter to avoid screws when coupling to the antenna came from the conclusions in Paper VII. The knowledge about how to take advantage of an SOI wafer came from the work presented in Papers III and IV.

The return loss presented in Fig. 4.49, shows a wide-band antenna. The good match between the simulated and measured return loss also shows a well matched coupling between the waveguide port and the antenna. This shows how well the gap adapter works without screws.

The measured gain was also close to the simulated gain, thus indicating that the gold-covered Si gap waveguide antenna was fabricated well to the standards of the design given.

Conclusion

In this thesis, gap waveguides from 100 – 325 GHz, gap adapters, a rectangular waveguide-to-microstrip transition and a gap waveguide antenna were all microfabricated with base materials covered in gold. The three base materials explored in this thesis are silicon, SU8 and carbon nanotubes.

Silicon is the most common material used for these kind of structures, there are several processes developed to work with silicon at the microscale, and high resolution structures can be achieved. Due to the large structures and high aspect ratios needed at these frequencies, there were some difficulties that occurred. The first issue that occurred was the strong under-etch of the pins, for every design, the deep reactive ion etch process needed to be tuned to balance the under-etch and surface roughness. Also, when etching deep trenches of several hundred micrometers with multiple etch masks, there is also the issue of finding etch masks that have a high selectivity to each other and to silicon. For smaller structures, it would be easier to find etch masks that are selective to each other and would still survive the process.

SOI (silicon on insulator) wafers are another way to work with silicon structures, the oxide layer is used as a stop-layer to achieve a uniform pin height throughout the wafer. The downside when working with a large wafer, in this case a 6" wafer, is that there will be a difference in etch rate. The outer perimeter of the wafer will etch faster than the center of the wafer. The deeper the etch, the bigger is the difference of etch depths. This resulted in that the oxide on the outer edge of the wafer had almost been completely etched away, while in the center of the wafer, the oxide was barely visible, thereby defeating the purpose of achieving a uniform pin-height over the entire wafer.

A material that is gaining popularity for high frequency applications is the polymer SU8. The benefit is that no etch masks are needed, layers up to 650 μm can be spun in one run, all structures are vertical, there is no "under-etch", the material is fairly robust (the SU8 gap adapter survived a fall of 5 m), and relatively low cost considering both the equipment and the material cost. The downside with fabricating large structures in SU8

is the long curing times, the thicker the SU8 the longer the curing times, up to several hours. Another issue that was noticed in the presented work was that the adhesion of Au to SU8 after gold-plating was sensitive during cooling for large smooth surface areas. The electroplating process needed to be optimized depending on the SU8 structure, and the electroplated SU8 structure needed to be cooled gradually.

Carbon nanotubes were explored for the first time to be used as a base material. Carbon nanotubes can grow several hundreds of micrometers within minutes and the process cost less than the silicon deep reactive ion etch process. However, it is difficult to grow the carbon nanotubes with high precision and they are difficult to cover with a conductive metal. The top surface roughness is also quite high thus creating a lossy surface. This could be avoided by implementing the design of a groove gap waveguide instead. The wave would propagate on the silicon surface with a lower surface roughness instead.

When the three base materials were compared to each other by fabricating the 280 GHz ridge gap resonator, the silicon ridge gap resonator performed the best overall, however the SU8 ridge gap resonator performed the best for higher frequencies. The CNTs proved to be the lossiest of the base materials.

The gap adapter evolved from a single-sided brass prototype to a double-sided SU8 gap adapter. The gap adapter enables measurements without screws or perfect electrical connection. It was shown that the gap adapter could operate with gaps up to 100 μm , compared to a flat surface reference, that had an insertion loss of 1.5 dB as soon as the screws were removed. By fabricating the gap adapter with SU8, the gap adapter is made robust, easy to mass-fabricate and at a low cost.

Groove and ridge gap waveguides were further explored at 100 GHz with different ways of connecting to them. The groove, being similar to the rectangular waveguide, did not need any transition structure, while the ridge needed a rectangular waveguide-to-ridge transition. Both structures were more lossy than expected, although they showed comparable attenuation per wavelength to existing technology.

A rectangular waveguide-to-microstrip transition was also fabricated in silicon, together with a hollow waveguide version. Two different deep reactive ion etch processes were explored, both showed a trade off between low under etch and low surface roughness. Measurements on the hollow waveguide showed an insertion loss of around 1.5 dB and a return loss of 10 dB, which is higher than simulated. This could be due to the surface roughness, or the way it is packaged. If the transitions and the hollow waveguide were to be fabricated in SU8 instead, there would not be any under etch and the surface roughness would be much smoother, although the curing times would be very long.

The 100 GHz ridge gap antenna uses the same kind of silicon on insulator wafers as the 100 GHz gap waveguides. The benefit of the silicon on insulator wafer is that it makes it possible to create an overhang for the rectangular waveguide-to-ridge transition. This would not be possible if only SU8 was used. The design has guiding pin and

screw holes etched in the silicon. It uses a gap adapter to connect to it, to avoid screws and any pressure that could risk damaging the silicon. Like for the silicon gap adapter, the measurements showed a strong agreement with the simulations, indicating that the fabrication process was successful. The fabrication process was even more successful than the process used for the 100 *GHz* groove and ridge gap waveguides. Although the measurements matched the simulations, the performance is not competitive with existing technology, as the antenna was designed as a proof-of-concept prototype. However, since the microfabrication process was so successful in fabricating the antenna at the specifications given, there is good reason to believe that it will work for a design with competitive performance.

The work presented in this thesis shows how microsystem technology enables the realisation of microwave components above 100 *GHz*. The thesis explored the fundamentals needed to in the end fabricate a high frequency antenna, and the work done here opens up the possibility for high frequency passive and active components with transitions in between.

Outlook

The work presented in this thesis explores the fundamental components and transitions for frequencies above 100 GHz. A proof-of-concept antenna operating at 100 GHz was presented with a gain of 10.4 dBi and a bandwidth of 15.5%. Although the antenna performed according to simulations, the antenna is not commercially competitive. The next step would be to design and fabricate high gain, wide-band planar gap waveguide antennas operating at 140 GHz. The biggest challenge with these gap waveguide antennas are that they are going to have several layers just as previous gap waveguide antennas at 60 GHz have [68, 72, 73, 104]. This requires a good alignment and high precision. The material also needs to be able to produce high aspect ratio structures.

In this thesis, gold-covered silicon and SU8 have been used for these kind of large and high aspect ratio electromagnetic structures. Another material that would be interesting to investigate is the polymer OSTE (Off-stoichiometry thiol-ene). Like SU8, OSTE is a UV-sensitive polymer, and can be used to fabricate high aspect ratio structures. However, unlike SU8, OSTE does not need as long curing times as SU8 do and can instead be cured with UV light within minutes. OSTE can be used for molding and contains sulfur, which enables direct covalent bonding to gold.

Another interesting path to explore is the field of active devices. With active devices, the high-frequency gap waveguide antennas can be made steerable and thus become active gap waveguide antennas. One way of making the gap antenna steerable is to use MMICs on the different branches of the feed network, to manipulate the signal. To make this possible, gap waveguide to MMIC coupling at high frequencies (above 100 GHz) needs to be investigated. Another way of making the gap antenna steerable is to incorporate gap waveguide switches on the feed network. Hence, an investigation of gap waveguide switches operating at higher frequencies (above 100 GHz) can be of interest.

Bibliography

- [1] D. M Pozar, “Microwave Engineering, 3rd,” *JOHN WILEY SONS INC*, 2005.
- [2] J. Hasch, E. Topak, R. Schnabel, T. Zwick, R. Weigel, and C. Waldschmidt, “Millimeter-wave technology for automotive radar sensors in the 77 GHz frequency band,” *IEEE Transactions on Microwave Theory and Techniques*, vol. 60, no. 3 PART 2, pp. 845–860, 2012.
- [3] N. Kukutsu, A. Hirata, M. Yaita, K. Ajito, H. Takahashi, T. Kosugi, H.-J. Song, A. Wakatsuki, Y. Muramoto, T. Nagatsuma, and Y. Kado, “Toward practical applications over 100 GHz,” in *Microwave Symposium Digest (MTT), 2010 IEEE MTT-S International*, (Anaheim, CA), pp. 1134–1137, 2010.
- [4] L. Yujiri, M. Shoucri, and P. Moffa, “Passive millimeter-wave imaging,” *IEEE Microwave Magazine*, vol. 4, pp. 39–50, sep 2003.
- [5] D. M. Sheen, D. L. McMakin, and T. E. Hall, “Three-dimensional millimeter-wave imaging for concealed weapon detection,” *IEEE Transactions on Microwave Theory and Techniques*, vol. 49, no. 9, pp. 1581–1592, 2001.
- [6] S. S. Ahmed, A. Genghammer, A. Schiessl, and L.-P. Schmidt, “Fully Electronic E-Band Personnel Imager of 2 m² Aperture Based on a Multistatic Architecture,” *IEEE Transactions on Microwave Theory and Techniques*, vol. 61, pp. 651–657, jan 2013.
- [7] N. D’Apuzzo, “Recent Advances in 3D Full Body Scanning With Applications To Fashion and Apparel,” *Optical 3-D Measurement Techniques IX, Vienna, Austria*, vol. 2, pp. 1–10, 2009.
- [8] M. Patlak, S. J. Nass, I. C. Henderson, and J. C. Lashof, *Mammography and Beyond: Developing Technologies for the Early Detection of Breast Cancer*. National Academies Press (US), 2001.

- [9] S. Hagness, A. Taflove, and J. Bridges, "Two-dimensional FDTD analysis of a pulsed microwave confocal system for breast cancer detection: fixed-focus and antenna-array sensors," *IEEE Transactions on Biomedical Engineering*, vol. 45, no. 12, pp. 1470–1479, 1998.
- [10] M. Stuchly and E. Fear, "Microwave detection of breast cancer," *IEEE Transactions on Microwave Theory and Techniques*, vol. 48, no. 11, pp. 1854–1863, 2000.
- [11] F. Töpfer and J. Oberhammer, "Millimeter-Wave Tissue Diagnosis: The Most Promising Fields for Medical Applications," *IEEE Microwave Magazine*, vol. 16, pp. 97–113, may 2015.
- [12] F. Töpfer, S. Dudorov, and J. Oberhammer, "Micromachined 100 GHz near-field measurement probe for high-resolution microwave skin-cancer diagnosis," in *2012 IEEE/MTT-S International Microwave Symposium Digest*, pp. 1–3, IEEE, jun 2012.
- [13] G. M. Rebeiz, *RF MEMS: Theory, Design, and Technology*. John Wiley & Sons, 2003.
- [14] L. Larson, R. Hackett, M. Melendes, and R. Lohr, "Micromachined microwave actuator (MIMAC) technology—a new tuning approach for microwave integrated circuits," *IEEE 1991 Microwave and Millimeter-Wave Monolithic Circuits Symposium. Digest of Papers*, 1991.
- [15] N. Somjit, G. Stemme, and J. Oberhammer, "Binary-Coded 4.25-bit W-Band Monocrystalline-Silicon MEMS Multistage Dielectric-Block Phase Shifters," *Microwave Theory and Techniques, IEEE Transactions on*, vol. 57, no. 11, pp. 2834–2840, 2009.
- [16] C. Goldsmith, A. Malczewski, Z. Yao, S. Chen, J. Ehmke, and D. Hinzl, "RF MEMS variable capacitors for tunable filters," *International Journal of RF and Microwave Computer-Aided Engineering*, vol. 9, no. 4, pp. 362–374, 1999.
- [17] E. Erdil, K. Topalli, M. Unlu, O. Civi, and T. Akin, "Frequency Tunable Microstrip Patch Antenna Using RF MEMS Technology," *IEEE Transactions on Antennas and Propagation*, vol. 55, no. 4, pp. 1193–1196, 2007.
- [18] K. E. Petersen, "Micromechanical Membrane Switches on Silicon," *IBM Journal of Research and Development*, vol. 23, no. 4, pp. 376–385, 1979.
- [19] K. Petersen, "Dynamic micromechanics on silicon: Techniques and devices," *IEEE Transactions on Electron Devices*, vol. 25, 1978.

- [20] M.-A. Grétilat, F. Grétilat, and N. F. De Rooij, “Micromechanical relay with electrostatic actuation and metallic contacts,” *Journal of Micromechanics and Microengineering*, vol. 9, pp. 324–331, 1999.
- [21] J. Wright and Y.-C. Tai, “Magnetostatic MEMS relays for the miniaturization of brushless DC motor controllers,” in *Technical Digest. IEEE International MEMS 99 Conference. Twelfth IEEE International Conference on Micro Electro Mechanical Systems*, (Orlando Florida, USA), pp. 594–599, 1999.
- [22] H. Sehr, A. G. R. Evans, A. Brunnschweiler, G. J. Ensell, and C. G. J. Schabmueller, “Design and fabrication of a thermally actuated microrelay based on vertical bimorphs,” in *Eurosensors XVI, the 16th European Conference on Solid-State Transducers*, (Prague, Czech Republic), pp. 752–755, 2002.
- [23] H.-C. Lee, J.-Y. Park, and J.-U. Bu, “Piezoelectrically actuated RF MEMS DC contact switches with low voltage operation,” *IEEE Microwave and Wireless Components Letters*, vol. 15, no. 4, 2005.
- [24] Ai Qun Liu, *RF MEMS Switches and Integrated Switching Circuits*. Springer US, 2010.
- [25] S. Roy and M. Mehregany, “Fabrication of electrostatic nickel microrelays by nickel surface micromachining,” in *Proc. IEEE Int. Conf. Micro-electromechanical Systems*, (Amsterdam, Netherlands), pp. 353–357, 1995.
- [26] F. A. Ghavanini, P. Enoksson, S. Bengtsson, and P. Lundgren, “Vertically aligned carbon based varactors,” *Journal of Applied Physics*, vol. 110, no. 2, p. 021101, 2011.
- [27] A. Cazzorla, P. Farinelli, L. Urbani, R. Sorrentino, and B. Margesin, “MEMS-based LC tank with extended tuning range for multiband applications,” *Radio Science*, 2016.
- [28] J. Basu and T. K. Bhattacharyya, “Microelectromechanical resonators for radio frequency communication applications,” *Microsystem Technologies*, vol. 17, pp. 1557–1580, 2011.
- [29] Y. Lin, S. Lee, S. Li, Y. Xie, Z. Ren, and C. . Nguyen, “Series-resonant VHF micromechanical resonator reference oscillators,” 2004.
- [30] Y.-W. Lin, S. Lee, S.-S. Li, Y. Xie, Z. Ren, and C.-C. Nguyen, “60-MHz wine-glass micromechanical-disk reference oscillator,” *2004 IEEE International Solid-State Circuits Conference (IEEE Cat. No.04CH37519)*, 2004.

- [31] K. Cioffi and W.-T. Hsu, "32KHz MEMS-based oscillator for low-power applications," in *Proceedings of the 2005 IEEE International Frequency Control Symposium and Exposition, 2005.*, (Vancouver), pp. 551–558, 2005.
- [32] S.-S. Li, Y.-W. Lin, Y. Xie, Z. Ren, and C.-C. Nguyen, "Micromechanical "hollow-disk" ring resonators," *17th IEEE International Conference on Micro Electro Mechanical Systems. Maastricht MEMS 2004 Technical Digest*, 2004.
- [33] L. Pelliccia, P. Farinelli, R. Sorrentino, G. Cannone, G. Favre, and P. Coassini, "K-band MEMS-based frequency adjustable waveguide filters for mobile back-hauling," *International Journal of Microwave and Wireless Technologies*, vol. 8, pp. 751–757, apr 2016.
- [34] K. Boustedt, K. Persson, and D. Stranneby, "Flip chip as an enabler for MEMS packaging," in *Electronic Components and Technology Conference, 2002. Proceedings. 52nd*, pp. 124–128, 2002.
- [35] O. Heaviside, *Electromagnetic theory*. London: "The Electrician" printing and publishing company, limited, 1 ed., 1893.
- [36] L. Rayleigh, "XVIII. On the passage of electric waves through tubes, or the vibrations of dielectric cylinders," *Philosophical Magazine Series 5*, vol. 43, pp. 125–132, feb 1897.
- [37] D. D. Grieg and H. F. Engelmann, "Microstrip—A New Transmission Technique for the Kilomegacycle Range," *Proceedings of the IRE*, vol. 40, no. 12, pp. 1644–1650, 1952.
- [38] J. Hirokawa and M. Ando, "Single-layer feed waveguide consisting of posts for plane TEM wave excitation in parallel plates," *IEEE Transactions on Antennas and Propagation*, vol. 46, 1998.
- [39] K. Wu, D. Deslandes, and Y. Cassivi, "The substrate integrated circuits - a new concept for high-frequency electronics and optoelectronics," in *6th International Conference on Telecommunications in Modern Satellite Cable and Broadcasting Service 2003 TELSIKS 2003*, vol. 1, pp. P–III–P–X, 2003.
- [40] E. Yablonovitch, "Inhibited Spontaneous Emission in Solid-State Physics and Electronics," *Physical Review Letters*, vol. 58, no. 20, pp. 2059–2062, 1987.
- [41] S. John, "Strong Localization of Photons in Certain Disordered Dielectric Supperlattices," *Physical Review Letters*, vol. 58, no. 23, pp. 2486–2489, 1987.

- [42] P.-S. Kildal, E. Alfonso, A. Valero-Nogueira, and E. Rajo-Iglesias, "Local metamaterial-based waveguides in gaps between parallel metal plates," *IEEE Antennas and Wireless Propagation Letters (AWPL)*, vol. 8, pp. 84–87, 2009.
- [43] P.-S. Kildal, "Three metamaterial-based gap waveguides between parallel metal plates for mm/submm waves," in *3rd European Conference on Antennas and Propagation (EuCAP 2009)*, vol. 8, (Berlin, Germany), pp. 84–87, 2009.
- [44] P.-S. Kildal, A. U. Zaman, E. Rajo-Iglesias, E. Alfonso, and A. Valero-Nogueira, "Design and experimental verification of ridge gap waveguide in bed of nails for parallel plate mode suppression," *IET Microwaves, Antennas and Propagation*, vol. 5, no. 3, pp. 262–270, 2011.
- [45] E. Rajo-Iglesias, A. U. Zaman, and P.-S. Kildal, "Parallel plate cavity mode suppression in microstrip circuit packages using a lid of nails," *IEEE Microwave and Wireless Components Letters*, vol. 20, no. 1, pp. 31–33, 2009.
- [46] A. Algaba-Brazález, A. U. Zaman, and P.-S. Kildal, "Improved microstrip filters using PMC packaging by lid of nails," *IEEE Transactions on Components, Packaging and Manufacturing Technology*, vol. 2, no. 7, pp. 1075–1084, 2012.
- [47] A. U. Zaman, P.-S. Kildal, and A. A. Kishk, "Narrow-Band Microwave Filter Using High-Q Groove Gap Waveguide Resonators With Manufacturing Flexibility and No Sidewalls," *IEEE Transactions on Components, Packaging and Manufacturing Technology*, vol. 2, pp. 1882–1889, nov 2012.
- [48] A. U. Zaman, M. Alexanderson, T. Vukusic, and P.-S. Kildal, "Gap Waveguide PMC Packaging for Improved Isolation of Circuit Components in High-Frequency Microwave Modules," *IEEE Transactions on Components, Packaging and Manufacturing Technology*, vol. 4, no. 1, pp. 16 – 25, 2014.
- [49] H.-W. Yao, A. Abdelmonem, J.-F. Liang, and K. Zaki, "Analysis and design of microstrip-to-waveguide transitions," *IEEE Transactions on Microwave Theory and Techniques*, vol. 42, no. 12, pp. 2371–2380, 1994.
- [50] Y.-C. Shih, T.-N. Ton, and L. Bui, "Waveguide-to-microstrip transitions for millimeter-wave applications," in *1988., IEEE MTT-S International Microwave Symposium Digest*, pp. 473–475, IEEE, 1988.
- [51] Y.-C. Leong and S. Weinreb, "Full band waveguide-to-microstrip probe transitions," in *1999 IEEE MTT-S International Microwave Symposium Digest*, vol. 4, (Anaheim, CA), pp. 1435–1438, Ieee, 1999.

- [52] K. Sakakibara, M. Hirono, N. Kikuma, and H. Hirayama, "Broadband and planar microstrip-to-waveguide transitions in millimeter-wave band," in *2008 International Conference on Microwave and Millimeter Wave Technology*, vol. 3, pp. 1278–1281, IEEE, apr 2008.
- [53] W. Simon, M. Werthen, and I. Wolff, "A novel coplanar transmission line to rectangular waveguide transition," *1998 IEEE MTT-S International Microwave Symposium Digest (Cat. No.98CH36192)*, vol. 1, pp. 3–6, 1998.
- [54] M. Al Henawy and M. Schneider, "Rectangular waveguide to coplanar stripline transition based on a unilateral finline," in *2012 6th European Conference on Antennas and Propagation (EUCAP)*, pp. 405–409, IEEE, mar 2012.
- [55] N. Kaneda, "A broad-band microstrip-to-waveguide transition using quasi-yagi antenna," *IEEE Transactions on Microwave Theory and Techniques*, vol. 47, no. 12, pp. 2562–2567, 1999.
- [56] J. Becker, Y. Lee, J. East, and L. Katehi, "A finite ground coplanar line-to-silicon micromachined waveguide transition," *IEEE Transactions on Microwave Theory and Techniques*, vol. 49, no. 10, pp. 1671–1676, 2001.
- [57] M. Vahidpour and K. Sarabandi, "2.5D Micromachined 240 GHz Cavity-Backed Coplanar Waveguide to Rectangular Waveguide Transition," *IEEE Transactions on Terahertz Science and Technology*, vol. 2, pp. 315–322, may 2012.
- [58] P.-S. Kildal, *Foundations of Antenna Engineering: A Unified Approach for Line-of-Sight and Multipath*. Gothenburg: Kildal Antenn AB, 2nd ed., 2015.
- [59] R. Garg, P. Bhartia, I. Bahl, and A. Ittipiboon, *Microstrip antenna design handbook*. Norwood, MA: ARTECH HOUSE INC, 2001.
- [60] J. Hirokawa and M. Ando, "Efficiency of 76 GHz Post-Wall Waveguide-Fed Parallel Plate Slot Arrays," in *29th European Microwave Conference, 1999*, vol. 3, pp. 271–274, IEEE, oct 1999.
- [61] L. Yan, W. Hong, G. Hua, J. Chen, K. Wu, and T. J. Cui, "Simulation and experiment on SIW slot array antennas," *IEEE Microwave and Wireless Components Letters*, vol. 14, no. 9, pp. 446–448, 2004.
- [62] J. Liu, D. R. Jackson, and Y. Long, "Substrate integrated waveguide (SIW) leaky-wave antenna with transverse slots," *IEEE Transactions on Antennas and Propagation*, vol. 60, no. 1, pp. 20–29, 2012.

- [63] F. Xu, K. Wu, and X. Zhang, "Periodic Leaky-Wave Antenna for Millimeter Wave Applications Based on Substrate Integrated Waveguide," *IEEE Transactions on Antennas and Propagation*, vol. 58, pp. 340–347, feb 2010.
- [64] Y. J. Cheng, W. Hong, and K. Wu, "Design of a Monopulse Antenna Using a Dual V-Type Linearly Tapered Slot Antenna (DVL TSA)," *IEEE Transactions on Antennas and Propagation*, vol. 56, pp. 2903–2909, sep 2008.
- [65] A. U. Zaman and P.-S. Kildal, "Wide-Band Slot Antenna Arrays With Single-Layer Corporate-Feed Network in Ridge Gap Waveguide Technology," *IEEE Transactions on Antennas and Propagation*, vol. 62, no. 6, pp. 2992–3001, 2014.
- [66] S. A. Razavi, P.-S. Kildal, L. Xiang, E. Alfonso Alós, and H. Chen, "2x2-Slot Element for 60-GHz Planar Array Antenna Realized on Two Doubled-Sided PCBs Using SIW Cavity and EBG-Type Soft Surface fed by Microstrip-Ridge Gap Waveguide," *IEEE Transactions on Antennas and Propagation*, vol. 62, pp. 4564–4573, sep 2014.
- [67] B. Cao, H. Wang, Y. Huang, and J. Zheng, "High-Gain L-Probe Excited Substrate Integrated Cavity Antenna Array with LTCC-Based Gap Waveguide Feeding Network for W-Band Application," *IEEE Transactions on Antennas and Propagation*, vol. 63, pp. 5465–5474, dec 2015.
- [68] A. U. Zaman and P.-S. Kildal, "Different Gap Waveguide Slot Array Configurations for mmWave Fixed Beam Antenna Application," in *2016 10th European Conference on Antennas and Propagation (EuCAP)*, pp. 1–4, IEEE, apr 2016.
- [69] M. Ferrando-Rocher, A. Valero-Nogueira, J. I. Herranz-Herruzo, A. Berenguer, and B. Bernardo-Clemente, "Groove Gap Waveguides : A Contactless Solution for Multilayer Slotted-Waveguide Array Antenna Assembly," in *2016 10th European Conference on Antennas and Propagation (EuCAP)*, (Davos), pp. 1–4, IEEE, apr 2016.
- [70] A. Farahbakhsh, D. Zarifi, A. U. Zaman, and P. S. Kildal, "Corporate Distribution Networks for Slot Array Antenna Based on Groove Gap Waveguide Technology," in *2016 10th European Conference on Antennas and Propagation (EuCAP)*, (Davos), pp. 1–3, IEEE, apr 2016.
- [71] D. Zarifi, A. Farahbakhsh, A. U. Zaman, and P. S. Kildal, "A High Gain Ridge Gap Waveguide Fed Slot Antenna Array for 60 GHz Applications," in *2016 10th European Conference on Antennas and Propagation (EuCAP)*, (Davos), pp. 1–3, IEEE, apr 2016.

- [72] A. Vosoogh and P.-S. Kildal, "Corporate-Fed Planar 60 GHz Slot Array Made of Three Unconnected Metal Layers Using AMC pin surface for the Gap Waveguide," *IEEE Antennas and Wireless Propagation Letters*, pp. 1–1, 2015.
- [73] A. Vosoogh, P.-S. Kildal, and V. Vassilev, "A Multi-Layer Gap Waveguide Array Antenna Suitable for Manufactured by Die-Sink EDM," in *2016 10th European Conference on Antennas and Propagation (EuCAP)*, pp. 1–4, IEEE, apr 2016.
- [74] K. R. Williams and R. S. Muller, "Etch Rates for Micromachining Processing," *Journal of Microelectromechanical Systems*, vol. 5, no. 4, pp. 256–269, 1996.
- [75] J. D. Gelorme, R. J. Cox, and S. A. R. Gutierrez, "Photoresist composition and printed circuit boards and packages made therewith," 1989.
- [76] MicroChem Corporation, "SU-8 2100-2150 Data Sheet."
- [77] H. Lorenz, M. Despont, N. Fahrni, J. Brugger, P. Vettiger, and P. Renaud, "High-aspect-ratio, ultrathick, negative-tone near-UV photoresist and its applications for MEMS," *Sensors and Actuators A*, vol. 64, no. 1, pp. 33–39, 1998.
- [78] K. V. Nemani, K. L. Moodie, J. B. Brennick, A. Su, and B. Gimi, "In vitro and in vivo evaluation of SU-8 biocompatibility," *Materials Science and Engineering C*, vol. 33, no. 7, pp. 4453–4459, 2013.
- [79] Z. Cui and R. A. Lawes, "A new sacrificial layer process for the fabrication of micromechanical systems," *Journal of Micromechanics and Microengineering*, vol. 7, pp. 128–130, sep 1997.
- [80] R. Martinez-Duarte and M. J. Madou, "Microfluidics and Nanofluidics Handbook: fabrication, implementation, and applications," in *Microfluidics and Nanofluidics Handbook Fabrication, Implementation, and Applications* (S. K. M. Suman Chakaborthy, ed.), ch. 8, pp. 231–268, CRC Press, 1 ed., 2011.
- [81] A. del Campo and C. Greiner, "SU-8: a photoresist for high-aspect-ratio and 3D submicron lithography," *Journal of Micromechanics and Microengineering*, vol. 17, pp. R81–R95, jun 2007.
- [82] X. Shang, M. Ke, Y. Wang, and M. J. Lancaster, "WR-3 Band Waveguides and Filters Fabricated Using SU8 Photoresist Micromachining Technology," *IEEE Transactions on Terahertz Science and Technology*, vol. 2, no. 6, pp. 629–637, 2012.
- [83] S. Iijima, "Helical microtubules of graphitic carbon," *Nature*, vol. 354, no. 6348, pp. 56–58, 1991.

- [84] J. W. Mintmire, B. I. Dunlap, and C. T. White, "Are fullerene tubules metallic?," *Physical Review Letters*, vol. 68, no. 5, pp. 631–634, 1992.
- [85] N. Hamada, S. I. Sawada, and A. Oshiyama, "New one-dimensional conductors: Graphitic microtubules," *Physical Review Letters*, vol. 68, no. 10, pp. 1579–1581, 1992.
- [86] R. Saito, M. Fujita, G. Dresselhaus, and M. S. Dresselhaus, "Electronic structure of chiral graphene tubules," *Applied Physics Letters*, vol. 60, no. 18, p. 2204, 1992.
- [87] Y. Lan, Y. Wang, and Z. F. Ren, "Physics and applications of aligned carbon nanotubes," *Advances in Physics*, vol. 60, no. 4, pp. 553–678, 2011.
- [88] P.-S. Kildal, E. Lier, and J. Aas, "Artificially soft and hard surfaces in electromagnetics and their application," *1988 IEEE AP-S. International Symposium, Antennas and Propagation*, 1988.
- [89] P.-S. Kildal, "Definition of artificially soft and hard surfaces for electromagnetic waves," *Electronics Letters*, vol. 24, no. 3, pp. 168–170, 1988.
- [90] M. G. Silveirinha, C. A. Fernandes, and J. R. Costa, "Electromagnetic characterization of textured surfaces formed by metallic pins," *IEEE Transactions on Antennas and Propagation*, vol. 56, pp. 405–415, feb 2008.
- [91] E. Rajo-Iglesias and P.-S. Kildal, "Numerical studies of bandwidth of parallel-plate cut-off realised by a bed of nails, corrugations and mushroom-type electromagnetic bandgap for use in gap waveguides," *IET Microwaves, Antennas and Propagation*, vol. 5, no. 3, p. 282, 2011.
- [92] D. Sievenpiper, L. Zhang, R. F. J. Broas, N. G. Alexopolous, and E. Yablonovitch, "High-impedance electromagnetic surfaces with a forbidden frequency band," *IEEE Transactions on Microwave Theory And Techniques*, vol. 47, no. 11, pp. 2059–2074, 1999.
- [93] A. U. Zaman, V. Vassilev, P.-S. Kildal, and A. Kishk, "Increasing parallel-plate stopband in gap waveguides using inverted pyramid-shaped nails for slot array application above 60 GHz," in *5th European Conference on Antennas and Propagation (EuCAP)*, pp. 2254–2257, 2011.
- [94] E. Rajo-Iglesias, P.-S. Kildal, A. U. Zaman, and A. Kishk, "Bed of Springs for Packaging of Microstrip Circuits in the Microwave Frequency Range," *IEEE Transactions on Components, Packaging and Manufacturing Technology*, vol. 2, pp. 1623–1628, oct 2012.

- [95] E. Pucci, A. U. Zaman, E. Rajo-Iglesias, P.-S. Kildal, and A. Kishk, "Study of Q-factors of ridge and groove gap waveguide resonators," *IET Microwaves, Antennas and Propagation*, vol. 7, pp. 900–908, aug 2013.
- [96] J. Papapolymerou, J.-C. Cheng, J. East, and L. P. B. Katehi, "A micromachined high-Q X-band resonator," *IEEE Microwave And Guided Wave Letters*, vol. 7, pp. 168–170, 1997.
- [97] D. Kajfez, S. Chebolu, M. R. Abdul-Gaffoor, and A. A. Kishk, "Uncertainty analysis of the transmission-type measurement of Q-factor," *IEEE Transactions on Microwave Theory and Techniques*, vol. 47, no. 3, pp. 367–371, 1999.
- [98] J. Gao, A. Kasamatsu, F. Kojima, and K. Li, "Performance of transmission line on liquid crystal polymer (LCP) from 220 GHz to 330 GHz," in *2015 8th UK, Europe, China Millimeter Waves and THz Technology Workshop (UCMMT)*, pp. 1–4, IEEE, sep 2015.
- [99] E. Pucci and P.-S. Kildal, "Contactless Non-Leaking Waveguide Flange Realized by Bed of Nails for Millimeter Wave Applications," in *6th European Conference on Antennas and Propagation (EUCAP)*, pp. 3533–3536, 2012.
- [100] A. Algaba-Brazález, E. Pucci, S. Rahiminejad, and P.-S. Kildal, "Experimental validation of a ridge gap waveguide resonator at 100 GHz," in *IEEE International Symposium on Antennas and Propagation, AP-S 2013*, (Orlando, USA), 2013.
- [101] A. Algaba Brazalez, J. Flygare, J. Yang, V. Vassilev, M. Baquero-Escudero, and P.-S. Kildal, "Design of π -Band Transition From Microstrip to Ridge Gap Waveguide Including Monte Carlo Assembly Tolerance Analysis," *IEEE Transactions on Microwave Theory and Techniques*, vol. 64, pp. 1245–1254, apr 2016.
- [102] W. R. McGrath, C. Walker, M. Yap, and Y.-C. Tai, "Silicon micromachined waveguides for millimeter-wave and submillimeter-wave frequencies," *IEEE Microwave And Guided Wave Letters*, vol. 3, pp. 61–63, mar 1993.
- [103] I. Stil, A. L. Fontana, B. Lefranc, A. Navarrini, P. Serres, and K. F. Schuster, "Loss of WR10 waveguide across 70-116 GHz," in *22nd International Symposium on Space Terahertz Technology*, (Tokyo), pp. 151–153, apr 2012.
- [104] D. Zarifi, A. Farahbakhsh, A. U. Zaman, and P.-S. Kildal, "Design and Fabrication of a High-Gain 60-GHz Corrugated Slot Antenna Array With Ridge Gap Waveguide Distribution Layer," *IEEE Transactions on Antennas and Propagation*, vol. 64, pp. 2905–2913, jul 2016.